UNSTEADY FLOW PHYSICS OF AIRFOIL DYNAMIC STALL

BY

ROHIT GUPTA

DISSERTATION

Submitted in partial fulfillment of the requirements
for the degree of Doctor of Philosophy in Aerospace Engineering
in the Graduate College of the
University of Illinois at Urbana-Champaign, 2020

Urbana, Illinois

Doctoral Committee:

Assistant Professor Phillip J. Ansell, Chair
Professor Gregory S. Elliott
Professor J. Craig Dutton
Assistant Professor Karen Mulleners

Abstract

A series of wind tunnel experiments were conducted on an NACA 0012 airfoil undergoing a linear pitch ramp maneuver at a fixed dimensionless pitch rate of $\Omega^+ = 0.05$ and across three transitional Reynolds numbers, $Re_c = 0.2 \times 10^6$, $Re_c = 0.5 \times 10^6$, and $Re_c = 1.0 \times 10^6$. The primary objectives of these experiments were to perform a detailed analysis of the flow evolution, with particular emphasis on the underlying physical mechanisms, and to extract the dominant scales associated with the flow perturbations, for a canonical dynamic stall process. A series of unsteady surface pressure measurements, with a high sampling frequency, were acquired in order to investigate the time-dependent behavior of the flow in the immediate vicinity of the airfoil. These surface pressure measurements were used to identify the region of boundary layer transition during the initial stages of the dynamic stall process. A spatially-contracting laminar separation bubble was also identified near the airfoil leading edge from the characteristic pressure plateau in the surface pressure distribution. The dominant frequencies associated with the laminar separation bubble were extracted using a continuous wavelet transform technique. These frequencies were observed to span a wide range of chord-based Strouhal numbers between $St = 50$ and $St = 105$, at $Re_c = 0.5 \times 10^6$. The off-body flow evolution was inferred and described using a combination of surface pressure measurements and time-resolved particle image velocimetry. For $Re_c = 0.2 \times 10^6$ and $Re_c = 0.5 \times 10^6$, the dynamic stall vortex was observed to emerge from a collective interaction of the discrete vortices that were ejected from the leading edge of the airfoil. At $Re_c = 1.0 \times 10^6$, however, the near-wall vortices were observed to amalgamate into two regions, forming a distinct primary and a secondary coherent structure. After formation, these two structures were observed to interact with each other, following a co-rotating vortex merging process and resulting in the emergence of a single, coherent dynamic stall vortex. The process of emergence of the dynamic stall vortex at $Re_c = 1.0 \times 10^6$, observed from the present experiments, is therefore quite distinct from the classical understanding of the dynamic stall vortex formation, which was observed at the lower Reynolds numbers. The time-dependent spectra of the velocity field were calculated using a combination of empirical mode decomposition and Hilbert transformation. From the velocity spectra, the fluctuations in the flow were observed to attain an amplified state during the initial ejection of vorticity from the leading-edge region of

the airfoil. During this amplified phase, the most dominant velocity fluctuations were found to conform to a range of displacement-thickness based Strouhal scales between $St_{\delta^*} = 0.09$ and $St_{\delta^*} = 0.14$. Finally, a numerical implementation of the Orr-Sommerfeld equation was used to extract the spatially-unstable modes associated with the phase-averaged velocity measurements near the airfoil leading edge. The most unstable frequencies from linear stability analysis were found to be consistent with those determined directly from the velocity acquisition during the amplified shedding phase of the dynamic stall process.

Acknowledgments

This document serves as a great example of abstraction wherein my name as the sole author of the work, described herein, quite unfortunately ignores the incredible support and guidance that I have received from a multitude of people in a way that was absolutely critical for the successful completion of this work. First of, I would like to thank my advisor Prof. Ansell, who is quite simply the best advisor that I could have ever hoped for. He has been unbelievably kind, patient, and supportive, and has quite frankly spoiled me through my time as a graduate student by creating an environment of unbelievable intellectual freedom for my research. I'm extremely fortunate to have had the opportunity to work under his guidance and mentorship and I can't thank him enough for all of the things that he has done for me. I would also like to thank the other members of my committee for the inavaluable discussions, comments, and suggestions that have significantly improved the quality of this work. I'm particularly thankful to Prof. Dutton for his wonderfully inspiring lectures on Advanced Gas Dynamics and to Prof. Mulleners for allowing me to spend several months with the UNFoLD research group at EPFL in Switzerland.

I'm greatly indebted to my parents, my uncle, and the rest of my family for what feels like the entire universe (both observable and beyond) and I'm therefore going to restrict myself from typing it all out in words. I'm also very grateful for all of the friendships back home in India that I continue to lean upon for critical emotional support, quite like the concrete foundation at the base of the leaning tower of Pisa. I'm also very thankful to Prof. Mukherjea, who served as a great inspiration to me both academically and beyond through all of my interactions with him as an undergraduate student at IIEST, Shibpur. I'm very thankful to all of the past and current graduate students from what I consider as the Experimental Fluid Dynamics 'supergroup' at the University of Illinois for their mentorship and their friendship, which I continue to value and cherish. I'm specifically thankful to the members of the Aerodynamics and Unsteady Flows Research Group who have basically been my family away from home and have generously humored me through all of my distractions and puerile innuendos. In particular, I owe a great deal of gratitude to Georgi Hristov for being quite generous with his time in helping me set up the dynamic stall experiments in the wind tunnel facility at the University of Illinois.

I want to thank all of the science bloggers and youtubers who have served as a source of periodic inspiration that has helped sustain my interest in science. I'm grateful to the process of fermentation, which proved to be an invaluable resource during the preparation of this document. I'm extremely thankful to Jon Retter for his continued friendship and support despite all of my inadequecies that render me unworthy of this friendship. I'm very grateful to him. Finally, I'm also extremely grateful to all those who continue to hold steadfast to the values of humility and empathy in the modern world. They are truly an inspiration.

Table of Contents

List of Tables

List of Figures

List of Abbreviations

AC	Alternating Current
A/D	Analog to Digital
BL	Boundary Layer
CAD	Computer-Aided Design
CMOS	Complementary Metal-Oxide Semiconductor
CWT	Continuous Wavelet Transform
DSV	Dynamic Stall Vortex
EMD	Empirical Mode Decomposition
EXP	EXPerimentally determined quantity
FA-MVEMD	Fast and Adaptive, multi-dimensional, Multi-Variate EMD
IMF	Intrinsic Mode Functions
LECS	Leading-Edge Coherent Structures
LES	Large-Eddy Simulation
LSB	Laminar Separation Bubble
LST	Linear Stability Theory
Nd	Neodymium-doped crystal
PIV	Particle Image Velocimetry
SCXI	Signal Conditioning eXtensions for Instrumentation
TR-PIV	Time-Resolved PIV
YAG	Yttrium-Aluminum Garnet
YLF	Yttrium-Lithium Fluoride

List of Symbols

A	fluctuation amplitude or left matrix in the eigenvalue formulation for absolute instability
A_{inlet}	cross-sectional area of the wind tunnel inlet
A_{ts}	cross-sectional area of the test-section inlet
a_n	hyperbolic tangent fit coefficients
a_∞	freestream speed of sound
B	Right matrix in the eigenvalue formulation for absolute instability
b	span of the airfoil model
C	empty test-section cross-sectional area
$\mathbb{C}$	set of complex numbers
C_0	pre-defined constant in Sutherland's law of viscosity
C_N	Series of matrices in the eigenvalue formulation for convective instability
C_l	lift coefficient
$C_{l,cor}$	tunnel corrected C_l
$C_{l,max}$	maximum value of C_l
$C_{l,uncor}$	uncorrected C_l
C_m	quarter-chord pitching moment coefficient
$C_{m,cor}$	tunnel corrected C_m
$C_{m,min}$	minimum value of C_m
$C_{m,uncor}$	uncorrected C_m
C_p	pressure coefficient
$C_{p,cor}$	tunnel corrected C_p
$C_{p,f}$	low-pass-filtered C_p
$C_{p,min}$	minimum value of C_p
$C_{p,rms}$	root-mean-square of C_p
$C_{p,uncor}$	uncorrected C_p

c	airfoil chord length
D	velocity gradient tensor
$\mathbf{d}$	detail of $\mathbf{h}$ obtained by subtracting the mean envelope
d_n	Chebyshev expansion coefficients
d_p	PIV particle diameter
E	generalized signal energy or fluctuation energy
$\mathbb{E}$	expected value of a parameter
F	functional form of dispersion relationship
F'_{x_c}	net force on airfoil along x_c
F'_{y_c}	net force on airfoil along y_c
f	frequency
$f_\#$	lens f-number setting
f_0	wavelet center frequency
f_{acq}	acquisition frequency
f_l	focal length of lens and optics
$H(\,.\,)$	Hilbert transform of an input signal
$\mathbf{h}$	multidimensional, multivariate signal
h_{LSB}	LSB chordwise length projected in vertical plane
h_p	h projected along $\mathbf{n}$
$h_{p,m}$	mean envelope of h_p
$h_{p,max}$	maximum envelope of h_p
$h_{p,min}$	minimum envelope of h_p
h_w	width of the test section
I	normalized intensity of first image in PIV correlation
I'	normalized intensity of second image in PIV correlation
K_1	solid blockage velocity correction constant
k	non-dimensional perturbation wavenumber
k_i	imaginary part of k
k_r	real part of k
L'	airfoil lift
l_{LSB}	chordwise extent of the LSB
$M'_{c/4}$	airfoil quarter-chord pitching moment
M_∞	freestream Mach number

m	pressure transducer calibration slope
N_{exp}	number of independent experimental realizations
$\mathbf{n}$	pre-defined unit normal used to obtain h_p
P	base flow pressure field or pressure measured using unsteady transducer
p	pressure
p'	perturbation in p
$\hat{p}$	amplitude of p'
p_{inlet}	static pressure aft of the turbulence screens
p_∞	static pressure at the inlet of test section
Q	second invariant of D used for vortex identification
Q_p	set of physical quantities
Q_{ref}	reference value used for colormap scale normalization of Q
q_∞	freestream dynamic pressure
R	specific gas constant
$\mathbb{R}$	set of real numbers
R^2	least-squares error used for curve-fitting purposes
Ra	average surface roughness
Re	Reynolds number
Re_c	chord-based, freestream Reynolds number
Re_{δ_r}	Reynolds number based on δ_r
S	wavelet amplitude
St	chord-based Strouhal number
St_{LSB}	Strouhal number based on the projected length of the LSB
St_p	Stokes number of seed particle used for PIV
St_{δ^*}	δ^* and u_{max} based Strouhal number
s	sample input signal
T	temperature
T_0	pre-defined constant in Sutherland's law of viscosity
T_n	n^{th} order Chebyshev polynomial
T_∞	ambient air temperature
t	time
t^d	two-sided Student's t-distribution
t_0	a select instance in time

t_a	maximum airfoil thickness
t_{acq}	acquisition time period
t_f	characteristic time scale of flow
t_p	characteristic time scale of seed particle used for PIV
t_{pulse}	laser pulse timing
U	base flow velocity profile
U_{inlet}	velocity at the inlet of wind tunnel
U_{Q_p}	uncertainties associated with Q_p
U_∞	freestream velocity
u	velocity component along x
$\mathbf{u}$	velocity vector
u'	perturbation in u
$\hat{u}$	amplitude of u'
u_a	hyperbolic tangent velocity profile
u_e	experimentally-acquired velocity profile
u_{max}	maximum velocity in the shear layer
V	velocity magnitude
V_p	unsteady pressure transducer voltage
V_m	volume of the airfoil model
V_{max}	maximum velocity for colormap scale normalization of V
v	velocity component along y
v'	perturbation in v
$\hat{v}$	amplitude of v'
v_a	analytic signal from Hilbert transform
w	column vector of Euclidean distances used for order-statistics filter
$\mathbf{x}$	position vector
x	freestream direction
x_0	a select point along x
x_c	chordwise direction
y	transverse direction
$\hat{y}$	Chebyshev domain obtained from a mapping of y using ξ
y_0	a select point along y
y_c	chord-normal direction

y_m	m^{th} collocation point on y
$\hat{y}_m$	m^{th} collocation point on $\hat{y}$
y_{max}	y as $v' \to 0$ or y at $u = u_{max}$
z	direction normal to the $x - y$ plane
$\mathbb{Z}$	set of integers
α	angle of attack
α_{ci}	confidence interval associated with t^d
α_{cor}	tunnel corrected α
α_{min}	α corresponding to $C_{m,min}$
α_{stall}	α corresponding to $C_{l,max}$
α_{uncor}	uncorrected α
δ^*	shear layer displacement thickness
δ_r	bead-size for transition trip
ϵ_{sb}	solid blockage velocity increment factor
η	wavelet scale parameter
μ_0	pre-defined constant in Sutherland's law of viscosity
μ_∞	dynamic air viscosity
ν	non-dimensional angular frequency
ν_i	imaginary part of ν
ν_r	real part of ν
ξ	scale factor for coordinate transformation from y to $\hat{y}$
ρ	density
ρ_p	PIV particle density
ρ_∞	ambient air density
σ	wavelet support
σ_c	streamline curvature coefficient
σ_{std}	sample standard deviation
τ	time parameter in wavelet and Hilbert transform integrals
ψ	wavelet function
Ω	dimensional pitch rate
Ω^+	non-dimensional pitch rate
ω	vorticity vector
ω_{ref}	reference value used for colormap scale normalization of ω
ω_z	vorticity component along z

Chapter 1

Introduction

Dynamic stall is a complex phenomenon which occurs for aerodynamic geometries subjected to unsteady separation due to rapid changes in the relative freestream conditions. These changes in the relative freestream are commonly introduced through unsteady kinematics of a body, such as a pitching, plunging, or surging motion, or some combination thereof. Dynamic stall can also be induced due to externally-applied changes in freestream conditions, such as gusts or unsteady vortex interactions. The dynamic stall phenomenon is associated with a precipitous growth in the flowfield unsteadiness, which induces high-amplitude structural vibrations and causes an overall decline in the vehicle aerodynamic performance. While this process is most commonly associated with rotorcraft in forward flight, it can also affect fixed wing aircraft under severe gust loading or during extreme maneuvers. In the biological domain, this phenomenon is a known occurrence in organisms that utilize high-speed pitching, perching, or flapping motions of lift and thrust-generating surfaces. The dynamic stall flowfield contains complex interactions amongst several canonical fluid processes that span a wide range of spatio-temporal scales. This multi-scale nature of the phenomenon has made it substantially difficult to understand, model, and predict.

1.1 Literature Review

Several seminal investigations in the literature [1, 3–12] have led to an improved phenomenological understanding of the dynamic stall phenomenon. A typical dynamic stall process on an oscillating airfoil initiates with localized flow reversal near the airfoil trailing edge that spreads further upstream along the airfoil surface with increasing angles of attack. The separated shear layer at the airfoil leading edge, after the growth of flow reversal across the entire chord, rolls up due to an inherent instability to form a characteristic leading-edge vortex. Thus, the defining feature of the dynamic stall process, i.e., the dynamic stall vortex (DSV), emerges beyond a critical angle of attack, which defines the instance of the onset of dynamic stall. With further increase in the airfoil angle of attack, the DSV grows rapidly as it convects downstream past the airfoil quarter chord, leading to a large overshoot in the lift and the quarter-chord pitching moment coef-

ficients, as compared to the stationary airfoil. Eventually the DSV, with sufficient passage of time, convects past the vicinity of the airfoil surface leading to a significant attenuation of the aerodynamic performance coefficients, from the previously reported overshoots. The post-stall airfoil is characterized by a bluff-body type wake with a large recirculation area. A schematic of the dynamic stall process, and its effects on the normal force and pitching moment coefficients, is presented in Fig. 1.1, after Carr. [1]

Beyond the morphological description, the classical studies also contain an in-depth exploration of the parameter space, analyzing the effects of the motion parameters, Reynolds number, and the airfoil geometry on the overall flow characteristics and the airfoil performance coefficients. Carr et al. [1] used a combination of surface pressure transducers, hot-wire probes, and smoke-flow visualization to study the dynamic stall process on an oscillating NACA 0012 airfoil in pitch, for a wide range of frequencies, Reynolds numbers, and oscillation amplitudes. These experiments were conducted for a baseline Reynolds number of $Re_c = 2.5 \times 10^6$. For the range of parameters investigated in this study, the dynamic stall process was found to be less sensitive to the variation in Reynolds number in comparison with changes in the reduced frequency and oscillation amplitude. Furthermore, a light stall of the airfoil, characterized by viscous interactions with a characteristic length scale equal to the airfoil thickness, was found to have a stronger dependence on the aforementioned parameters in comparison with a deep dynamic stall, where the scale of viscous interactions is commensurate with the airfoil chord. McCroskey et al. [4] conducted dynamic stall experiments on a baseline NACA 0012 airfoil subjected to a harmonic pitch motion at $Re_c = 2.5 \times 10^6$. These authors were able to induce a transformation from a trailing-edge type stall behavior to a leading-edge type stall through careful variations in the leading-edge geometry of the airfoil model. In addition to the parametric analysis, several studies have also investigated the phenomena of dynamic stall hysteresis and aerodynamic damping, as detailed by McCroskey. [6] The hysteresis effects were found to result from the inertial lag in the flow development during rapid motion of the airfoil, producing a characteristic asymmetry in the aerodynamic force and moment polars. The presence of dynamic stall hysteresis, therefore, renders the aerodynamic coefficients as path-dependent functions of the angle of attack. For an oscillating airfoil, the aerodynamic damping parameter provides a quantitative measure of the net work done over a complete cycle of oscillation. This damping parameter was found to be negative during certain critical phases of the dynamic stall process, which indicates that the airfoil extracts energy from the freestream leading to an unconstrained and potentially catastrophic growth in the oscillation amplitude. Chandrasekhara et al. [11, 12] used a combination of Schlieren imaging and interferometric measurements to investigate the effects of compressibility on a rapidly-pitching NACA 0012 airfoil. For a sufficiently high freestream Mach number, these authors discovered a series of shock waves near the airfoil leading edge during the initial stages

of the dynamic stall process. Furthermore, in the presence of significant compressibility, the DSV was found to be confined closer to the airfoil surface in comparison with the case of an incompressible dynamic stall process.

Recent investigations have moved beyond the domain of simple morphological descriptions to explore the detailed underlying processes associated with the overarching dynamic stall phenomenon using a combination of advanced experimental techniques and high-fidelity simulations. While these studies span both the two-dimensional and three-dimensional domains, only the former has been highlighted in this chapter, in order to be consistent with the nature of the present investigation. Pruski and Bowersox [13] investigated the development of leading-edge flow structures about an oscillating NACA 0012 airfoil model at a chord-based Reynolds number of $Re_c = 1.0 \times 10^6$ using planar particle image velocimetry (PIV). These authors noticed the growth of the leading-edge vortex, after formation, due to the interaction with the surrounding vorticity prior to the detachment from the airfoil surface. As such, the authors concluded that the DSV, for an instantaneous realization of the dynamic stall process, results from the coalescence of shear-layer vortices rather than a distinct singular vortex. Mulleners and Raffel [14,15] used a combination of unsteady pressure measurements, time-resolved particle image velocimetry (TR-PIV), and coherent structure analysis to study the behavior of the off-body flow during dynamic stall, focusing primarily on the stall development and stall onset phases of the phenomenon. These investigations were performed on a sinusoidally-oscillating OA209 airfoil at $Re_c = 9.2 \times 10^5$. Based on the behavior of the separated shear layer, the stall development phase was classified into a distinct primary instability stage, which was followed by a vortex formation stage. The primary instability stage was characterized by the initial growth of instabilities in the separated shear layer. The vortex formation stage, in contrast, was used in reference to the large-scale roll up of the shear layer as a result of the non-linear interactions within the shear layer. The transition from the primary instability to the vortex formation stages was identified based on the rate of displacement of the separated shear layer, which was observed to be distinctly higher during the vortex formation stage of the dynamic stall process. Beyond stall development, a vortex-induced separation mechanism was identified by these authors, as the governing physical process that was responsible for the onset of dynamic stall. The two-stage stall development process was also observed by Deparday and Mulleners [16,17]. Additionally, these authors were able to demonstrate a strong mathematical correlation between the surface pressure field near the airfoil leading edge and the state of the shear layer during the stall development phase of the dynamic stall process.

Large-eddy simulations (LES) were employed by Visbal [18] and Visbal and Garmann [19] to analyze a series of constant-pitch rate-based dynamic stall processes on NACA 0012 and SD 7003 airfoils at $Re_c = 0.2 \times 10^6$ and $Re_c = 0.5 \times 10^6$. Besides the onset of dynamic stall, these authors investigated the detailed underlying

viscous mechanisms that appear prior to the emergence of the DSV. Several characteristic features of the unsteady boundary layer (BL) were identified in these studies, including a laminar-to-turbulent transition region, which was observed to propagate upstream along the airfoil surface with increasing angles of attack, and the emergence of a leading-edge laminar separation bubble (LSB). The LSB, in particular, was identified as a critical feature of the dynamic stall flowfield, as the breakdown of the structure was observed to initiate the rapid shedding of vorticity near the airfoil leading edge, leading to the onset of dynamic stall. The unsteady character of the LSB was also highlighted in these studies, in particular near stall onset, during which time the LSB was shown to be a source of significant acoustic radiation, which propagated across large sections of the flowfield. The fundamental characteristics of the LSB were corroborated by Wen and Gross [20], who also used LES to study the flow behavior about a Sirkosky SCC-A09 airfoil at $Re_c = 0.2 \times 10^6$, for complex motion profiles, which included non-inertial effects from the centrifugal and Coriolis forces. The criticality of the LSB to dynamic stall onset was investigated even further in the recent numerical simulations of Benton and Visbal [21,22] involving an NACA 0012 geometry subjected to a constant-pitch rate maneuver at $Re_c = 1.0 \times 10^6$. These authors demonstrated that, for the given flow conditions, the LSB breakdown was initiated by a direct interaction with the turbulent separation that starts from the airfoil trailing edge and propagates upstream with increasing angles of attack. A causal relationship was also established between the breakdown of the LSB and the onset of dynamic stall, in further confirmation of the LSB-induced flow physics, described previously by Visbal and Garmann. [19] The effects of airfoil thickness on the mechanism for stall onset were explored numerically by Sharma and Visbal, for a fixed constant-pitch rate motion profile and a chord-based Reynolds number of $Re_c = 0.2 \times 10^6$. [23, 24] These authors observed a gradual shift in the underlying mechanism with increasing airfoil thickness, from an initial leading-edge type stall, caused by LSB breakdown due to strong adverse pressure gradients, to a mixed leading- and trailing-edge type stall, which is triggered by an interaction between trailing-edge turbulent separation and the leading-edge LSB. LES-based investigations have also been employed, in the recent past, for concept-level exploratory studies of dynamic stall flow control using unsteady actuation near the airfoil leading edge. [25,26] The targeting of natural instabilities within the LSB was demonstrated through these studies to have a favorable impact on the airfoil aerodynamic performance, leading to a suppression of the turbulent BL separation on the airfoil surface, a significant mitigation of the overall vibratory loading, and an associated delay in the emergence of the DSV.

Due to the complex, multi-scale nature of dynamic stall, several studies have also employed modal decomposition techniques to identify the underlying, repeating patterns, from the overall statistical process in the flowfield. Mohan et al. [27,28] used proper orthogonal decomposition and dynamic mode decomposition

to extract the dominant components of the numerically-derived flow about a rapidly plunging SD 7003 airfoil at $Re_c = 6 \times 10^4$. These authors demonstrated that the overall dynamic stall process could be reconstructed to a high degree of accuracy using only a small subset of the modal components. Dunne et al. [29] employed dynamic mode decomposition to extract the prominent timescales associated with the flow structures of interest from the experimentally-acquired velocity field about a wind turbine blade, at $Re_c = 1 \times 10^6$. Several major timescales were identified in this study, including the overall period of the flow as imposed by the combined pitching and plunging motion cycle, a vortex formation time associated with the leading-edge coherent structure, and the time period of vortex shedding at the airfoil trailing edge. In spite of these efforts, the extraction of well-defined and physically-relevant modal components however, remains a significant challenge due to the non-stationary nature of the dynamic stall process. The complex, underlying trend of the process is not well represented by a set of predefined basis functions. Stated differently, a finite set of modes with fixed spatio-temporal scales is largely inadequate in describing the rapidly evolving flow during the dynamic stall process. Thus, some recent efforts have been directed towards the application of scale-based, adaptive modal decomposition techniques that are not limited to stationary signals to the dynamic stall flowfield. Mohan et al. [30] used a combination of Empirical Mode Decomposition (EMD) and 1D Fourier transform to provide statistical insights into the onset of dynamic stall. The time-dependent velocity signal used for this analysis was extracted at a representative point in space from the full LES-derived velocity field about a plunging SD7003 airfoil [30], which had been discussed previously. A reconstructed velocity signal, using only a finite set of modes with comparatively large spatio-temporal scales, was found to adequately capture the time evolution of the velocity during the initial phase of the dynamic stall process. However, the same signal was deemed insufficient in capturing the physically-relevant features of the velocity evolution during dynamic stall onset, which indicated that the stall onset phase was associated with a significant growth of the transient, high-frequency modes in the unsteady flowfield. Wen and Gross [31] employed ensemble EMD on the aerodynamic coefficients for the dynamic stall process about a Sirkosky SCC-A09 airfoil. These performance coefficients were obtained from simulations, which were performed as part of a previous study of the authors [20], as discussed above. In this study, the intermittent processes during dynamic stall were detected more efficiently using EMD, as compared to proper orthogonal decomposition. Ansell and Mulleners [32] used a combination of EMD and 2D Fourier transform on the experimentally-acquired velocity field about a sinusoidally pitching OA209 airfoil, to provide quantitative estimates of the dominant length scales associated with the dynamic stall flowfield. These length scales were then related to the characteristic flow structures in the off-body flowfield, including the formation of discrete vortices due to an instability in the separated shear layer, interactions

between distinct vortical structures leading to a vortex-pairing process, and the large-scale roll-up behavior resulting in the emergence of the DSV.

1.2 Research Objectives

The current study is aimed at providing a comprehensive, physics-based experimental analysis of a canonical dynamic stall process. While previous experiments have focused primarily on stall development and stall onset, the current investigation describes the entirety of the dynamic stall process, starting from an analysis of the near-wall flow features for the largely attached BL, and leading up to an examination of the vorticity development in the off-body flow, during the emergence of the DSV. A detailed study of the complete dynamic stall process, focusing primarily on the underlying mechanisms, has only been achieved thus far using numerical simulations from the recent past, as stated previously in Section 1.1. With the present experiments, which form an independent set of observations for the same process, a more robust, complementary understanding can be achieved of the various physical mechanisms that underlie this phenomenon. Moreover, a well-designed experiment provides a more realistic replication of the real-world environment by automatically accounting for all of the interactions and background randomness of the natural world, that would otherwise be difficult to model, in simulations. Beyond the identification of critical features in the flow development, a major focus of the present study involves a quantitative characterization of the dominant perturbative scales in the time-varying flowfield. Past efforts at a scale-based analysis of dynamic stall, outlined in Section 1.1, have not captured the simultaneous spatial and temporal dependence of the characteristic scales in the flow. The precise nature of this spatio-temporal dependence is critical in the design of active flow control systems, particularly with regards to actuator placement and the choice of actuation parameters, in order to effectively target the natural instabilities in the flow. For the current study, a combination of a suitable modal decomposition method and signal processing technique is used, in an attempt to extract the time-dependent spectra for the entire flowfield and consequently, to describe the evolution of the dominant scales in the flow as a function of both space and time. In keeping with the physics-based theme of the current study, an effort is also made to identify the instability mechanism which drives the initial growth of perturbations near the airfoil leading edge, during stall development. As such, a numerical implementation of linear stability analysis is used to predict the dominant instability mode during the initial BL separation phase of dynamic stall development. These numerical predictions are compared against the actual scales in the flow, in order to investigate a possible connection between the vortex scaling, observed in the current experiments, with well-established instability mechanisms from the literature. As

a final objective of this study, the analysis of mechanisms and scales in the flow are repeated across a set of transitional Reynolds numbers in order to analyze the Reynolds number dependence of the overall dynamic stall process, with particular emphasis on the off-body vorticity development and the energy spectra associated with perturbations in the velocity field.

A more precise set of statements outlining the objectives of the current investigation is listed below:

- Identify the characteristic features in the near-wall flow, such as the laminar-to-turbulent transition of the BL or a possible growth of the laminar separation bubble, during the initial phase of the dynamic stall process, i.e., prior to the ejection of vortices at the airfoil leading edge, using unsteady surface pressure measurements.

- Calculate the time-dependent spectra of the pressure fluctuations near the airfoil leading edge from an alternative set of pressure measurements with high time-resolution, in order to extract potential high-frequency modes beyond what has been possible from previous experiments in the literature. Identify the dominant modes from the pressure spectra in order to characterize the time-dependent frequency variation associated with possible unsteady features in the near-wall flow, close to the airfoil leading edge.

- Infer and analyze the time-evolution of the off-body flow through a combination of unsteady pressure measurements and TR-PIV, and in particular describe, using complementary vortex identification methods, the detailed flow evolution from the initial shedding at the airfoil leading edge to the emergence and subsequent evolution of the DSV.

- Calculate the time-dependent spectra of the velocity fluctuations for the entire flowfield using a combination of a suitable modal decomposition method and signal processing technique. Describe the evolution of the most dominant perturbation modes in the flow, during the time period between the initial ejection of vortices at the airfoil leading edge and the emergence of the DSV. Also calculate the average frequency of the most dominant velocity modes during the initial shedding event at the airfoil leading edge.

- Use a numerical implementation of linear stability analysis on the phase-averaged velocity measurements to extract the two-dimensional, convectively-unstable modal perturbations. Compare the most-unstable frequencies from linear stability analysis, during the initial ejection of leading-edge vorticity, with those estimated directly from the acquired velocity measurements during an equivalent phase of the dynamic stall process. Identify the possible underlying instability mechanism that drives the initial growth of perturbations in the separated shear layer interface at the airfoil leading edge.

- Analyze the effects of Reynolds number on the overall dynamic stall process for a fixed set of motion parameters. In particular, identify any characteristic differences in the off-body vorticity development and in the dominant velocity spectra for a set of transitional Reynolds numbers.

1.3 Figures

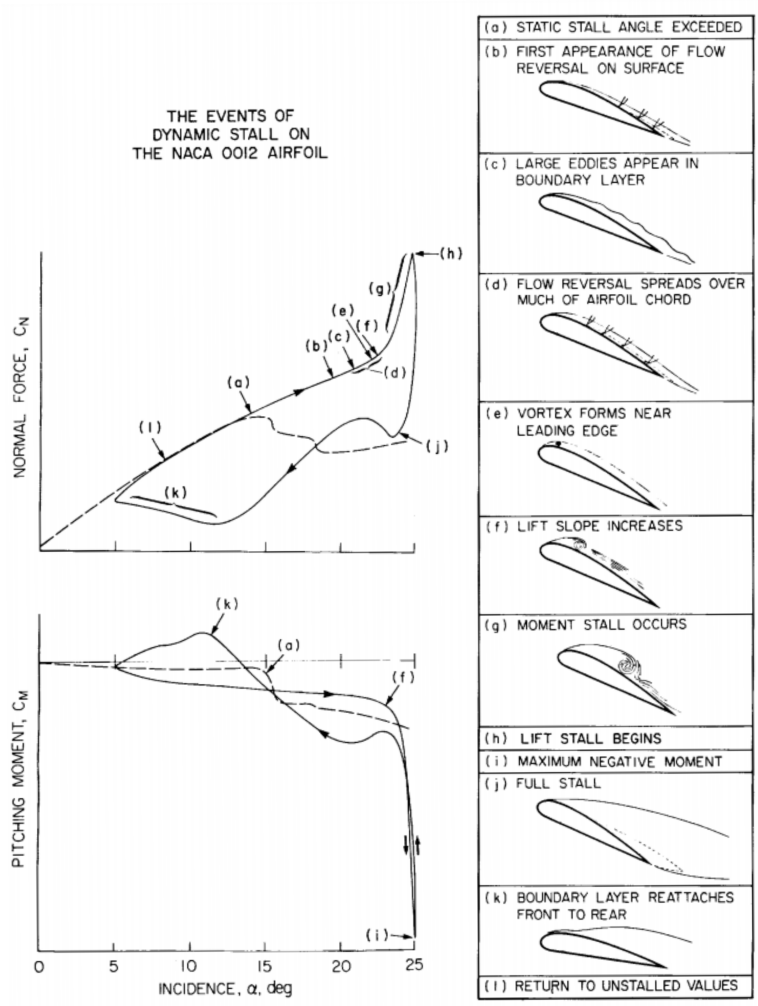

Figure 1.1: Summary of events for a canonical dynamic stall process, from Carr. [1]

Chapter 2

Methodology

All of the experiments and the data analysis techniques of the current investigation are described in this chapter, in detail. This chapter also contains the numerical formulation for linear stability analysis and a description of the experimental uncertainties.

2.1 Experimental Environment

The wind tunnel facility, airfoil installation, and the mechanical drive system for the airfoil pitch motion are described in this section.

2.1.1 Wind Tunnel

The experiments in this study were conducted exclusively in an open-return type, subsonic wind tunnel, which was part of the Aerodynamic Research Laboratory at the University of Illinois. The wind tunnel had a rectangular test section with a cross-sectional dimension of 0.9 m $\times$ 1.2 m and a length of 2.4 m in the streamwise direction. The test section was designed with a linear gradient in the cross-sectional area such that the downstream section was slightly larger in size in comparison with the section upstream in order to compensate for the growth of the BL along the tunnel walls. A 0.1 m thick honeycomb flow straightener and a total of four anti-turbulence screens were installed at the inlet of the wind tunnel. This flow conditioning configuration was effective in containing the turbulence intensity in the test section to within 0.1% at all operating speeds. A schematic of the wind tunnel is presented in Fig. 2.1.

An ABB ACS 800 Low Voltage AC Drive, with a regulated 90 kW AC motor was used to drive a five-bladed fan, which was installed aft of the tunnel diffuser. This AC motor was capable of achieving a maximum angular speed of approximately 1200 RPM, which produced an empty test section speed of approximately 75 m/s. The chord-based, freestream Reynolds number for the present experiments was calculated using the common definition:

$$Re_c = \frac{\rho_\infty U_\infty c}{\mu_\infty} \tag{2.1}$$

where U_∞ represents the freestream velocity, c denotes the airfoil chord, ρ_∞ represents the air density, and μ_∞ corresponds to the dynamic viscosity of the air.

The freestream velocity in the test-section was determined from the difference in the static pressure, Δp, between the inlet of the wind tunnel, aft of the turbulence screens, p_{inlet}, and the inlet of the test section, p_∞. Two sets of four pressure taps, installed individually on each side of the tunnel walls at the tunnel inlet and at the inlet of the test section, were used to acquire an average measurement of p_{inlet} and p_∞. The pressure measurement was accomplished using a Setra 239 pressure transducer. The ambient temperature, T_∞, was acquired using an Omega thermocouple. The freestream velocity in the test section was calculated, under assumptions of steady, inviscid, and incompressible, constant density flow, using the following equations:

$$A_{inlet}U_{inlet} = A_{ts}U_\infty \tag{2.2}$$

$$\frac{1}{2}\rho_\infty {U_\infty}^2 + p_\infty = \frac{1}{2}\rho_\infty {U_{inlet}}^2 + p_{inlet} \tag{2.3}$$

$$U_\infty = \sqrt{\frac{2\Delta p}{\rho_\infty\left(1 - \left(\frac{A_{ts}}{A_{inlet}}\right)^2\right)}} \tag{2.4}$$

where A_{inlet} corresponds to the cross-sectional area of the wind tunnel inlet, A_{ts} is the cross-sectional area at the inlet of the test section, and Δp denotes the difference between p_{inlet} and p_∞. The wind tunnel of the current investigation was associated with an A_{inlet}/A_{ts} ratio of $7.5:1$. The air density was calculated using the ideal gas law:

$$\rho_\infty = \frac{p_\infty}{RT_\infty} \tag{2.5}$$

where R denotes the specific gas constant. The dynamic viscosity was calculated from Sutherland's law with three coefficients as described by the following equation:

$$\mu_\infty = \mu_0 \frac{T_0 + C_0}{T_\infty + C_0}\left(\frac{T_\infty}{T_0}\right)^{3/2} \tag{2.6}$$

where μ_0, T_0, and C_0 are pre-defined constants. For air at moderate temperature and pressure conditions, these constants have values of $\mu_0 = 1.716 \times 10^{-5}$ kg/m-s, $T_0 = 273.11$ K, and $C_0 = 110.56$ K. Prior to the dynamic stall maneuver, the speed of the tunnel fan was controlled through an iterative computer routine to set the freestream velocity and consequently, the Reynolds number during testing to within 1% of the desired Reynolds number. For the current study, the experiments were performed at three different Reynolds numbers, $Re_c = 0.2 \times 10^6$, $Re_c = 0.5 \times 10^6$, and $Re_c = 1.0 \times 10^6$. These Reynolds numbers correspond

to a freestream Mach number of $M_\infty = 0.02$, $M_\infty = 0.05$, and $M_\infty = 0.1$, respectively, using the common definition for the Mach number:

$$M_\infty = \frac{U_\infty}{a_\infty} \tag{2.7}$$

where a_∞ denotes the speed of the sound in the freestream.

2.1.2 Airfoil Installation

An NACA 0012 airfoil model with a chord length of $c = 0.457$ m and a span of $b = 0.853$ m was used for the present study. The model was installed vertically inside the test section, with a small gap at the tunnel floor and the ceiling in order to facilitate the dynamic motion of the airfoil. The NACA 0012 geometry was selected since it has been used extensively in the past for dynamic stall investigations. [18, 19, 21, 22] The airfoil model was assembled from three different sections, as shown in Fig 2.2. The center section of the model was fabricated from aluminum through a high-fidelity electrical discharge machining process, which produced an extremely smooth surface finish with an average surface roughness less than $Ra = 1$ μm. This section had a span of 0.152 m and was designed with a hollow interior to facilitate the installation of pressure transducers, which are also indicated in Fig. 2.2. The outboard sections of the airfoil model were constructed with a foam core and a fiberglass skin in an effort to reduce the inertia of the model. These sections were fabricated carefully with a small undercut near the root, to provide a mating surface and produce a seamless fit with the center aluminum section. Primary structural support to the airfoil model was provided by the main spar, which was fabricated from a hollow steel tube of a circular cross section, with an outer diameter of 31.75 mm and a radial thickness of 6.35 mm. The center of this main spar was positioned at the quarter-chord point of the airfoil. Additional structural support was provided using a series of fasteners and round tubes that were configured to extend across the entire span of the airfoil model. A precise circular cutout was incorporated in the floor and in the ceiling of the test section for the passage of the main spar. An adjustable flap, with a low-friction surface, was used to seal the small annular gap between the spar and the corresponding cutout in the tunnel surface. The main spar was supported using a pair of bearing blocks that were installed on the outer frame of the wind tunnel. A flexible shaft coupling was used to connect the main spar with a high-torque direct drive brushless servo motor, model C(H)092 manufactured by Kollmorgen Corporation, which was installed underneath the test section. A three-dimensional rendering of the airfoil installation is provided in Fig. 2.3. Actual photographs of the dynamic stall setup, showing all of the major components, are presented in Fig. 2.4.

Using the brushless servo motor, the airfoil model was subjected to a linear pitch-ramp maneuver about the quarter-chord point at a prescribed dimensionless pitch rate, Ω^+, which is defined using the following

equation:

$$\Omega^+ = \frac{\Omega c}{U_\infty} \tag{2.8}$$

where Ω represents the dimensional pitch rate. A linear pitch ramp maneuver was chosen in order to isolate the dynamic stall process from boundary-layer hysteresis and the unsteady wake effects of periodic maneuvers. For the current investigation, a pitch rate of $\Omega^+ = 0.05$ was used, since it has been studied in the past using high-fidelity simulations. [18, 19, 21–24] The experiments were designed to capture the dynamic stall process across a range of angles of attack between $\alpha = -5°$ and $\alpha = 30°$. This range of angles of attack was selected since it spans the entirety of the dynamic stall process starting from an initial state, which is characterized by a laminar BL that is attached over the entirety of the airfoil upper surface to a final state that is characterized by post-stall bluff body shedding. The servo motor was, however, configured to rotate between $\alpha = -6°$ and $\alpha = 31°$ in order to reduce the effects of acceleration on the intended linear ramp motion profile.

In order to achieve the desired pitch-ramp maneuver, the motion parameters of the servo motor were controlled using an AKD servo drive, which was also manufactured by the Kollmorgen Corporation. Prior to performing the linear pitch-ramp maneuver, the AKD drive system was optimized for the desired motion profile using in-built performance-tuning software. As part of the performance-tuning algorithm, the airfoil installation was subjected to an initial excitation by the servo motor in order to determine the frequency response of the loaded system. This system response was acquired through a series of feedback sensors that came pre-integrated with the motor. Using this frequency response, the control parameters for the feedback controller were adjusted automatically to minimize the difference between the commanded and the actual motion profiles. Additionally, the AKD servo drive was also configured with a series of notch filters, which were designed to attenuate the resonant modes of the loaded system. The angular position of the airfoil was also monitored in real time using a high-resolution Dynapar HS35R optical encoder, which was attached directly to the airfoil rotary shaft. A comparison between the commanded and the acquired motion profiles for an example pitch-ramp maneuver under experimental conditions at $Re_c = 0.5 \times 10^6$ is presented in Fig. 2.5.

In addition to the baseline airfoil installation, several experiments were performed to acquire the time-dependent surface pressure on the airfoil model configured with a BL trip. The BL trip was constructed from a sparse distribution of spherical beads that were deposited manually over an adhesive substrate. Due to the manual construction of the BL trip, the sparsity of the bead distribution is only intended to provide a qualitative measure of the roughness density, which was kept low in order to ensure that a three-dimensional perturbation was imposed on the overarching boundary layer. The size of the beads was determined based

on the recommendations of Braslow et al. [33] for a grit-type transition trip. From this reference, a critical minimum size, δ_r, of the roughness elements was deemed necessary, such that $Re_{\delta_r} > 600$, in order to promote transition of the BL at the desired location. However, increasing the size of the roughness elements beyond $2\delta_r$ was found to have a substantial effect on the overall drag of the aerodynamic geometry. Following these recommendations, the spherical beads used in the BL trip of the current experiments were sized with an approximate diameter of $300 - 350$ μm, which produced a roughness-based Reynolds number that was marginally greater than $Re_{\delta_r} = 600$. The BL trip was installed between $x_c/c = 0.005$ and $x_c/c = 0.02$ on the upper surface of the airfoil model.

Finally, a series of experiments was also conducted with a pair of rectangular splitter plates that were installed on the airfoil model to reduce the three-dimensional effects of the flow at the model tips. These plates were fabricated with a dimension of 0.686 m by 0.457 m, following the recommendations of Diebold et al., [34] and were installed at a distance of approximately 50 mm from the floor and ceiling of the test section. The acquired experimental data in the presence of the splitter plates were however, found to be similar to the measurements acquired in the absence of these surfaces. For simplicity, all of the results presented in Chapter 3 correspond to the airfoil installation without the splitter plates.

2.2 Pressure Acquisition and Analysis

The unsteady pressure measurements were acquired using a series of 27 ultra-miniature, high frequency response pressure transducers installed across the center span of the airfoil model. In order to capture the large pressure gradients at the airfoil leading edge, the transducers were distributed more densely near the leading-edge region of the airfoil, as seen in Fig. 2.6 a).

The pressure transducers of the current study were manufactured by Kulite Semiconductor Products, Inc. under model designation XCS-062. The circular face of the transducer, exposed to the flow, had a diameter of approximately 1.7 mm and contained a screen element with 8 regularly-distributed holes as shown in Fig. 2.6 b). A pieszoresistive sensor, installed immediately behind the screen, formed the critical component of a four-arm Wheatstone bridge which was designed to produce a time-dependent output voltage that varied linearly with the applied pressure. The differential pressure range of the transducers was specified at ± 35 kPa. A temperature compensation module was also integrated in the construction to ensure a wide working temperature range between $T = 25°$C and $T = 80°$C. The unsteady voltages from the transducers were acquired through a National Instruments Signal Conditioning eXtensions for Instrumentation (SCXI) measurement system and a National Instruments PCI-MIO-16XE-10 A/D board. The SCXI system consisted

of sets of four signal conditioning modules: Simultaneous-Sampling Differential Amplifier module (SCXI-1140), 8th order Lowpass Bessel Filter module (SCXI-1142), and two Isolation Amplifiers with Excitation modules (SCXI-1121). A total of four sets of the signal conditioning modules were used to simultaneously acquire measurements from all 27 pressure transducers installed on the airfoil surface. The simultaneous sampling of the signals from each pressure transducer was achieved using the SCXI-1140 module. Since the A/D system was only capable of sampling a single channel at any given instant in time, the SCXI-1140 module was configured with a series of capacitors to store the acquired voltages from all 27 pressure transducers until the completion of the analog-to-digital signal conversion process. In order to prevent signal aliasing, the SCXI-1142 module was configured to the correct Nyquist cutoff frequency using the filter frequency response data provided by the manufacturer. The SCXI-1121 modules were used to supply a 10 V excitation to the pressure transducers and to provide electrical isolation of the acquired transducer signals. Finally, a SCXI-1321 terminal block was used for the electrical connection of the pressure transducers with the SCXI signal conditioning modules. All of the SCXI modules were compactly integrated into a SCXI-1001 chassis. A schematic of the SCXI setup is presented in Fig. 2.7.

Prior to the acquisition of the surface pressure, the transducers were calibrated using a five-point calibration process. The calibration slope, m, for each transducer was obtained by comparing the acquired voltages for five reference pressure values using the following equation:

$$\Delta P = m\Delta V_p \tag{2.9}$$

where ΔV_p represents the change in voltage associated with the change in pressure ΔP. It should be mentioned that a small gain was applied to the acquired transducer voltages in order to enhance the signal-to-noise ratio and improve the digitization of the analog signal. The unsteady pressure measurements in the present investigation were acquired at two different sampling rates, $f_{acq} = 3$ kHz and $f_{acq} = 33$ kHz. The corresponding Nyquist cutoff frequencies were set at $f = 1.5$ kHz and $f = 16.5$ kHz. It should be noted that the sampling rates of the current study are significantly lower than the manufacturer-specified transducer natural frequency of $f = 150$ kHz. For the low-sampling frequency, the surface pressures were acquired simultaneously from each transducer in order to study the time-dependent surface pressure evolution and to calculate the unsteady airfoil performance, following a mathematical process described in Section 2.2.1. In contrast with the low-sampling rate, the pressure acquisition at $f_{acq} = 33$ kHz could only be acquired individually due to hardware sampling limitations of the A/D system.

All of the pressure results in this study are presented in the airfoil-fixed frame of reference. In this

reference frame, the origin is affixed to the leading edge of the airfoil with the x-axis, x_c, oriented along the chordwise direction, and the y-axis, y_c, oriented along the chord-normal direction.

2.2.1 Performance Calculation

The pressure coefficient C_p was calculated from the acquired pressure, p, and the freestream pressure, p_∞, using the following equation:

$$C_p = \frac{p - p_\infty}{q_\infty} \tag{2.10}$$

where q_∞ represents the freestream dynamic pressure, which is defined by:

$$q_\infty = \frac{1}{2}\rho_\infty {U_\infty}^2 \tag{2.11}$$

The airfoil lift and pitching moment coefficients were calculated from the known pressure distribution across the surface of the airfoil. This calculation was accomplished by approximating the airfoil contour as a series of discrete panels. Each of these panels was generated by a linear interpolation between two adjacent pressure transducers, producing a series of $(n-1)$ panels for every n transducers. The pressure across the length of a panel was approximated as the average of the pressure at the ends of the panel. The surface traction vector resulting from the pressure on a given panel, i, was further split into a chord-normal component, $\Delta F'_{y_{c,i}}$ and a chordwise component, $\Delta F'_{x_{c,i}}$ using:

$$\Delta F'_{y_c,i} = \frac{p_i + p_{i+1}}{2}(x_{c,i+1} - x_{c,i}) \tag{2.12}$$

$$\Delta F'_{x_c,i} = -\frac{p_i + p_{i+1}}{2}(y_{c,i+1} - y_{c,i}) \tag{2.13}$$

The pitching moment about the airfoil quarter chord, $M'_{c/4,i}$, due to the forces, $\Delta F'_{y_c,i}$ and $\Delta F'_{x_c,i}$ was determined, using the following equation:

$$\Delta M'_{c/4,i} = \Delta F'_{y_c,i}\left(x_{c,c/4} - \frac{x_{c,i} + x_{c,i+1}}{2}\right) + \Delta F'_{x_c,i}\left(\frac{y_{c,i} + y_{c,i+1}}{2}\right) \tag{2.14}$$

The total chord-normal and chordwise forces, F'_{y_c} and F'_{x_c}, and the quarter-chord pitching moment, $M'_{c/4}$, were calculated by taking the summation of $\Delta F'_{y_c,i}$, $\Delta F'_{x_c,i}$, and $\Delta M'_{c/4,i}$ over all the panels on the surface of the discretized airfoil:

$$F'_{y_c} = \sum_i \Delta F'_{y_c,i} \tag{2.15}$$

$$F'_{x_c} = \sum_i \Delta F'_{x_c,i} \tag{2.16}$$

$$M'_{c/4} = \sum_i \Delta M'_{c/4,i} \tag{2.17}$$

The airfoil lift, L', was calculated by rotating the forces in the airfoil-fixed frame of reference, F'_{y_c} and F'_{x_c}, by an amount equal to the airfoil angle of attack:

$$L' = F'_{y_c}\cos(\alpha) - F'_{x_c}\sin(\alpha) \tag{2.18}$$

Finally, the airfoil lift and quarter-chord pitching moment coefficients, C_l and C_m, were determined from their commonly used definition:

$$C_l = \frac{L'}{q_\infty c} \tag{2.19}$$

$$C_m = \frac{M'_{c/4}}{q_\infty c^2} \tag{2.20}$$

2.2.2 Wavelet Analysis

The energy spectra of the pressure fluctuations were calculated using a continuous wavelet transform (CWT). In this method, the time-dependent input signal, $s(t)$, is compared against a wavelet signal or function, $\psi(t)$, using an inner product that is described below. The wavelet functions are a general class of complex-valued functions that are defined with compact support in the time domain, i.e., the functions are identically equal to zero outside a finite time interval. The time-localization of the wavelet function makes CWT a suitable choice for the analysis of non-stationary signals, such as the time-dependent surface pressure of the current investigation. In the Fourier domain, a wavelet function spans a range of frequencies that are distributed around a well-defined peak. The center frequency of the wavelet can in turn be controlled by scaling the period of the wavelet function, using a scale parameter, η. The wavelet functions can also be displaced along the time domain by changing the time-displacement parameter, τ. For a given value of η and τ, the inner product can be calculated using: [35]

$$S(\eta,\tau) = \frac{1}{\sqrt{\eta}} \int_{-\infty}^{+\infty} s(t)\bar{\psi}\left(\frac{t-\tau}{\eta}\right) dt \tag{2.21}$$

The amplitude, $S(\eta,\tau)$, provides a measure of the similarity between $s(t)$ and $\psi(t)$ as a function of the parameters η and τ. The integral from Eq. 2.21 was performed for a range of values of η and τ to obtain the full time-dependent spectra of the surface pressure during the dynamic stall process. It should be mentioned here that the wavelet analysis was performed with the time-dependent pressure measurements

that were acquired at a high sampling rate of $f_{acq} = 33$ kHz on the airfoil upper surface. The results of this analysis are presented in Chapter 3 in terms of the generalized energy, $E(\eta, \tau)$, which was calculated from the amplitude, $S(\eta, \tau)$ using the following equation:

$$E(\eta, \tau) = \log_{10} |S(\eta, \tau)|^2 \tag{2.22}$$

The Morlet wavelet, shown in Fig. 2.8, was used as the wavelet function in the current study. As discussed by Torrence and Compo, [35] this wavelet is constructed using a complex sinusoid which is compactly supported through a Gaussian envelope. The Morlet wavelet can be expressed mathematically as:

$$\psi(t) = e^{-t^2/2\sigma^2} e^{i2\pi f_0 t} \tag{2.23}$$

where f_0 corresponds to the center frequency of the unscaled wavelet and σ is a measure of the wavelet support. The Morlet wavelet was selected for this study since it has been shown to be extremely effective in the identification of oscillatory behaviors in a signal. Furthermore, due to the approximate equivalence between the Morlet and the Fourier scales, the energy spectra were conveniently transformed from the scale-based domain to the corresponding Fourier domain.

The frequencies from the wavelet analysis are presented primarily in terms of the chord-based Strouhal number, which uses the airfoil chord length and the freestream velocity as the charactersitic scales of the flow, as defined by the following equation:

$$St = \frac{fc}{U_\infty} \tag{2.24}$$

In addition to the chord length of Eq. 2.24, a variable length scale calculated by taking a projection of the chordwise extent of the LSB in the vertical plane was also used as a characteristic length scale in the non-dimensionalization of the spectral frequencies. This variable-length Strouhal scaling was calculated using the following equation:

$$St_{LSB} = \frac{fh_{LSB}}{U_\infty} \tag{2.25}$$

where h_{LSB}, as described above, was calculated from the chordwise length of the LSB, l_{LSB}, using the following equation:

$$h_{LSB} = l_{LSB} \sin(\alpha) \tag{2.26}$$

2.2.3 Tunnel Corrections

A wind tunnel testing environment is designed to simulate the flow around an airfoil model in a spatially unbounded freestream. Due to the infeasibility of such a design, however, the true wind tunnel testing environment is constrained with finite wall boundaries, which introduces local wall effects that are absent in a hypothetically unbounded freestream. All the pressure-based results presented in Chapter 3 were corrected for the solid blockage and streamline curvature effects through standard correction procedures for two-dimensional, low-Reynolds number wind tunnel testing, as described by Barlow et al. [36]

The solid blockage effect describes the effective reduction in the test section area due to the presence of the model, which produces a local acceleration of the fluid that depends on the model thickness and the airfoil angle of attack. The effects of the local acceleration were corrected using a solid-blockage velocity increment coefficient, ϵ_{sb}, defined using the following equation:

$$\epsilon_{sb} = \frac{K_1 V_m}{C^{3/2}} \tag{2.27}$$

where K_1 is a constant that depends on the model configuration. For the current study, a value of $K_1 = 0.52$ was used, based on the recommendations of Barlow et al. [36] for airfoil models that span the height of the test section. The parameter C in Eq. 2.27 represents the empty test-section area while V_m corresponds to the volume of the model, which was estimated using the following equation,

$$V_m = \frac{3}{4} t_a c b \tag{2.28}$$

where t_a represents the maximum airfoil thickness.

The streamline curvature effects, in the presence of finite boundaries, lead to an increase in the apparent camber of the airfoil, which in turn, causes an artifical increase in the airfoil lift and the magnitude of the pitching moment, in comparison with an unbounded environment. Following the detailed empirical analysis in Barlow et al., [36] the streamline curvature effects were compensated for using the streamline curvature coefficient:

$$\sigma_c = \frac{\pi^2}{48} \left(\frac{c}{h_w} \right)^2 \tag{2.29}$$

where h_w corresponds to the width of the test section.

With the solid blockage and streamline curvature coefficients, the airfoil angle of attack, surface pressure, and the lift and quarter-chord pitching moment coefficients were corrected for tunnel wall effects, using the

following equations:

$$\alpha_{cor} = \alpha_{uncor} + \frac{57.3\sigma_c}{2\pi}(C_{l,uncor} + 4C_{m,uncor}) \tag{2.30}$$

$$C_{p,cor} = \frac{C_{p,uncor}}{(1+\epsilon_{sb})^2} \tag{2.31}$$

$$C_{l,cor} = C_{l,uncor}(1 - \sigma_c - 2\epsilon_{sb}) \tag{2.32}$$

$$C_{m,cor} = C_{m,uncor}(1 - 2\epsilon_{sb}) + \frac{1}{4}\sigma_c C_{l,uncor} \tag{2.33}$$

where the subscripts *uncor* and *cor* refer to the uncorrected and the corrected parameters.

It should be noted that previous experiments in the literature on vortex shedding in the vicinity of a rigid wall have indicated that the critical shedding parameters remain unaffected for models that are installed beyond two characteristic length scales away from the wall. [37, 38] At the maximum angle of attack of $\alpha = 31°$, the leading and trailing edges of the airfoil, in the present experiments, are positioned at a distance of 0.55 m and 0.43 m away from the walls of the test-section. Thus, the model-to-wall distance at $\alpha = 31°$ is approximately 2.3 times the characteristic length scale based on the projected height of the airfoil in the vertical plane. Thus, although the tunnel walls affect the pressure and performance coefficients of the airfoil, they are not expected to influence the dominant modes of perturbations in the flow, and consequently, the energy spectra associated with the pressure and velocity fields.

2.3 Flowfield Acquisition and Analysis

The time-dependent flow evolution across a streamwise plane near the center span of the airfoil was acquired using TR-PIV. A 60 W Quantronix Darwin Duo Nd: YLF laser was used, in conjunction with a series of beamforming optics, to produce a collimated laser sheet with an approximate thickness of 1 mm. A YLF gain medium was used in this study, since the electron population in the excited state is associated with a significantly lower rate of decay, in comparison with the commonly used YAG crystals. The long upper-state lifetime enables the high rate of emission of the laser beam, which was required in order to capture the rapidly-evolving flow during the dynamic stall process. The beamforming optics used in the current setup consisted of two cylindrical diverging lenses, with $f_l = -400$ mm and $f_l = -75$ mm and a spherical converging lens, which was associated with a focal length of 300 mm. A schematic of the laser sheet formation process is shown in Fig. 2.9. The Nd:YLF laser was operated in external double trigger mode to provide a pair of laser pulses at a repetition rate of 1 kHz. A mineral oil-based haze generator was used to seed the flow with smoke particles that had a mean diameter of $d_p = 1 - 2$ μm. Using this particle

diameter, the Stokes number was calculated from the following equations:

$$St_p = \frac{t_p}{t_f} \tag{2.34}$$

$$t_p = \frac{\rho_p {d_p}^2}{18\mu} \tag{2.35}$$

where t_p and t_f denote the characteristic time scales of the seed particles and the flow, and ρ_p corresponds to the density of the particles. For the current experiments, the Stokes number was estimated at $St_p \lessapprox 0.01$, which indicates that the time scale of the seed particles is significantly lower than the characteristic time scale of the flow. Consequently, the seed particles were expected to advect almost perfectly with the flow, which suggests a negligible effect of particle lag in the acquired TR-PIV data. The images of the seed particles were acquired at 2000 frames per second using a Photron Mini AX200 CMOS high-speed camera at the maximum possible resolution of 1024×1024 pixels. The size of each pixel in this camera's sensor is equal to 20 μm, which combined with the high quantum efficiency, produced an overall light sensitivity that was deemed sufficient for the current experiments. The high-speed camera was equipped with a photographic lens set at a focal length, $f_l = 28$ mm and at an f-number setting of $f_\# = 2.8$. The camera and the lens system were installed on top of the wind tunnel in order to capture the seed particles that were illuminated by a horizontal laser sheet, which was projected from the test section sidewall. A clear acrylic surface was used to provide the required optical access to the laser and camera systems. In order to reduce the intensity of reflections off the surface of the model, the airfoil was wrapped in a thin, light adhesive black paper. The laser and camera system were configured in frame-straddling mode, with a desired acquisition frequency of $f_{acq} = 1$ kHz ($t_{acq} = 0.001$ s), as shown in Fig. 2.10.

The acquired TR-PIV images were processed in LaVision DaVis version 8.4.0 using a normalized multi-pass cross correlation procedure with a square interrogation window. The two-dimensional cross-correlation routine in DaVis uses a numerical implementation of the following equation:

$$(I * I')(\Delta x, \Delta y) = \int I(x, y) I'(x + \Delta x, y + \Delta y) dx dy \tag{2.36}$$

where I and I' denote the normalized intensities of the images at time t and $t+\Delta t$. The displacement vector is defined as the combination of Δx and Δy that is associated with the global peak in $I * I'$. The integral of Eq. 2.36 is evaluated within a pre-defined kernel, known as the interrogation window. This window slides over the entire image to generate the complete vector field. In the current experiments, the interrogation window for the first three passes was set at 128×128 pixels with 50% overlap, which was decreased sequentially to

16×16 pixels with 75% overlap, for the final three correlation passes. The time interval between the laser pulses, Δt_{pulse}, was optimized to achieve the minimum possible uncertainty for the selected interrogation windows. An algorithm-based dynamic mask was developed to eliminate the narrow reflection-containing region, with an approximate width of $1-2$ mm, in the immediate vicinity of the airfoil surface. A correlation peak filter was used to eliminate vectors for which the ratio of the primary-to-secondary correlation peak was less than a value of 1.5. A median filter was also employed to remove vectors which differed by more than two standard deviations from the neighboring vectors in a 16×16 region. All of the TR-PIV results are presented in the PIV frame of reference. In this reference frame, the origin was affixed to the quarter-chord point of the airfoil, with the x- and y-axis aligned with the freestream and transverse directions, respectively. The final velocity fields, obtained after processing, were associated with a spatial resolution of approximately 1.5×10^{-3} m in both the x and y directions.

The vorticity field, $\omega(\mathbf{x}, t)$, which provides a measure of the localized rotation rate in the flow, was calculated from the TR-PIV velocity, using the curl vector operation:

$$\omega = \nabla \times \mathbf{u} \tag{2.37}$$

For a two-dimensional flow in the x-y plane, Eq. 2.37 reduces to:

$$\omega_z = \left(\frac{\partial v}{\partial x} - \frac{\partial u}{\partial y} \right) \tag{2.38}$$

where the z-component of vorticity, ω_z, is also mathematically equal to twice the angular velocity of an infinitesimal fluid element along the z-axis.

The flow characteristics during the dynamic stall process were also investigated using the Q-criterion, based on the work of Hunt et al. [39] The parameter Q, in this method, corresponds to the second invariant of the velocity gradient tensor, D_{ij}, where $D_{ij} = \frac{\partial u_i}{\partial x_j}$ and $i, j = 1, 2, 3$ for a general three-dimensional flow. The second invariant of D is defined as:

$$Q = \frac{1}{2}(tr(D)^2 - tr(D^2)) \tag{2.39}$$

An alternative version of Eq. 2.39 was used in the current study, which was obtained by simplifying Eq. 2.39 for an incompressible, two dimensional flowfield. This simplified version of the Q parameter was calculated using:

$$Q = \frac{\partial u}{\partial x}\frac{\partial v}{\partial y} - \frac{\partial u}{\partial y}\frac{\partial v}{\partial x} \tag{2.40}$$

From a physical standpoint, the Q parameter shows the relative strength of the rate of rotation and the strain rate tensors. Thus, a positive value of Q at a given region in the flowfield defines a flow state where the rate of rotation dominates over the irrotational straining, whilst a $Q < 0$ region describes a flow state for which the strain rate dominates the associated vorticity.

2.3.1 Spectral Methods

The spectra of the dominant fluctuation modes in the velocity field, during the dynamic stall process, were extracted using a three-step procedure:

As the **first** step, the fluctuations in the velocity field were extracted from the background time-dependent trend, using EMD. EMD was selected as the decomposition method due to the data-driven, adaptive nature of the algorithm, which makes it suitable for application on a non-stationary signal, such as the velocity field associated with the current dynamic stall process. Using EMD, the instantaneous velocity, $u(x, y, t)$ and $v(x, y, t)$, were decomposed into a set of Intrinsic Mode Fuctions (IMFs), $u_k(x, y, t)$ and $v_k(x, y, t)$, which contain oscillations about a zero mean, and a Residue, $u_r(x, y, t)$, $v_r(x, y, t)$, which represents the time-dependent trend, as described by the following equations:

$$u(x, y, t) = \sum_k u_k(x, y, t) + u_r(x, y, t) \tag{2.41}$$

$$v(x, y, t) = \sum_k v_k(x, y, t) + v_r(x, y, t) \tag{2.42}$$

The effectiveness of the EMD algorithm for modal analysis of nonlinear, non-stationary signals has been demonstrated extensively in the literature. [30–32, 40, 41] For the current study, a multidimensional, multivariate version of the EMD algorithm was employed in order to ensure that the modes of the velocity field retained coherence on both velocity components, u and v, and across the space-time dimensions, x, y, and t. This advanced version of EMD, known as the Fast and Adaptive, Multidimensional, Multivariate EMD (FA-MVEMD) is described in detail in the literature. [42] A summarized version of the algorithm is presented below:

1. For the given inputs, $u(x, y, t)$ and $v(x, y, t)$, assign a new multidimensional, multivariate signal $\boldsymbol{h}(x, y, t)$. The signal $\boldsymbol{h}(x, y, t)$ represents a space-time dependent, two component generalized vector such that $\boldsymbol{h} = (h_1, h_2) = (u, v)$, where h_1 and h_2 are the two orthogonal components of $\boldsymbol{h}$.

2. Project the multivariate signal, $\boldsymbol{h}(x, y, t)$, onto a unit normal, $\boldsymbol{n} = \left(\frac{1}{\sqrt{2}}, \frac{1}{\sqrt{2}}\right)$, to obtain the projected signal $h_p(x, y, t)$.

3. Use a sliding kernel to extract and store the local maxima and minima of the projected signal, h_p, into two separate matrices, $h_{p,max}$ and $h_{p,min}$.

4. Calculate and store the Euclidean distances between adjacent entries of $h_{p,max}$ and $h_{p,min}$ into a column vector w. Use the median of the vector w as the window size for the order statistics filter.

5. The order statistics filter is a form of min-max filter, which when applied to an input signal, such as h_1, produces an output with the maximum envelope of h_1, $h_{1,max}$. An element of $h_{1,max}$ corresponding to a given space-time position, (x_o, y_o, t_o), is equal to the maximum of all the elements in h_1 that were initially encompassed by the filter centered at (x_o, y_o, t_o). Use a similar implementation of the order statistics fiter to obtain the minimum envelope of h_1, denoted as $h_{1,min}$, and consequently the mean envelope $h_{1,m}$. Repeat the entire process to obtain the mean envelope, $h_{2,m}$, for the signal h_2.

6. Extract the detail for each component h_i $(i = 1, 2)$ using the following equation $d_i = h_i - h_{i,m}$. Repeat steps 5 and 6, with $h_i = d_i$, until each detail acquires a purely oscillatory state within a certain tolerance level, as described by the following expression:

$$\frac{\sum h_{i,m}^2}{\sum h_i^2} < 0.01 \tag{2.43}$$

   The converged d_i thus obtained corresponds to the first IMF of the velocity field, $u_1(x, y, t)$ and $v_1(x, y, t)$.

7. Repeat steps 1–6, with new $\boldsymbol{h}$ equal to the difference of the previous $\boldsymbol{h}$ from step 1 and the detail, $\boldsymbol{d}$, from step 6, until all the oscillatory content from the velocity field is removed.

An example of the EMD-based decomposition of the instantaneous flowfield at $\alpha = 21.24°$ for $Re_c = 0.5 \times 10^6$ is presented in Fig. 2.11, as iso-contours of the velocity magnitude. The velocity field of Fig. 2.11 has also been normalized with respect to the maximum flow velocity, V_{max}, at the corresponding angle of attack. As a reminder, the rank of each IMF from Fig. 2.11 corresponds to the number of iterations of the complete FA-MVEMD algorithm, which was outlined in steps 1–6, previously. A total of four IMFs were extracted from the velocity field, which were associated with velocity fluctuations with progressively larger spatial, and by extension, temporal scales, as shown in Fig. 2.11 b)–e). IMF 1, therefore, exhibits the smallest scales of fluctuations in the separated shear layer that could be resolved with the present TR-PIV acquisition. In contrast, IMF 4 contains streamwise-oriented streaks that are associated with the largest length and time scales in the flow. Thus, a given iteration of the FA-MVEMD algorithm extracts flow structures that are associated with the highest available wavenumbers, k, and angular frequencies, ν. The

state of the background flow evolution at $\alpha = 21.24^\circ$ can be gauged from the Residue, which is presented in Fig. 2.11 f).

In the **second** step of the spectral analysis, the quantitative estimates of the time-dependent frequencies, f, and the perturbation amplitudes, A, were obtained by employing the Hilbert transform. Since the Hilbert transformation works best for input signals that are localized in the frequency domain, this method was not applied directly to the acquired TR-PIV velocity measurements due to the wide range of spatio-temporal scales that are associated with the full perturbations in the undecomposed flowfield. Instead, the Hilbert transform was applied individually to the y-component of velocity, v_k, at each point in space within a given IMF, using the following equation:

$$H(v_k)(t) = \frac{1}{\pi} \int_{-\infty}^{+\infty} \frac{v_k(\tau)}{t - \tau} d\tau \tag{2.44}$$

where $H(v_k)(t)$ denotes the Hilbert transform of $v_k(t)$. The convolution of the input signal $v_k(t)$ and the function $1/(\pi t)$, as defined by Eq. 2.44, introduces a phase shift of $-\pi/2$ to every Fourier component of $v_k(t)$. Thus, from the nature of the convolution integral in Eq. 2.44, the functions $v_k(t)$ and $H(v_k)(t)$ form a harmonic conjugate pair, which satisfy the Cauchy-Riemann equations. These functions are therefore combined as real and imaginary parts to construct a new complex analytic signal, as follows:

$$v_a(t) = v_k(t) + iH(v_k)(t) \tag{2.45}$$

The absolute value of the analytic signal, $|v_a(t)|$, was used to obtain a trivial measure of the time-dependent amplitude of $v_k(t)$, whilst the time-derivative of the phase angle was employed to extract the instantaneous frequency, as defined by the following equation:

$$f(t) = \frac{1}{2\pi} \frac{\mathrm{d}}{\mathrm{d}t} \tan^{-1} \left(\frac{H(v_k)(t)}{v_k(t)} \right) \tag{2.46}$$

For the purposes of presentation, the amplitude, $|v_a(t)|$, was converted into a time-dependent generalized energy using the same logarithmic definition that had been used previouly for the pressure spectra, as described by Eq. 2.22. After calculating the time-dependent energy and frequency for the velocity perturbation at a single point in space, Eq. 2.44–Eq. 2.46 were applied to the rest of the flow, within the same IMF, to obtain the spatio-temporal energy and frequency distribution for the given IMF velocity field. A set of energy and frequency iso-contours corresponding to the first three IMFs from Fig. 2.11 are presented in Fig. 2.12. The frequencies in Fig. 2.12 b) are presented in terms of the chord-based Strouhal number, which was defined previously using Eq. 2.24. A variable transparency colormap is also employed in the frequency contours of

Fig. 2.12 b), in which the level of opacity has been scaled proportional to the perturbation energy. Thus, the regions of amplified perturbations in the flow are colored more opaquely than the attenuated counterparts.

In the **final** step, the dominant mode of oscillation at each point in the flow was extracted by selecting the frequency that was associated with the highest perturbation energy from the entire set of IMFs, at a given angle of attack. This final step was repeated for all of the angles of attack of interest to produce a time-dependent energy and frequency representation for the dynamic stall process.

2.4 Linear Stability Methods

One of the objectives of this study was to compare the velocity perturbation modes derived from a combined EMD and Hilbert transform approach, as described in Section 2.3, with the modal predictions of linear stability analysis. Unlike more sophisticated stability equations, such as the Parabolized Stability Equations, the fundamental equations in linear stability analysis are only applicable during the growth of small-amplitude perturbations in the flow. However, the linear stability methods were selected for the current study due to the ease of implementation and the demonstrated success in the literature for transition-based studies involving separated shear layers and laminar separation bubbles. [43–48] The detailed mathematical formulation and the numerical procedure for the implementation of linear stability analysis is described in this section.

2.4.1 Mathematical Formulation

The mathematical formulation for the stability analysis of prescribed velocity profiles is derived from the Navier-Stokes equations, which in its current reproduction, describe the motion of an incompressible, viscous fluid in two dimensions:

$$\frac{\partial u}{\partial x} + \frac{\partial v}{\partial y} = 0 \tag{2.47}$$

$$\frac{\partial u}{\partial t} + u\frac{\partial u}{\partial x} + v\frac{\partial u}{\partial y} = -\frac{\partial p}{\partial x} + \frac{1}{Re}\left(\frac{\partial^2 u}{\partial x^2} + \frac{\partial^2 u}{\partial y^2}\right) \tag{2.48}$$

$$\frac{\partial v}{\partial t} + u\frac{\partial v}{\partial x} + v\frac{\partial v}{\partial y} = -\frac{\partial p}{\partial y} + \frac{1}{Re}\left(\frac{\partial^2 v}{\partial x^2} + \frac{\partial^2 v}{\partial y^2}\right) \tag{2.49}$$

For simplicity, the variables in Eq. 2.47–2.49 have been non-dimensionalized using suitable length and velocity scales. The choice of these characteristic scales is discussed later in this section. The assumption of incompressibility introduces significant simplicity to the problem by decoupling the momentum equation in the full Navier-Stokes equation from the energy equation. This assumption is justified by the low Mach

number conditions of the freestream. The highest Reynolds number of the current dynamic stall experiments, $Re_c = 1.0 \times 10^6$, is associated with a freestream Mach number that is only as large as $M_\infty = 0.1$.

The growth of perturbations is calculated over a parallel base flow oriented along the x-axis, $u = U(y)$, $v = 0$. This base flow along with the corresponding pressure field, p, represents an equilibrium solution to Eq. 2.47–2.49. While a perfectly unidirectional base profile is not realized practically, previous studies in the literature have demonstrated that non-parallel flow effects do not contribute significantly to the disturbance growth in canonical shear layer profiles. [49,50] Thus, the predictions from linear stability analysis have been shown to remain valid for non-parallel base profiles. As the next step of this stability formulation, a set of small-amplitude perturbations is added to the equilibrium solution of Eq. 2.47–2.49:

$$u = U(y) + u' \tag{2.50}$$

$$v = v' \tag{2.51}$$

$$p = P + p' \tag{2.52}$$

These perturbed flow variables are introduced back into Eq. 2.47–2.49. The governing equations are subsequently simplified by eliminating the equilibrium solution and the second-order terms involving u', v', to obtain the linearized form of the Navier-Stokes equation about the base flow:

$$\frac{\partial u'}{\partial x} + \frac{\partial v'}{\partial y} = 0 \tag{2.53}$$

$$\frac{\partial u'}{\partial t} + U\frac{\partial u'}{\partial x} + v'\frac{\mathrm{d}U}{\mathrm{d}y} = -\frac{\partial p'}{\partial x} + \frac{1}{Re}\left(\frac{\partial^2 u'}{\partial x^2} + \frac{\partial^2 u'}{\partial y^2}\right) \tag{2.54}$$

$$\frac{\partial v'}{\partial t} + U\frac{\partial v'}{\partial x} = -\frac{\partial p'}{\partial y} + \frac{1}{Re}\left(\frac{\partial^2 v'}{\partial x^2} + \frac{\partial^2 v'}{\partial y^2}\right) \tag{2.55}$$

The perturbations, u', v', and p', are expanded across a normal basis, such that two distinct modes do not interact with each other. Moreover, for the idealized base flow, the perturbation growth is restricted in time or along the streamwise direction. Under these assumptions, each perturbation mode can be defined as:

$$u' = \hat{u}(y)e^{i(kx-\nu t)} \tag{2.56}$$

$$v' = \hat{v}(y)e^{i(kx-\nu t)} \tag{2.57}$$

$$p' = \hat{p}(y)e^{i(kx-\nu t)} \tag{2.58}$$

Substituting these quantities into Eq. 2.53–2.55 and solving for the perturbation amplitude, $\hat{v}(y)$, the linearized Navier-Stokes equations reduce to the Orr-Sommerfeld equation, which in the current form, governs the growth of two-dimensional, linear perturbations over a parallel base profile:

$$\left(U - \frac{\nu}{k}\right)\left(\frac{\mathrm{d}^2\hat{v}}{\mathrm{d}y^2} - k^2\hat{v}\right) - \frac{\mathrm{d}^2U}{\mathrm{d}y^2}\hat{v} = \frac{1}{ikRe}\left(\frac{\mathrm{d}^4\hat{v}}{\mathrm{d}y^4} - 2k^2\frac{\mathrm{d}^2\hat{v}}{\mathrm{d}y^2} + k^4\hat{v}\right) \tag{2.59}$$

A simpler, inviscid version of Eq. 2.59 known as the Rayleigh equation, has also been used in the literature for the stability analysis of separated shear layers. [44, 46, 47, 51] For the current study, however, the full Orr-Sommerfeld equation was used in order to include the effects of viscosity and obtain more accurate predictions from the stability analysis. A semi-infinite fluid domain is assumed in the current application with a rigid, impenetrable surface at $y = 0$. The perturbation amplitude is also assumed to decay as $y_{max} \to \infty$. Thus, a combination of no-slip and no-penetration boundary conditions is enforced, in the current problem, using:

$$\hat{v}(0) = \hat{v}(y_{max} \to \infty) = \frac{\mathrm{d}\hat{v}}{\mathrm{d}y}(0) = \frac{\mathrm{d}\hat{v}}{\mathrm{d}y}(y_{max} \to \infty) = 0 \tag{2.60}$$

The Orr-Sommerfeld equation, together with the boundary conditions from Eq. 2.60 form an eigenvalue system, which can be solved to obtain the eigenvalues $k \in \mathbb{C}$, and the corresponding eigenfunctions, $\hat{v}(y)$. The set of all such possible combinations of $\nu, k, \hat{v}(y)$ that solve the governing equations, Eq. 2.59 and Eq. 2.60, define an instability or eigenvalue spectrum for a fixed base profile. The solution to the Orr-Sommerfeld equation involves two distinct possibilities. A temporal or absolute instability analysis seeks to find solutions for which $k \in \mathbb{R}$, thereby restricting the growth of instabilities to only the time domain. The spatial or convective instability analysis, in contrast, considers solutions for which $\nu \in \mathbb{R}$, thus, restricting the amplitude growth to the spatial domain. It should also be noted that a more general analysis of the linear disturbance growth on a parallel base flow involves a perturbation that depends on three spatial dimensions. It can however, be demonstrated using Squires' transformation that each unstable, three-dimensional mode of the Orr-Sommerfeld equation is associated with a significantly more unstable two-dimensional mode. [52,53] Thus, the two-dimensional formulation of the current investigation was deemed sufficient in accurately predicting the instability spectra of the desired base velocity profile.

2.4.2 Base Flow Considerations

Due to the sensitivity of the numerical derivatives to scatter in the experimentally-acquired base flow, the present implementation of linear stability analysis was performed over an analytical curve that was fitted

over the acquired velocity profile. Several analytical profiles of varying complexity, ranging from a simple cubic spline to a more complicated logistic series fit, have been used in the literature to approximate a separated shear layer velocity profile, as outlined in [48]. Based on the recommendations of Boutilier and Yarusevych, [48] a modified version of the hyperbolic tangent fit, originally proposed by Dovgal et al. [51] and Dini et al., [54] was used in the current investigation. The hyperbolic tangent fit is defined mathematically as:

$$u_a(y) = a_1(1 + \tanh(a_2 y + a_3)) + a_4 y + a_5 \tag{2.61}$$

Besides sufficient smoothness and differentiability, this curve fit was selected due to the ease of implementation and the demonstrated higher tolerance to experimental scatter. [48] A least squares curve fitting procedure was used to fit the analytical profile from Eq. 2.61 to the acquired velocity data. In this curve-fitting method, a measure of the deviation between the real data and the fitted curve is obtained through the following quantity:

$$R^2 = \sum_i \left[u_e(y_i) - u_a(y_i)\right]^2 \tag{2.62}$$

where u_e denotes the experimentally-determined velocity profile. In order to minimize the error R^2 ,from Eq. 2.62, the derivatives $\frac{\mathrm{d}R^2}{\mathrm{d}a_n}$ for $n \in [1, 5]$, are set identically to zero which produces a system of equations that can be solved to obtain the hyperbolic-tangent coefficients a_n. An example hyperbolic tangent fit for a velocity profile extracted at $x/c = -0.15$, corresponding to an angle of attack of $\alpha = 20.63°(Re_c = 0.5 \times 10^6)$, is presented in Fig. 2.13. It should be mentioned that the origin of the y axis in Fig. 2.13 has been redefined such that it lies on the surface of the airfoil mask.

It should also be mentioned that the Orr-Sommerfeld equation of the form presented in Eq. 2.59 is valid for base flows that do not vary with time. A dynamic stall process is however, associated with a non-stationary velocity field that varies significantly with time. However, the time scale associated with the growth of perturbations, which is proportional to the inverse of the velocity difference in a canonical mixing layer, $(\Delta u)^{-1}$, is expected to be significantly smaller than the characteristic time scale associated with the flowfield, $(\Omega)^{-1}$. Thus, the base flow is expected to remain largely unchanged during the exponential growth phase of an initial small-amplitude perturbation.

2.4.3 Numerical Implementation

A spectral method was used to compute the solutions to the Orr-Sommerfeld equation for a fixed base profile. In this method, the desired solution is approximated as a series of orthogonal test functions. A finite set of Chebyshev polynomials was used as test functions in the current investigations due to their

rapid convergence, i.e., the solution can be made to converge by considering only a few terms in the series expansion. These polynomials have also been used widely in the literature for numerical implementation of linear stability analysis. [55–59] The n^{th} Chebyshev polynomial is defined as:

$$T_n(y) = \cos\left[(n-1)\arccos(y)\right] \tag{2.63}$$

The perturbation amplitude, $\hat{v}$ from Eq. 2.59 is then defined as the linear sum of a finite number of Chebyshev polynomials using the following equation:

$$\hat{v}(y) = \sum_{n=1}^{N+1} d_n T_n(y) \tag{2.64}$$

where d_n is the coefficient associated with the n^{th} Chebyshev polynomial. It is important to note that the Chebyshev polynomial is defined for $y \in [-1, 1]$. The physical variable y from Eq. 2.59 is however, defined across a semi-infinite domain, i.e., $y \in [0, y_{max} \to \infty]$. Thus, in order to successfully incorporate the Chebyshev expansion of the velocity perturbation from Eq. 2.64 into Eq. 2.59, a coordinate transformation was defined to map the physical domain, y, into the Chebyshev domain, $\hat{y}$:

$$\hat{y} = y\xi - 1 \tag{2.65}$$

where $\xi = 2/y_{max}$. The Orr-Sommerfeld equation was reformulated using this coordinate transformation to yield:

$$\left(U - \frac{\nu}{k}\right)\left(\xi^2 \frac{\mathrm{d}^2\hat{v}}{\mathrm{d}\hat{y}^2} - k^2\hat{v}\right) - \frac{\mathrm{d}^2 U}{\mathrm{d}y^2}\hat{v} = \frac{1}{ikRe}\left(\xi^4 \frac{\mathrm{d}^4\hat{v}}{\mathrm{d}\hat{y}^4} - 2k^2\xi^2 \frac{\mathrm{d}^2\hat{v}}{\mathrm{d}\hat{y}^2} + k^4\hat{v}\right) \tag{2.66}$$

The boundary conditions, from Eq. 2.60, are also reformulated to comply with the domain of definition of the Chebyshev polynomials, as defined below:

$$\hat{v}(\pm 1) = \frac{\mathrm{d}\hat{v}}{\mathrm{d}\hat{y}}(\pm 1) = 0 \tag{2.67}$$

For numerical implementation of Eq. 2.66, the spatial variable, y is discretized into a series of points, which are commonly referred to as collocation points. These collocation points, $\hat{y}_m$ are selected to correspond to the location of extrema of the highest order Chebyshev polynomial, $T_{N+1} = \cos\left[(N)\arccos(\hat{y})\right]$ that is used in the expansion of $\hat{v}(\hat{y})$:

$$\hat{y}_m = \cos(\frac{m\pi}{N}) \tag{2.68}$$

where $m \in \mathbb{Z}$. The governing differential equation, which is applied at discrete collocation points, together with the boundary conditions, Eq. 2.66 and Eq. 2.67, form a system of linear algebraic equations that can be solved for either the absolute or the convective instability of a given base profile. It should be recalled that for absolute instability, a fixed wavenumber $k \in \mathbb{R}$ is pre-selected and the system of equations is solved to obtain the unknown angular frequencies, ν, and the eigenfunctions, $\hat{v}$. In matrix form, this system of equations can be written as:

$$(A - \nu B)\mathbf{d} = 0 \tag{2.69}$$

The imaginary part of the angular frequency, $\mathrm{Im}(\nu)$ or ν_i, defines the growth rate of the perturbation amplitude in time. Thus, an unstable base profile in time is associated with an angular fequency, ν, such that $\nu_i > 0$. The letters A and B correspond to matrices of size $(N+1) \times (N+1)$. In the interior of the $\hat{y}_m$ domain, i.e., for $(m+1) \in [3, N-1]$ and $n \in [1, N+1]$, the A and B matrices are defined as:

$$A_{m+1,n} = \frac{i}{Re}\xi^4 \frac{\mathrm{d}^4 T_n}{\mathrm{d}\hat{y}^4}(\hat{y}_m) + \left(k\xi^2 U(y_m) - i\frac{2k^2\xi^2}{Re}\right)\frac{\mathrm{d}^2 T_n}{\mathrm{d}\hat{y}^2}(\hat{y}_m) + \left(\frac{ik^4}{Re} - k^3 U(y_m) - k\frac{\mathrm{d}^2 U}{\mathrm{d}y^2}(y_m)\right) T_n(\hat{y}_m) \tag{2.70}$$

$$B_{m+1,n} = \xi^2 \frac{\mathrm{d}^2 T_n}{\mathrm{d}\hat{y}^2}(\hat{y}_m) - k^2 T_n(\hat{y}_m) \tag{2.71}$$

with the boundary conditions enforced on the first two and the last two rows of the matrices A and B, as shown below:

$$A_{1,n} = T_n(-1) \tag{2.72}$$

$$A_{2,n} = \frac{\mathrm{d}T_n}{\mathrm{d}\hat{y}}(-1) \tag{2.73}$$

$$A_{N,n} = T_n(1) \tag{2.74}$$

$$A_{N+1,n} = \frac{\mathrm{d}T_n}{\mathrm{d}\hat{y}}(1) \tag{2.75}$$

and $B = 0$ for $(m+1) = 1, 2, N, N+1$

For convective instability, the angular frequency $\nu \in \mathbb{R}$ is predefined, and the system of equations is solved for unstable wavenumbers, $\mathrm{Im}(k)$ or $k_i < 0$, and the corresponding eigenfunctions, $\hat{v}$. Similar to Eq. 2.69, the set of equations governing the convective instability of a base profile can also be written in matrix form as presented below:

$$(C_0 k^4 + C_1 k^3 + C_2 k^2 + C_3 k + C_4)\mathbf{d} = 0 \tag{2.76}$$

For $(m+1) \in [3, N-1]$ and $n \in [1, N+1]$, the matrices C_0 through C_4 are defined as:

$$C_{0_{m+1,n}} = \frac{i}{Re} T_n(\hat{y}_m) \tag{2.77}$$

$$C_{1_{m+1,n}} = -U(y_m) T_n(\hat{y}_m) \tag{2.78}$$

$$C_{2_{m+1,n}} = \nu T_n(\hat{y}_m) - i\frac{2\xi^2}{Re} \frac{\mathrm{d}^2 T_n}{\mathrm{d}\hat{y}^2}(\hat{y}_m) \tag{2.79}$$

$$C_{3_{m+1,n}} = U(y_m)\xi^2 \frac{\mathrm{d}^2 T_n}{\mathrm{d}\hat{y}^2}(\hat{y}_m) - \frac{\mathrm{d}^2 U}{\mathrm{d}y^2}(y_m) T_n(\hat{y}_m) \tag{2.80}$$

$$C_{4_{m+1,n}} = i\frac{\xi^4}{Re} \frac{\mathrm{d}^4 T_n}{\mathrm{d}\hat{y}^4}(\hat{y}_m) - \nu\xi^2 \frac{\mathrm{d}^2 T_n}{\mathrm{d}\hat{y}^2}(\hat{y}_m) \tag{2.81}$$

As with Eq. 2.69, the boundary conditions are enforced on the first and the last two rows of the C matrices, using the following relations:

$$C_{4_{1,n}} = T_n(-1) \tag{2.82}$$

$$C_{4_{2,n}} = \frac{\mathrm{d}T_n}{\mathrm{d}\hat{y}}(-1) \tag{2.83}$$

$$C_{4_{N,n}} = T_n(1) \tag{2.84}$$

$$C_{4_{N+1,n}} = \frac{\mathrm{d}T_n}{\mathrm{d}\hat{y}}(1) \tag{2.85}$$

with $C_0 = C_1 = C_2 = C_3 = 0$ for $(m+1) = 1, 2, N, N+1$

In the current investigation, select base flow profiles, acquired using TR-PIV, were analyzed for two-dimensional, convectively-unstable, velocity perturbation modes using a numerical routine that was developed to solve Eq. 2.76. The shear layer displacement thickness, δ^* and the maximum velocity, u_{max}, were used as characteristic length and velocity scales for the non-dimensional quantities in Eq. 2.66. These quantities, shown in Fig. 2.13, were selected since they were considered more physically relevant to the natural scales associated with the a separated shear layer profile, as opposed to the airfoil chord length and the freestream velocity. The displacement thickness, in the current study, was defined using the following equation:

$$\delta^* = \int_0^{y_{max}} \left(1 - \frac{u(y)}{u_{max}}\right) \mathrm{d}y \tag{2.86}$$

where y_{max} corresponds to the location where $u(y_{max}) = u_{max}$.

As a final note, it is important to mention that a numerical implementation of Eq. 2.76 is usually associated with a set of spurious eigenvalue estimates. These innaccurate estimates of the perturbation modes associated with linear stability analysis are well-documented in the literature. [60–62] A Gaster's

transformation-based approach was used in this study to extract the physically-real modes from the inaccurate numerical artifacts. Gaster's transformation is an approximate relationship that connects the temporal growth rate, ν_i, with the spatial growth rate, k_i. For a given base flow and Reynolds number, the Orr-Sommerfeld equation, from Eq. 2.59, reduces to a dispersion relationship of the form $F(k, \nu) = 0$. This dispersion relation can be solved for the angular frequency, ν, as a well-behaved analytic function of the wavenumber, k, i.e., $\nu = \nu(k)$. Since an analytic function satisfies the Cauchy-Riemann relationship, the solution $\nu = \nu(k)$ to the dispersion relation leads to the following equality:

$$\frac{\partial \nu_r}{\partial k_r} = \frac{\partial \nu_i}{\partial k_i} \tag{2.87}$$

where ν_r and k_r correspond to $\mathrm{Re}(\nu)$ and $\mathrm{Re}(k)$, respectively. The Cauchy-Riemann relation, Eq. 2.87, can then be integrated along a fixed k_r path, from an initial state, defined by $\nu_i = 0, k_i = k_i$, to a final state, $\nu_i = \nu_i, k_i = 0$, as shown below:

$$\nu_i = -\int_0^{k_i} \frac{\partial \nu_r}{\partial k_r} \mathrm{d}k_i \tag{2.88}$$

Assuming a constant $\frac{\partial \nu_r}{\partial k_r}$, which forms a valid approximation for small values of k_i, the integral can be evaluated to obtain the desired Gaster's transformation:

$$\nu_i \approx \frac{\partial \nu_r}{\partial k_r}(-k_i) \tag{2.89}$$

Thus, in addition to solving for the spatial growth rate, k_i, the numerical formulation for the absolute instability of the base profile was also implemented, using Eq. 2.69, to estimate the temporal growth rate, ν_i. From the complete spectrum of eigenvalue estimates, only the k_i and ν_i combinations that satisfied Eq. 2.89 were selected as physically-real estimates for further analysis. The results from the stability analysis are presented in Section 3.4 as a variation in the growth rate, $-k_i$ as a function of the displacement-thickness based Strouhal number, St_{δ^*}. This second Strouhal scaling was calculated using:

$$St_{\delta^*} = \frac{f\delta^*}{u_{max}} = \frac{\nu_r}{2\pi} \tag{2.90}$$

2.5 Statistics and Uncertainty

The set of physical quantities or parameters, Q_p, which includes $C_p(t)$, $C_l(t)$, $C_m(t)$, $V(x, y, t)$, and $\omega_z(x, y, t)$, were phase averaged or ensemble averaged over several experimental realizations. The phase-averaging process was intended to reduce the influence of the sampling uncertainty from the acquired measurements

and to better characterize the recurring variations during the dynamic stall process. The pressure-based results, C_p, C_l, and C_m were phase-averaged over 25 experimental runs or realizations, whilst the TR-PIV acquisition parameters, V, and ω_z were phase-averaged over 10 independent experimental realizations. From a mathematical standpoint, the phase-averaging procedure attempts to calculate the expected values of the physical parameters, $\mathbb{E}[Q_p]$, using the following equation:

$$\mathbb{E}[Q_p] \approx \overline{Q_p} = \frac{1}{N_{exp}} \sum_{i=1}^{N_{exp}} Q_{p_i} \tag{2.91}$$

where N_{exp} denotes the total number of independent experimental realizations: $N_{exp} = 25$ for $Q_p \in \{C_p, C_l, C_m\}$, and $N_{exp} = 10$ for $Q_p \in \{V, \omega_z\}$. Q_{p_i} corresponds to the measurements of the physical quantities that were acquired during the i^{th} experimental run. The phase-averaged energy measure, $\overline{E}$, for the pressure and velocity fluctuations were also calculated using an equivalent form of Eq. 2.91. In contrast, the frequency measure for the pressure and velocity fluctuations was calculated using an energy-weighted averaging procedure, as defined by:

$$\overline{f} = \frac{\sum_{i=1}^{N_{exp}} E_i f_i}{\sum_{i=1}^{N_{exp}} E_i} \tag{2.92}$$

where N_{exp} is associated with the same definition as in Eq. 2.91, wherein $N_{exp} = 25$ for the pressure-based spectra, and $N_{exp} = 10$ for the velocity spectra. An energy-weighted averaging process was used for the spectral frequencies in order to minimize the contribution of the low-amplitude background noise, and help provide an improved representation of the physical modes of perturbations in the flow. The corresponding phase-averaged Strouhal values, $\overline{St}$, were calculated from the phase-averaged frequencies, using an appropriate scaling definition from Eq. 2.24, Eq. 2.25, and Eq. 2.90.

The root-mean-square of the acquired pressure measurements, $C_{p,rms}$, was used to gain an elementary understanding of the progression of unsteadiness in the surface pressure field. This statistical quantity was calculated using the following equation:

$$C_{p,rms} = \sqrt{\frac{1}{N_{exp}} \sum_{i=1}^{N_{exp}} \left(C_{p_i} - C_{p_{i,f}}\right)^2} \tag{2.93}$$

where $C_{p_{i,f}}$ corresponds to the low-pass filtered surface pressure coefficient, which was obtained by applying a Savitzky-Golay filter to the acquired C_p from the i^{th} experimental run. In this filter, a pre-defined sliding kernel is used to extract a successive sub-sets of data points from an input signal. A polynomial curve fit is performed over each sub-set following a least-squares curve fitting procedure, which was described previously in reference to Eq. 2.62. A Savitzky-Golay filter was used in this study since it was found to be

effective in extracting the high-frequency oscillations whilst preserving the non-stationary character of the surface pressure evolution during the dynamic stall process. A fourth-degree polynomial with a kernel size of 5% relative to the total length of the input pressure signal was used in the current implementation of the Savitzky-Golay filter. The current method for the estimation of $C_{p,rms}$, as described by Eq. 2.93, was employed for this study, since it helps extract the high-frequency unsteadiness in C_p which stems from local, transient flow structures of interest.

The uncertainties associated with the phase-averaged quantities, which corresponds statistically to the standard deviation of the mean, was calculated using the following equation:

$$U_{Q_p} = t^d_{(N_{exp}-1,\alpha_{ci})} \frac{\sigma_{std}}{\sqrt{N_{exp}}} \tag{2.94}$$

where $t^d_{(N_{exp}-1)}$ denotes the student t-distribution for $N_{exp} - 1$ degrees of freedom. Stated differently, $t^d_{(N_{exp}-1)}$ describes the continuous probability distribution associated with a set of N_{exp} samples that are drawn randomly from a normal distribution. The two-sided t^d value was estimated for a desired confidence interval, α_{ci} using standard tables in the literature. [63] The quantity σ_{std} corresponds to the sample standard deviation, which for a given parameter, Q_p, was estimated using the following equation:

$$\sigma_{std} = \sqrt{\frac{1}{N_{exp}-1} \sum_{i=1}^{N_{exp}} \left(Q_{p_i} - \overline{Q_p}\right)^2} \tag{2.95}$$

A set of reference uncertainties for select phase-averaged parameters from the set Q_p is presented in Table 2.1.

The uncertainty for the instantaneous velocity field, corresponding to a single instance of the measurement process, was estimated following the steps outlined by Wieneke. [64] In this approach, the measure of uncertainty is obtained by calculating the asymmetry in the cross-correlation peak that is used to estimate the instantaneous velocities, as had been described previously in relation to Eq. 2.36. The instantaneous velocity uncertainties at select angles of attack, representing three distinct phases of the dynamic stall process at $Re_c = 0.5 \times 10^6$, are presented in Fig. 2.14. These uncertainty estimates are presented in terms of a percentage of the freestream velocity at $Re_c = 0.5 \times 10^6$. From Fig. 2.14, the uncertainties associated with the complex, rapidly evolving flow near the airfoil leading edge dominates that of the largely inviscid freestream. However, the estimated uncertainties are found to be within reasonable limits, with the maximum uncertainty being less than 5% of the freestream velocity.

2.6 Tables and Figures

Table 2.1: Reference uncertainties associated with select phase-averaged parameters.

Parameter	$Re_c(\times 10^6)$	Reference α°	Reference value	Absolute uncertainty
C_l	0.5	26.14	2.37	± 0.02
C_m	0.5	26.94	-0.50	± 0.01
C_p	0.5	17.97	-7.63	± 0.07
C_l	1.0	25.03	2.57	± 0.01
C_m	1.0	26.09	-0.37	± 0.01
C_p	1.0	23.67	-14.98	± 0.03

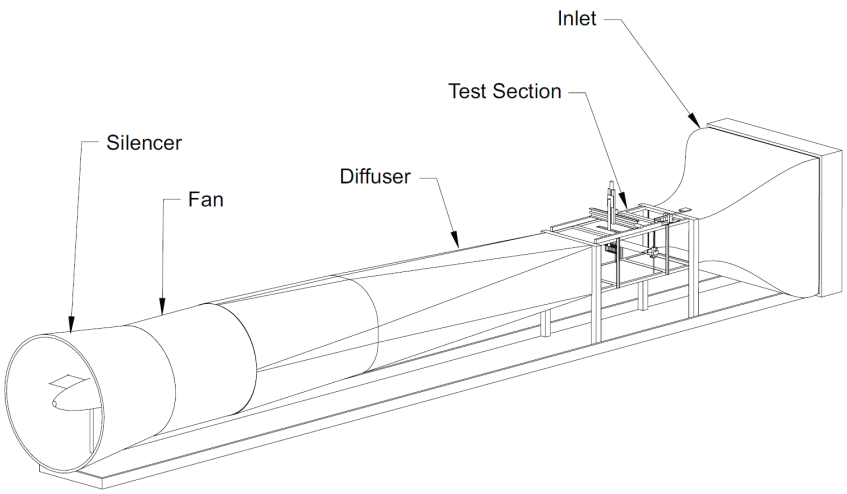

Figure 2.1: Schematic of the 0.9 m by 1.2 m subsonic wind tunnel.

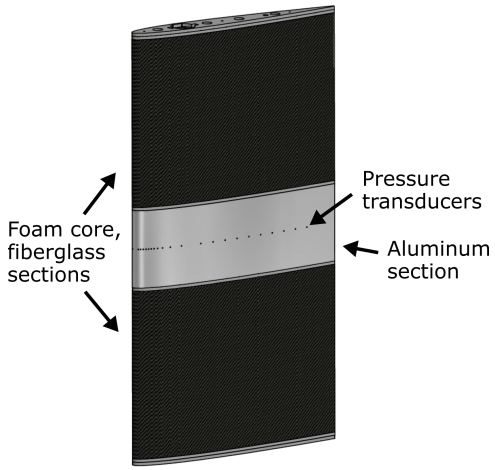

Figure 2.2: A computer rendering of the airfoil model used in the present experiments.

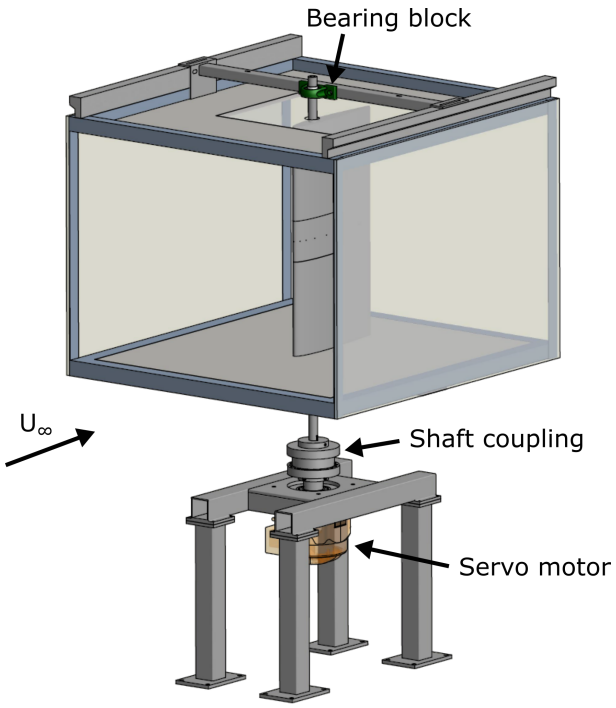

Figure 2.3: A CAD assembly showing the installation of the airfoil model in the test section.

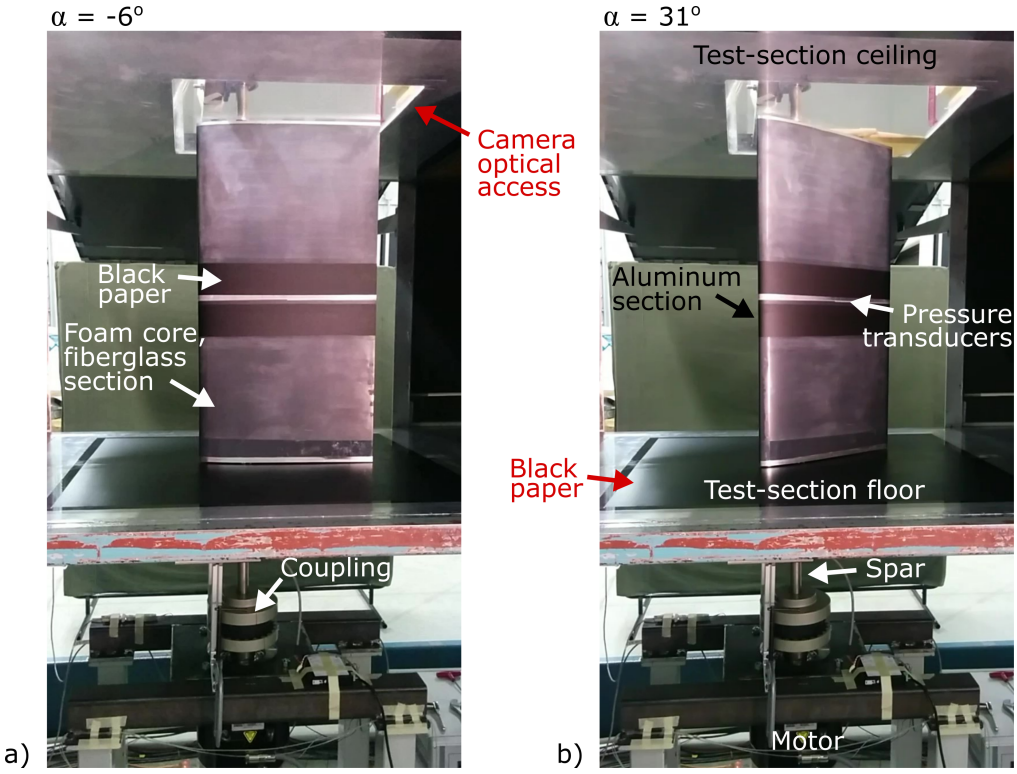

Figure 2.4: Photographs of the dynamic stall setup with the airfoil model oriented at a) $\alpha = -6°$, and b) $\alpha = 31°$.

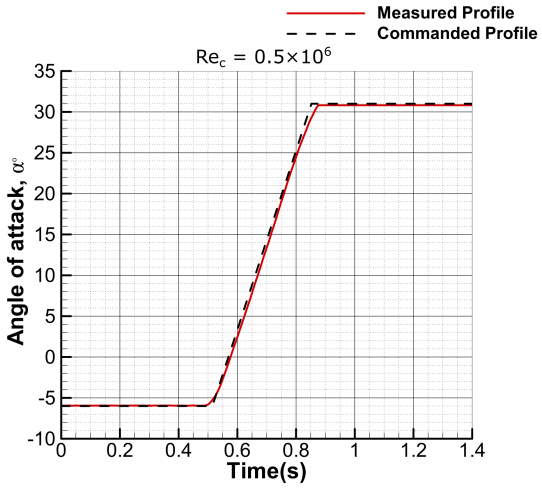

Figure 2.5: Time traces of the commanded and the acquired motion profiles for an $\Omega^+ = 0.05$ linear ramp maneuver at $Re_c = 0.5 \times 10^6$.

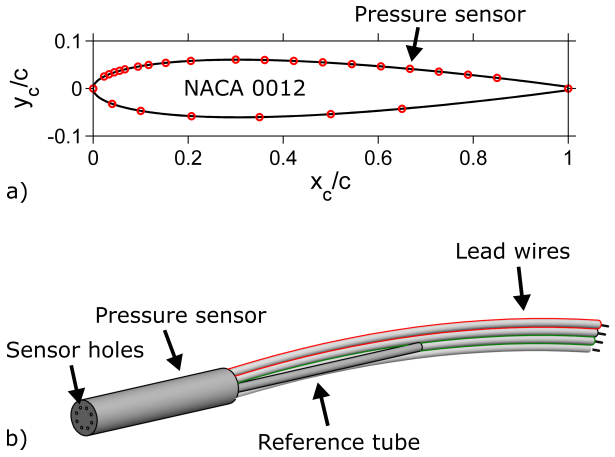

Figure 2.6: a) Distribution of pressure transducers across the airfoil surface, and b) a computer rendering of an individual pressure transducer used in the current study.

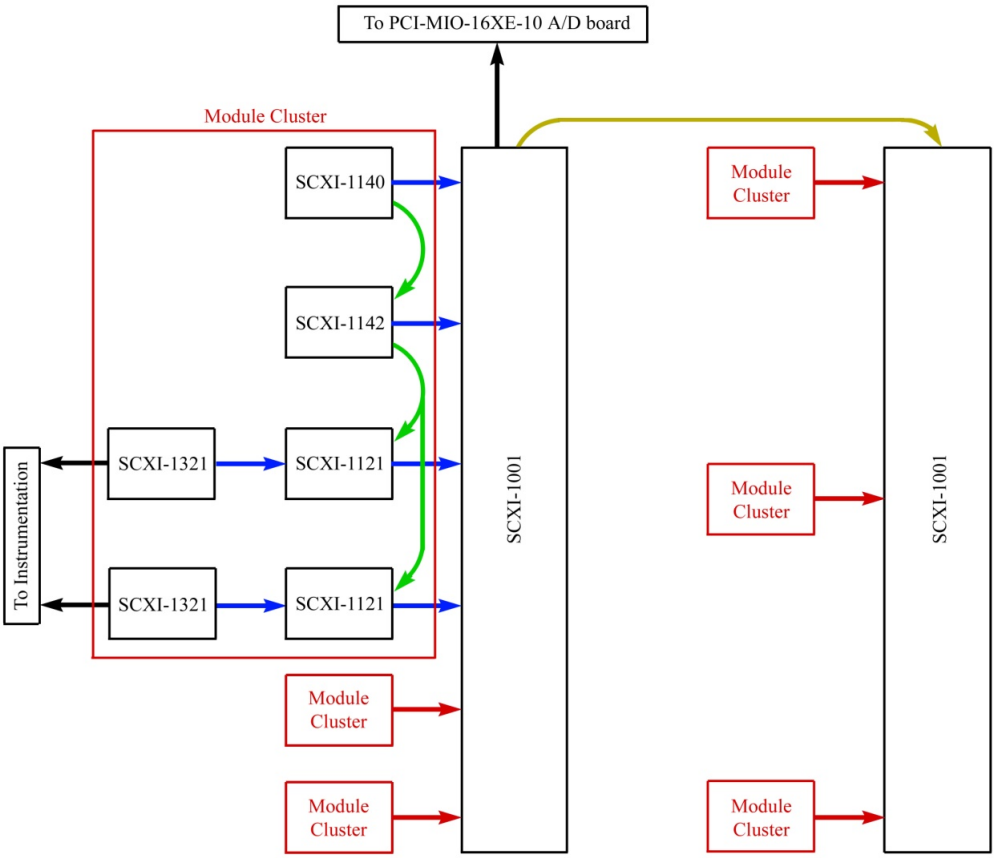

Figure 2.7: A schematic of the SCXI modules and chassis connections, after Ansell. [2]

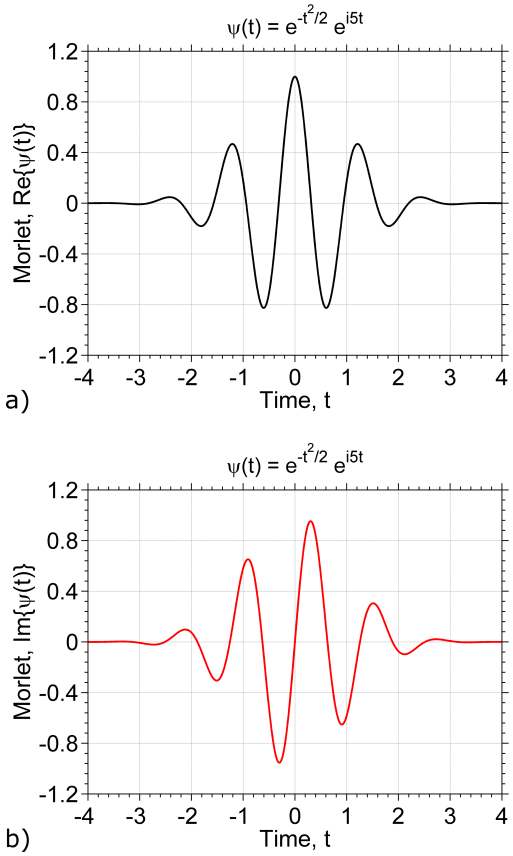

Figure 2.8: a) Real and b) Imaginary components of a sample Morlet wavelet function in the time domain.

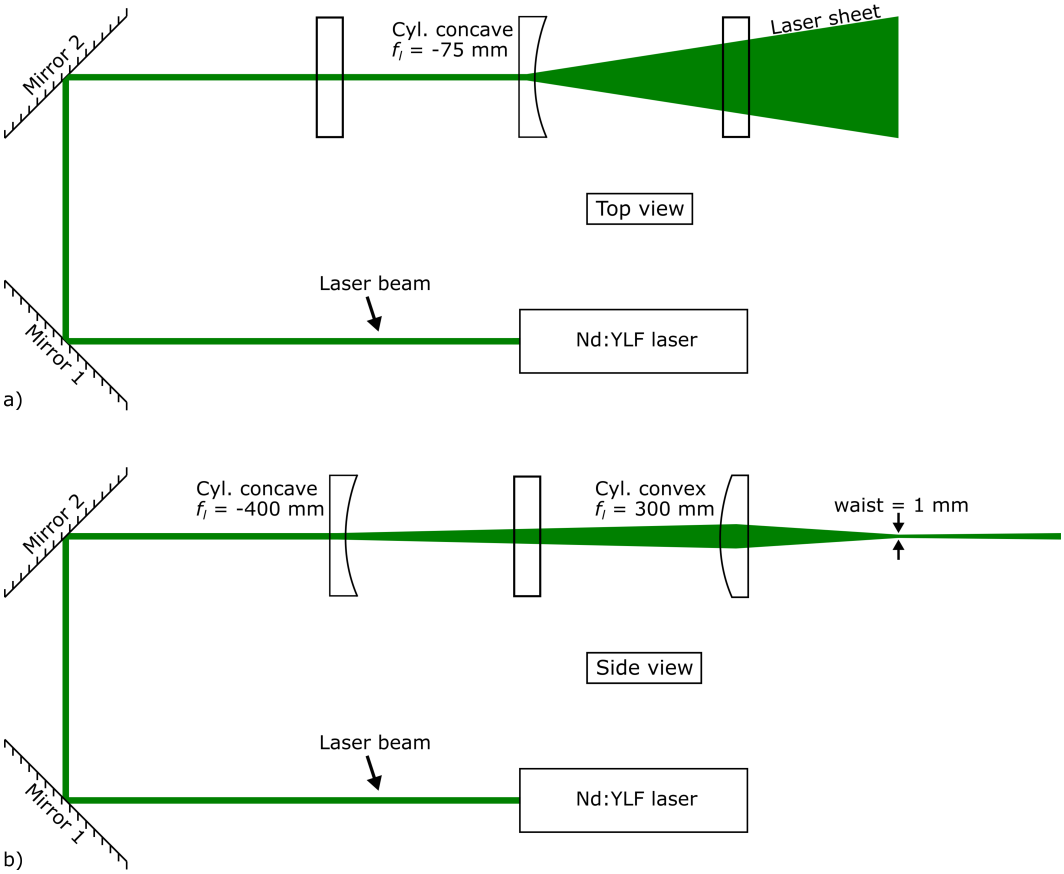

Figure 2.9: Schematic a) top and b) side views of the laser sheet formation process.

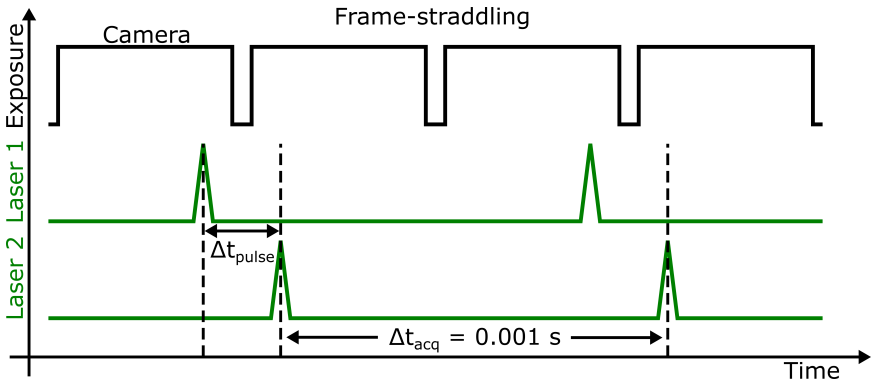

Figure 2.10: Laser and camera timing setup for TR-PIV acquisition in the frame-straddling mode.

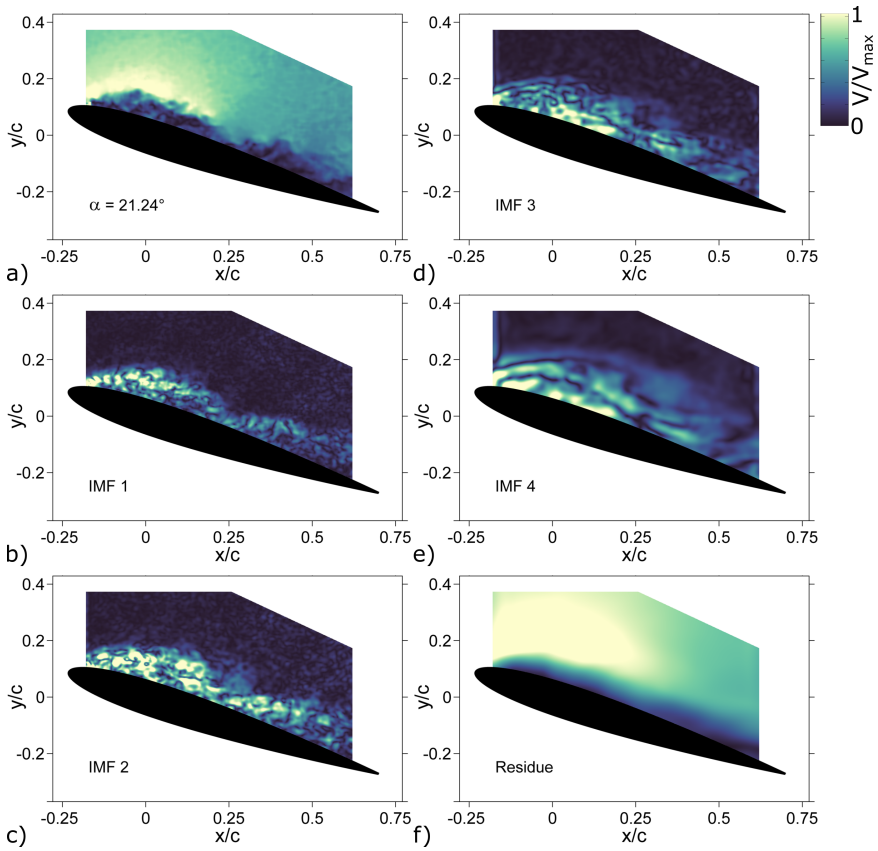

Figure 2.11: Instantaneous velocity at $\alpha = 21.24°$ along with the EMD-derived IMFs and the Residue ($Re_c = 0.5 \times 10^6$).

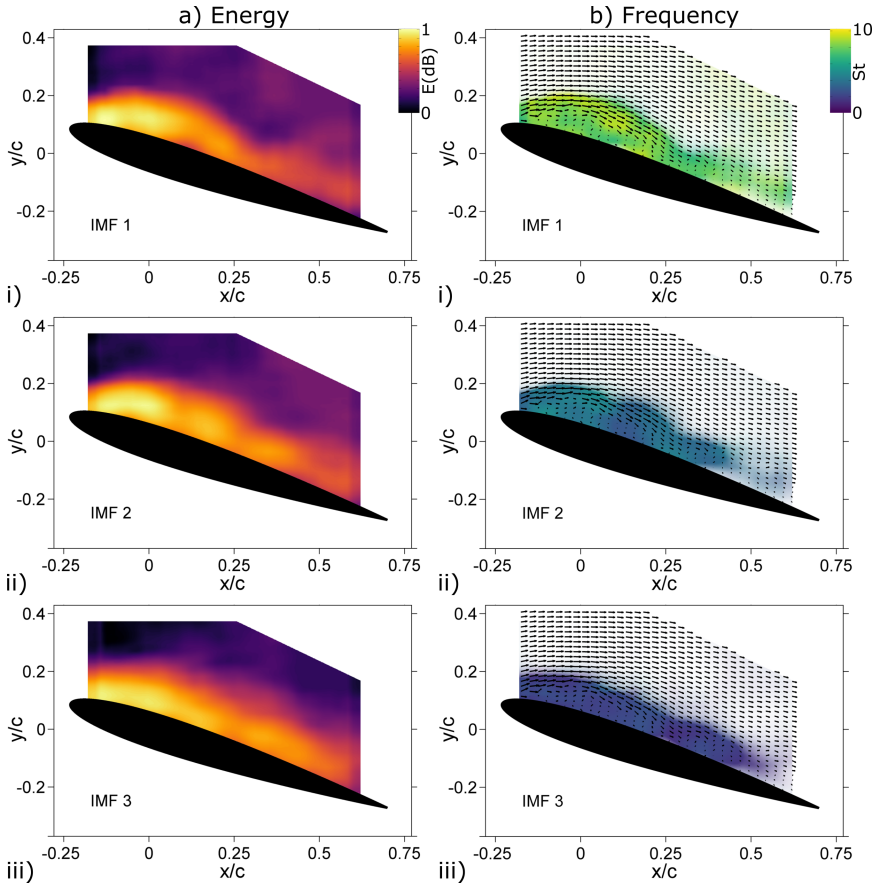

Figure 2.12: Instantaneous a) energy and b) frequency contours associated with the first three IMFs from Fig. 2.11.

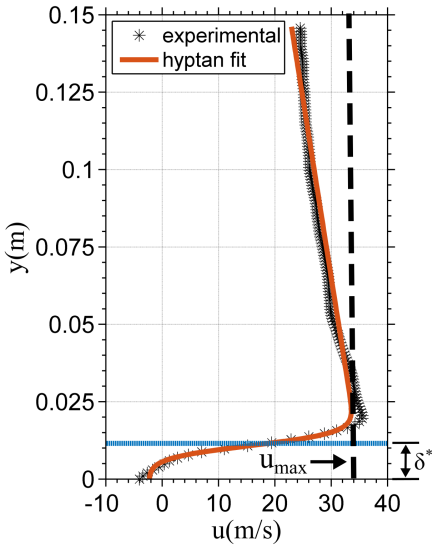

Figure 2.13: Comparison between the experimentally-acquired u-velocity ($x/c = -0.15$, $\alpha = 20.63°$, $Re_c = 0.5 \times 10^6$) and the associated hyperbolic tangent fit determined using Eq. 2.61.

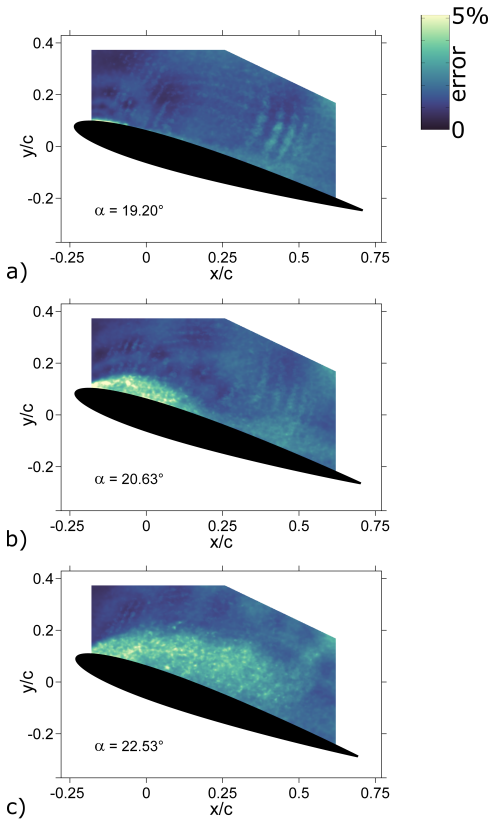

Figure 2.14: Instantaneous uncertainties in the velocity field measurements, relative to the freestream, at select angles of attack ($Re_c = 0.5 \times 10^6$).

Chapter 3

Results

The results of the experiments and the analysis techniques described previously in Chapter 2 are presented in this chapter. Initially, the dynamic stall process at $Re_c = 0.5 \times 10^6$ is analyzed in detail. As such, the results presented in Sections 3.1–3.2 correspond exclusively to the dynamic stall process at $Re_c = 0.5 \times 10^6$. It should also be noted that unless specified otherwise, the results from this chapter do not correspond to a single instance of the dynamic stall process, but were rather obtained by phase-averaging the corresponding physical quantities of interest over several experimental realizations, as described in Chapter 2. As such, the quantities $\overline{Q_p}$ where $Q_p \in \{C_p, C_l, C_m, V, \omega_z\}$, $\overline{E}$, and $\overline{St}$ are referred to as Q_p, E, and St, for simplicity. A detailed comparison of the dynamic stall processes at $Re_c = 0.2 \times 10^6$, $Re_c = 0.5 \times 10^6$, and $Re_c = 1.0 \times 10^6$ is presented thereafter in Section 3.3. It should be noted that all of the uncertainty values reported in this chapter define a 68% confidence interval about the corresponding mean of the physical quantity.

3.1 Surface Pressure Results

The acquired surface pressure evolution and the associated pressure-derived quantities for the dynamic stall process at $Re_c = 0.5 \times 10^6$ are detailed in this section.

3.1.1 Airfoil Performance

The unsteady lift and quarter-chord pitching moment coefficients for the NACA 0012 airfoil at $Re_c = 0.5 \times 10^6$ are presented in Fig. 3.1 a) and Fig. 3.1 b) respectively. These performance coefficients were derived from the surface pressure measurements and are provided for both the clean airfoil model and for the model configured with a BL-trip, which is also referred to as the tripped airfoil configuration. The details with regards to the calculation of the performance coefficients and the BL-trip installation are provided in Chapter 2. For the purposes of comparison, the steady performance of the airfoil model, acquired for a time-independent angle of attack, in the clean configuration, is also included in Fig. 3.1. Under steady conditions, the airfoil is observed, from Fig. 3.1 a), to attain a maximum lift coefficient of $C_{l,max} = 1.18$. The corresponding

stall angle of attack is equal to $\alpha_{stall} = 12.63°$. The quarter-chord pitching moment coefficient, under the same steady conditions, is measured trivially at $C_m \approx 0$, for $\alpha < \alpha_{stall}$. The marginal deviation in the pitching moment from the expected zero level can be attributed to the difference in the number of pressure transducers installed on the upper and lower surfaces of the airfoil.

In contrast with the steady measurements, the unsteady performance of the airfoil model for both the clean and tripped configurations is characterized by large overshoots in the magnitude of lift and pitching moment coefficients, and a significant delay in stall. An interesting feature of the lift polars for both airfoil configurations is the distinct increase in the lift-curve slope that occurs before stall, as indicated in Fig. 3.1 a). For the tripped airfoil however, this event appears earlier, by approximately $\Delta\alpha \approx 1.3°$, in comparison with the clean configuration. The increase in the lift slope is conjectured to result from a rapid spatial growth of the DSV, which causes increased suction across the upper surface of the airfoil. While the unsteady performance polars for both airfoil configurations are qualitatively similar, there exists some notable quantitative differences. From Fig. 3.1, the maximum lift coefficient associated with the clean airfoil, $C_{l,max} = 2.37 \pm 0.02$, is observed to be noticeably greater than the corresponding maximum for the tripped airfoil, which is limited at $C_{l,max} = 2.12 \pm 0.02$. The lift stall angle of attack for the clean airfoil is observed, from Fig. 3.1 a), to occur at $\alpha_{stall} = 26.14°$. This value of α_{stall} is significantly greater than the corresponding measurement of $\alpha_{stall} = 23.92°$, which was acquired for the tripped airfoil. Thus, the addition of the BL-trip promotes early stall and leads to a reduction in the maximum lift that is attained by the airfoil. A similar trend is observed for the quarter-chord pitching moment coefficient. The tripped airfoil $C_{m,min} = -0.40 \pm 0.01$ is observed to be noticeably lower in magnitude in comparison with the minimum pitching moment coefficient for the clean airfoil, which equals $C_{m,min} = -0.50 \pm 0.01$. Furthermore, the angle of attack corresponding to $C_{m,min}$, referred to here as α_{min}, is also significantly lower for the tripped case, with $\alpha_{min} = 25.07°$, in comparison with the clean airfoil $\alpha_{min} = 26.94°$.

3.1.2 Pressure Evolution

A surface contour of the time-dependent pressure, $C_p(x_c, \alpha)$, acquired across the airfoil upper surface at $Re_c = 0.5 \times 10^6$ is presented in Fig. 3.2 a). For additional clarity, a two-dimensional projection of this contour in the vicinity of the leading-edge region of the airfoil, between $x_c/c = 0$ and $x_c/c = 0.3$, and across $\alpha = 5°$ and $\alpha = 25°$ is presented in Fig. 3.2 b). It should be noted that the data presented in Fig. 3.2 correspond to the airfoil model in the clean configuration. The surface pressure distributions at select instances of the dynamic stall process, corresponding to a fixed set of angles of attack, are presented in Fig. 3.3. For $\alpha = 10.73°$ and $\alpha = 17.97°$, which is shown in Fig. 3.3 b) and 3.3 e), the chordwise pressure

distributions for the tripped airfoil have also been included for the purposes of comparison. The location of the pressure transducers on the airfoil surface has been indicated in Fig. 3.2 b) and Fig. 3.3. The discussion in relation to the behavior of the unsteady separation is supported by the off-body velocity acquisition, which is presented later in Section 3.2.

From Fig. 3.2, the initial phase of the dynamic stall pitch cycle is characterized by a monotonic growth in suction near the airfoil leading edge. A sample pressure distribution during this initial, largely inviscid phase of the dynamic stall process is presented in Fig. 3.3 a). An increase in the airfoil angle of attack to $\alpha = 10.73^{\circ}$ is accompanied by the development of a characteristic pressure plateau. This near-constant pressure region can easily be identified in Fig. 3.3 b). The pressure plateau has been associated in the literature [18, 19, 23, 24] with an LSB, which for the present study forms near the airfoil leading edge. The reattachment of the separated shear layer, after initial separation, is associated with rapid pressure recovery, as indicated in Fig. 3.3 b). In contrast with the clean airfoil, the tripped airfoil pressure distribution at $\alpha = 10.73^{\circ}$ is not associated with a similar pressure plateau, as seen again in Fig. 3.3 b). Thus, the installation of the BL trip leads presumably, to a forced transition of the boundary layer, which in turn inhibits the LSB formation near the airfoil leading edge. The suction peak for the tripped airfoil however, dominates that of the clean airfoil, as observed in Fig. 3.3 b) in the absence of reduced effective curvature due to the LSB. The combined set of observations in relation to the initial pressure evolution, provides strong evidence for an LSB, which forms in the absence of forced transition during the initial phase of the dynamic stall process. The reattachment point for the LSB was estimated from the literature [65] as the chordwise location that is associated with a distinct change in the severity of the adverse pressure gradient. In the current dynamic stall process, the LSB reattachment point is observed to move upstream causing the LSB to contract with increasing angles of attack. The movement of the LSB reattachment point is inferred from Fig. 3.3 b) and 3.3 c), and also traced by a dashed curve in Fig. 3.2 b). The behavior of the LSB, from the current experiments, is also consistent with LES-based investigations in the literature. [18, 19, 23, 24] The LSB eventually attains a critical minimum size that remains independent of small increases in the airfoil angle of attack, as seen in Fig. 3.2 b).

In addition to a spatially-evolving LSB, the initial phase of the dynamic stall process is also characterized by a rapid growth in the peak suction with increasing angles of attack. The airfoil suction attains a global peak $C_{p,min} = -7.63$ at $\alpha = 17.97^{\circ}$, as seen in Fig. 3.2 and Fig. 3.3 e). Besides attaining peak suction, the surface pressure at $\alpha = 17.97^{\circ}$ is also associated with reduced pressure recovery near the airfoil trailing edge, as shown in Fig. 3.3 e). The incomplete recovery of pressure is indicative of trailing-edge flow separation. Further increase in the airfoil angle of attack is accompanied by a rapid collapse in the suction

peak. This event has been associated in the literature with the breakdown or bursting of the LSB, which is characterized by flow separation near the airfoil leading edge. This leading-edge BL separation is distinct from the separation at the airfoil trailing edge, which was identified from Fig. 3.3 e). The collapse in peak suction occurs much earlier for the airfoil model in the tripped configuration, as seen again in Fig. 3.3 e). Consequently, the tripped airfoil stalls earlier than the airfoil in the clean configuration, as had been observed previously in Fig. 3.1. The growth of perturbations within the unstable separated shear layer, after the collapse in leading-edge suction, results in the roll up of the interface into coherent vortical structures, creating a distinct imprint on the pressure distribution, as indicated in Fig. 3.3 g). The emergence and rapid growth of the DSV result in a large low-pressure region, which at $\alpha = 22.53°$, extends to almost 60% of the chord, as seen in Fig. 3.3 h). The DSV-induced suction produces a distinct increase in the lift-curve slope, as had been observed previously in Fig. 3.1 a). Whilst growing spatially, the DSV core also convects downstream with increasing angles of attack, as highlighted in Fig. 3.2. This motion of the vortex core can also be inferred from the downstream displacement of the minimum pressure peak between Fig. 3.3 h) and Fig. 3.3 i). The diminishing suction peak, between Fig. 3.3 h) and Fig. 3.3 i), indicates that in addition to moving downstream, the DSV core also convects away from the surface of the airfoil. Finally, the surface pressure data beyond $x_c/c = 0.153$ are associated with a transient, but distinct increase in C_p prior to the appearance of a DSV-induced suction imprint, as outlined in Fig. 3.2 a). This transient increase in pressure has also been observed in simulations, [18, 19] and is caused by the vortex-induced movement of the fluid towards the airfoil surface in the immediate downstream vicinity of the DSV.

3.1.3 Pressure Spectra

An estimate of the unsteadiness in the surface pressure field was obtained by calculating the root mean square of the time-dependent pressure, using Eq. 2.93 from Chapter 2. It is important to emphasize once more that $C_{p,rms}$, from Eq. 2.93, is defined with respect to the low-pass filtered C_p, in order to highlight the unsteadiness in the pressure field from localized, transient sources, as opposed to the global pressure evolution that stems primarily from the pitching motion of the airfoil. The time-evolution of $C_{p,rms}$ for the clean airfoil at $Re_c = 0.5 \times 10^6$ is presented in Fig. 3.4 a). Select chordwise $C_{p,rms}$ distributions for a fixed set of angles of attack are presented in Fig. 3.5. Similar to the presentation of the acquired surface pressure in Section 3.1.2 of this document, the tripped airfoil $C_{p,rms}$ at $\alpha = 11.11°$ and $\alpha = 14.15°$ have also been incorporated in Fig. 3.5 b) and Fig. 3.5 c), for the purposes of comparison. Furthermore, a series of markers have been included in Fig. 3.4 a) and Fig. 3.5 to denote the position of the pressure transducers on the airfoil surface.

Starting from an initial laminar state, the BL during the airfoil pitch motion begins to transition near the trailing-edge region of the airfoil. This transition process is associated with a localized peak in $C_{p,rms}$, as observed in Fig. 3.5 a), for an example $C_{p,rms}$ acquisition at $\alpha = 4.08°$. The region at which the BL transitions from an initial laminar to a final turbulent state, moves upstream with increasing angles of attack. This movement of the transition zone is highlighted in Fig. 3.4 a), and is consistent with simulations from the literature. [18, 19] The approximate motion of the peak $C_{p,rms}$ is also presented in Fig. 3.4 b). At $\alpha = 11.11°$, a distinct $C_{p,rms}$ peak appears at $x_c/c = 0.056$, as highlighted in Fig. 3.5 b). This $C_{p,rms}$ peak reflects the increased unsteadiness in the BL resulting from the turbulent reattachment of the LSB, which had been identified previously in Section 3.1.2. As the LSB contracts, the $C_{p,rms}$ peak moves upstream following the reattachment point of the separated shear layer, with increasing angles of attack. Thus, the maximum $C_{p,rms}$ at $\alpha = 14.15°$ is positioned upstream of the corresponding maximum at $\alpha = 11.11°$, as observed from Fig. 3.5 b) and 3.5 c). For the tripped airfoil configuration, however, the chordwise position of the $C_{p,rms}$ peak remains independent of the angle of attack. This fixed transition region is centered at $x_c/c \approx 0.033$, as shown in Fig. 3.5 b) and Fig. 3.5 c). From the surface pressure acquisition for the clean airfoil, the size of the LSB beyond $\alpha = 13°$, was found to attain a critical minimum and remain independent of small increments in the angle of attack. Consequently, a region of elevated $C_{p,rms}$ persists near the airfoil leading edge, as outlined in Fig. 3.4 a). The collapse in leading-edge suction and the emergence of vortical structures are associated with a significant increase in $C_{p,rms}$, as observed in Fig. 3.4 a) and Fig. 3.5 d). This increase in $C_{p,rms}$ was also seen previously in the experiments of Lorber and Carta, [9] during an equivalent phase of the dynamic stall process. The global maximum in the $C_{p,rms}$ field occurs between $\alpha \approx 18.5°$ and $\alpha \approx 19°$. After emergence of the DSV, the $C_{p,rms}$ peaks diminish with increasing angles of attack, as inferred from Fig. 3.4 a) and 3.5 f). Thus, the unsteadiness in the surface pressure decreases gradually as the DSV core convects away from the surface of the airfoil.

The frequencies associated with the fluctuations in the pressure field were evaluated from the measurements of the surface pressure that were acquired at a high-sampling rate, as specified previously in Chapter 2. These high-resolution measurements were performed across the leading-edge region of the airfoil. The estimation of the frequencies associated with the pressure fluctuations was accomplished using a continuous wavelet transform technique, as described previously in Chapter 2. The phase-averaged, time-dependent energy spectra of the pressure acquisition at $x_c/c = 0.067, 0.094, 0.117, 0.153$ on the airfoil upper surface are presented in Fig. 3.6. The corresponding surface pressure evolutions are also presented in Fig. 3.6, for reference. It should be noted that the pressure spectra of Fig. 3.6 correspond to the airfoil model in the clean configuration. The unsteady pressure and the associated time-varying spectra for the tripped airfoil

at equivalent chordwise positions are presented in Fig. 3.7, for comparison. A threshold filter has been employed in each of the spectra presented in this section in order mask the low-amplitude regions, with $E < -20$ dB, that stem primarily from the background noise. A set of high-energy transients can be observed in the pressure spectra during the initial phase of the dynamic stall process, as identified by number 1 in Fig. 3.6. For a given chordwise location, this feature of the energy spectra appears when the LSB reattachment point passes over the corresponding location on the airfoil surface. The LSB reattachment also produces a distinct feature in the acquired pressure measurements, as indicated in Fig. 3.6 a). Due to the spatial contraction of the LSB, which brings the separated shear layer close to the surface of the airfoil, the LSB-induced unsteadiness in Fig. 3.6 is observed to be more prominent in the pressure data at $x_c/c = 0.067$. In the absence of the LSB for the tripped airfoil, the reattachment-induced unsteadiness does not appear in the pressure spectra for this configuration, as seen in Fig. 3.7. Beyond the initial period of the dynamic stall process, an extensive high-energy phase dominates the pressure spectra for both the clean and the tripped airfoils, as observed in Fig. 3.6 and Fig. 3.7. This prolonged period of high energy fluctuations, labeled as region 2, initiates in the lead up to the collapse of leading-edge suction and persists beyond the emergence of the DSV.

In order to identify the dominant frequencies associated with the LSB, the amplified energy of region 1, which describes the LSB reattachment process, is isolated from the full pressure spectra of Fig. 3.6. As an example, the energy spectrum at $x_c/c = 0.153$ is presented in Fig. 3.8 a), for a fixed angle of attack of $\alpha = 8.50°$. This angle of attack was selected, since it lies at the center of region 1 in Fig. 3.6 d). Similarly, the energy spectra corresponding to the LSB reattachment at $x_c/c = 0.067, 0.094, 0.117$ are also included in Fig. 3.8 a), for comparison. It should be noted that the energy spectra of Fig. 3.8 a) are displaced progressively by a value of 10 dB with increasing angles of attack. These spectra are characterized by a broad range of distinctly amplified frequencies centered around well-defined peaks. The frequencies associated with the well-defined peaks correspond to the most amplified mode of fluctuations in pressure during the reattachment of the LSB. It is interesting to note that the center frequency increases as the LSB reattachment point drifts upstream with increasing angles of attack. Across an angle-of-attack range between $\alpha = 8.50°$ and $\alpha = 10.50°$, the dominant LSB modes span a wide range of frequencies, which corresponds to a set of chord-based Strouhal numbers between $St = 50$ and $St = 105$, as shown in Fig. 3.8 b). This Strouhal range is consistent with those reported from the simulations of Visbal and Garmann. [19] In contrast with a fixed length scale, an alternative Strouhal definition based on a time-dependent length scale calculated from the chordwise projection of the LSB in the vertical plane, as described previously in Chapter 2, was also employed to characterize the center frequencies at the reattachment of the LSB. This

variable-length Strouhal scaling was found to reduce the disparate set of frequencies to an approximately constant value of $St_{LSB} \approx 1.2$, as shown in Fig. 3.8 b). Besides the analysis of region 1 of the pressure spectra, the second region of amplified pressure perturbations is also observed to contain a distinct feature of interest. The appearance of the vortex-induced suction peak is observed, in Fig. 3.6, to be accompanied by a rapid collapse in the spectral energy at the higher frequencies, as indicated by dashed arrows in Fig. 3.6. This behavior is also observed for the model in the tripped configuration, as indicated in Fig. 3.7. Thus, the pressure fluctuations are gradually dominated by the low-frequency modes during the DSV inception phase of the dynamic stall process.

3.2 TR-PIV Results

The detailed flow development for the dynamic stall process at $Re_c = 0.5 \times 10^6$ and the associated physical implications are described in this section.

3.2.1 Flow Evolution

The evolution of the off-body flowfield is studied using contours of the phase-averaged velocity, phase-averaged z-vorticity, and instantaneous Q-criterion at several representative angles of attack. The phase-averaged velocity and vorticity are presented in Fig. 3.9 and Fig. 3.10, respectively, whilst the instantaneous Q-criterion contours are presented later in Fig. 3.11. All of the results presented in this section correspond to the airfoil model in the clean configuration. Moreover, for the purposes of visualization, the value of ω_{ref} and Q_{ref} in Fig. 3.10 and Fig. 3.11 have been selected to saturate the highest 0.5% of the ω_z and Q values at each angle of attack. For reference, a series of velocity vectors have also been included in Fig. 3.9 at regular spatial intervals of $\Delta(x/c) \approx 0.025$ and $\Delta(y/c) \approx 0.017$.

The description of the flow development begins from an initial phase that corresponds to the state of the flow prior to the rapid collapse of leading-edge suction, which was observed from the pressure acquisition in Fig. 3.3 f). During this initial stage of the dynamic stall process, which corresponds to $\alpha = 17.97°$ and $\alpha = 19.20°$, the flow is observed to be largely irrotational except in the immediate vicinity of the surface, as seen in Fig. 3.10 and Fig. 3.11. This vortex-dominated region thickens gradually as the flow convects towards the airfoil trailing edge. The observed thickening results presumably from the diffusion of vorticity in the wall-normal direction. From the instantaneous Q contours of Fig. 3.11 a) and Fig. 3.11 b), the near-wall flow is characterized by a stochastic distribution of small-scale vortical structures, with large positive values for Q, and irrotational, strain-dominated regions with $Q < 0$. It should be mentioned here that the

irregular nature of the instantaneous flow is not an artifact of the image processing methodology, but an actual representation of the real behavior of the flow at a transitional Reynolds number. The statistical nature of the instantaneous flow is, however, significantly diminished during the phase-averaging process. The chord-normal spread of the vortices is strongly indicative of BL separation in the aft region of the airfoil, resulting in a reduced pressure recovery at the airfoil trailing edge, as identified previously from Fig. 3.3 e). It should be clarified here that the associated region of reversed flow is too narrow to be observed directly from the velocity field at $\alpha = 19.20°$. However, several LES-based investigations in the literature [18, 19, 23, 24] have captured the separation of the BL during the initial phase of the dynamic stall process for similar Reynolds numbers and dimensionless pitch rates. The associated separation point has been shown, in these studies, to originate near the airfoil trailing edge and to propagate upstream with increasing angles of attack. It should also be noted that the angles of attack associated with Fig. 3.11 a) and Fig. 3.11 b) are significantly larger than the static stall angle of the airfoil at $Re_c = 0.5 \times 10^6$. Thus, consistent with the classical understanding, the flow around the airfoil model during the linear pitch-ramp maneuver of the present investigations is associated with a significant delay in large-scale BL separation and stall.

With further increase in the angle of attack from $\alpha = 19.87°$ to $\alpha = 20.63°$, a rapid accumulation of vorticity occurs near the leading edge of the airfoil, as observed in Fig. 3.10 c), Fig. 3.10 d), and Fig. 3.10 e). This growth in vorticity results from the ejection of vortical structures as indicated in Fig. 3.11 c). A leading-edge reversed flow region can also be seen quite distinctly from the velocity acquisition during this phase of the dynamic stall process. At $\alpha = 20.63°$, for example, this reversed flow region is highlighted by a red curve, as shown in Fig. 3.9 e). The leading-edge coherent structures (LECS) of Fig. 3.11 c) are conjectured to result from an instability of the separated shear layer. The physical mechanism associated with the LECS ejection is analyzed in detail in Section 3.4. The displacement of the shear layer after BL separation reduces the overall curvature of the flow around the airfoil leading edge, causing a rapid decline in the suction, as had been observed from the pressure evolution in Fig. 3.2. Further downstream, the strength of the trailing-edge vortices is observed, from Fig. 3.10 c)–g), to diminish rapidly after the ejection of LECS, presumably due to viscous diffusion. The continuous production of LECS and the associated mutual interactions between the small-scale vortices result in the formation of a significantly larger coherent structure, known as the DSV. The DSV can be observed quite distinctly at $\alpha = 22.53°$, as indicated in Fig. 3.9 h), Fig. 3.10 h), and Fig. 3.11 h). From the instantaneous Q field of Fig. 3.11 h), the DSV is observed to consist of a multitude of vortical structures, which are separated by regions of irrotational straining, as opposed to a single, large, and distinct vortex. This fine-grained nature of the DSV, at a transitional Reynolds number, is consistent with

the experimental observations of Pruski and Bowersox. [13] Upon emergence, the DSV creates a large suction imprint on the airfoil surface, as seen before from the acquired pressure data of Fig. 3.3 h). Downstream of the DSV core, the fluid elements are associated with a vortex-induced velocity component towards the airfoil surface, as seen in Fig. 3.9 h). This feature of the flow was conjectured previously by observing a transient increase in the surface pressure, prior to the DSV-induced suction in Fig. 3.2 a). After formation, the DSV grows rapidly through a process of the entrainment of the surrounding fluid. The rapid growth in the DSV is accompanied by a distinct increase in the lift-curve slope, which was mentioned previously in reference to Fig. 3.1 a). In addition to the spatial growth, the DSV also convects away from the airfoil, as inferred from Fig. 3.9 h) and Fig. 3.9 i). The overall behavior of the DSV from the TR-PIV measurements is consistent with the pressure acquisition of Fig. 3.2 and Fig. 3.3.

3.2.2 Flow Spectra

The time-dependent amplitudes and frequencies of the dominant velocity perturbations for the clean airfoil dynamic stall process at $Re_c = 0.5 \times 10^6$ is described in this section. The velocity spectra were extracted using a combination of EMD and Hilbert transform, as described in Chapter 2. The results presented in this section were also phase averaged over multiple experimental realizations, using an energy-weighted averaging procedure, which is also described in Chapter 2.

The velocity spectra for a set of representative angles of attack are shown in Fig. 3.12. The angles of attack correspond to the flow states starting from the ejection of the LECS and leading up to the emergence of the DSV. The fluctuation energy in Fig. 3.12 can be gauged from the transparency level of the frequency contours. The plot regions with the highest 5% of the spectral energy are rendered opaquely, whilst the remaining areas are filled with a transparency level that is set linearly proportional to the corresponding energy. The frequency estimates in Fig. 3.12 are presented in terms of the chord-based Strouhal number, as defined in Eq. 2.24. The separated shear region is observed, from Fig. 3.12, to be associated with elevated fluctuation amplitude as compared to the rest of the flowfield. As further evidence of this increased unsteadiness, the highest 15% of the spectral energy was extracted at a given chordwise position in the flowfield. The boundary of this high-energy region, outlined by the dashed curves in Fig. 3.12, is observed to straddle the shear layer across the entire airfoil chord. The elevated unsteadiness therefore, appears to originate from a shear layer instability, which results in the local roll-up of the shear interface into a substantial number of small-scale LECS, as described earlier in the discussion pertaining to Fig. 3.11. The most amplified frequency at each chordwise position was also isolated from the full frequency field at several angles of attack in order to produce a space-time representation of the velocity spectra. The time-

dependent, chordwise frequency distribution for the isolated velocity spectra is presented in Fig. 3.13 a). The corresponding spectral energy is presented separately in Fig. 3.13 b). Similar to Fig. 3.6, a threshold filter is also employed in the velocity spectra of Fig. 3.13 in order to mask the regions where the energy of fluctuations is lower than $E < 0$ dB. From Fig. 3.13, the most-dominant velocity perturbation modes are observed to have insignificant energy during the initial phase of the dynamic stall process, i.e., below $\alpha \approx 18°$. The small perturbation amplitude is however, unsurprising, since the BL remains largely attached to the airfoil surface for angles of attack below $\alpha \approx 18°$. In fact, the airfoil was observed, from Fig. 3.3, to attain peak suction around $\alpha = 17.97°$. The separation of the flow at the airfoil leading edge and the initial ejection of the LECS, which occurs around $\alpha = 19.80°$, is indicated by a dashed line in Fig. 3.13. The perturbation amplitude reaches a maximum during the ejection of LECS, as indicated by the dashed outlines in Fig. 3.13 a) and Fig. 3.13 b). These high energy outlines define a region where the perturbation energy is more than two standard deviations above the global mean energy level. The elevated state of velocity fluctuations is, however, transient in nature, spanning an angle of attack range of $\Delta\alpha \approx 1.20°$. The average frequency of the perturbations during the high power transient is determined to be equal to $St = 6.23 \pm 0.09$. The increased unsteadiness is consistent with the simulations of Visbal, [18] wherein the highest fluctuations in the flow were observed during an equivalent phase of the dynamic stall process.

Following the high-power transient, the dominant fluctuations in the dynamic stall flowfield exhibit a complex, non-monotonic decline in frequency in the region next to the airfoil leading edge, as observed from Fig. 3.14 a). The Strouhal number associated with the time-varying frequency at $x/c = -0.15$, for example, decreases from $St \approx 6$ at $\alpha = 20.19°$ to $St \approx 4$ by $\alpha = 22.00°$, as shown in Fig. 3.14 b). The flow structures near the airfoil leading edge are therefore associated with increasing spatial and temporal scales as the dynamic stall process progresses towards the emergence of the DSV. Near the airfoil quarter-chord, however, the perturbation frequency across the same angle of attack range is observed, from Fig. 3.14 a) and 3.14 c), to follow a trend that is opposite of the spectral behavior near the airfoil leading edge. The increase in the frequency downstream of the leading-edge region is conjectured to result from a breakdown of the LECS into finer structures with comparatively smaller spatio-temporal scales.

3.3 Reynolds Number Effects

The effect of Reynolds number on the dynamic stall process is described in this section by comparing the pressure and velocity measurements that were acquired at different transitional Reynolds numbers, but for a fixed set of motion parameters, i.e., a fixed angle of attack range between $\alpha = -6°$ and $\alpha = 31°$ and

non-dimensional pitch rate, $\Omega^+ = 0.05$. The pressure development and the associated spectra are compared for two distinct Reynolds numbers, $Re_c = 0.5 \times 10^6$ and $Re_c = 1.0 \times 10^6$. The unsteady flowfield and flow spectra are also presented for $Re_c = 0.2 \times 10^6$ in addition to $Re_c = 0.5 \times 10^6$ and $Re_c = 1.0 \times 10^6$. The surface pressures could not be acquired during the pitch ramp maneuver at $Re_c = 0.2 \times 10^6$ due to the significantly lower dynamic pressures at this Reynolds number, which produced dimensional pressure values far closer to the uncertainty limits of the associated acquisition system, as compared to the higher Re_c cases.

3.3.1 Airfoil Performance

A comparison of the unsteady lift and quarter-chord pitching moment coefficients for the NACA 0012 airfoil model at $Re_c = 0.5 \times 10^6$ and $Re_c = 1.0 \times 10^6$ is presented in Fig. 3.15. From Fig. 3.15, the airfoil attains a maximum lift of $C_{l,max} = 2.37 \pm 0.02$ and $C_{l,max} = 2.57 \pm 0.01$ at $Re_c = 0.5 \times 10^6$ and $Re_c = 1.0 \times 10^6$, respectively. The lift stall for $Re_c = 0.5 \times 10^6$ and $Re_c = 1.0 \times 10^6$ occurs at $\alpha_{stall} = 26.14°$ and $\alpha_{stall} = 25.03°$. Thus, contrary to intuition, the airfoil model of the current experiments stalls earlier at the higher Reynolds number. This observation indicates that the DSV, which is primarily responsible for lift generation near stall, convects away at a much faster rate at the higher Reynolds number. In contrast with the relative differences near stall, the lift polar during the initial phase of the dynamic stall process is observed to be largely similar for both the Reynolds numbers. At $\alpha \approx 18°$, however, the lift polar at $Re_c = 0.5 \times 10^6$ starts to diverge from the high Reynolds number counterpart. This lift divergence is produced by the vortex-induced suction after the breakdown of the LSB, which is a feature that had been identified previously from the pressure evolution at $Re_c = 0.5 \times 10^6$, as shown in Fig. 3.3. It is therefore conjectured that the collapse of suction at the airfoil leading edge at $Re_c = 1.0 \times 10^6$ is delayed, in comparison with $Re_c = 0.5 \times 10^6$. Besides the initial lift divergence, a second phase of rapid lift growth is observed in the C_l polar corresponding to $Re_c = 0.5 \times 10^6$. This feature spans a range of angles of attack, starting from $\alpha = 23.58°$ and leading up to $\alpha_{stall} = 26.14°$, and had been described previously in Section 3.1.1. A similar phase of the dynamic stall process is also observed at the higher Reynolds number between $\alpha = 23.09°$ and $\alpha_{stall} = 25.03°$, as seen in Fig. 3.15 a).

From Fig. 3.15 b), the quarter-chord pitching moment coefficient is observed to attain a peak value of $C_{m,min} = -0.50 \pm 0.01$ at $Re_c = 0.5 \times 10^6$ and $C_{m,min} = -0.37 \pm 0.01$ at $Re_c = 1.0 \times 10^6$. The lower peak magnitude of the pitching moment at $Re_c = 1.0 \times 10^6$ is also a result of the rapid convection of the DSV at the higher Reynolds number. The moment stall of the airfoil model is observed at $\alpha = 26.94°$ and $\alpha = 26.09°$ for $Re_c = 0.5 \times 10^6$ and $Re_c = 1.0 \times 10^6$, respectively. Prior to the peak C_m at $Re_c = 0.5 \times 10^6$, a local maximum is observed in Fig. 3.15 b) at $\alpha = 21.63°$. This local C_m peak is produced during the initial growth

of vorticity near the leading-edge region of the airfoil. A similar feature is also observed at $\alpha = 25.07°$, in the moment polar corresponding to $Re_c = 1.0 \times 10^6$. Prior to the transient peak at $\alpha = 25.07°$ however, a strong pitch-down moment appears in the C_m polar corresponding to the higher Reynolds number, at $\alpha = 24.27°$. This additional feature is indicative of a possible secondary coherent structure that forms aft of the quarter chord of the airfoil, creating a transient nose-down moment prior to the vorticity growth at the airfoil leading edge. The hypothesis in regards to a secondary vortex at $Re_c = 1.0 \times 10^6$ is examined in greater detail in Section 3.3.3.

3.3.2 Pressure Evolution and Spectra

The time-dependent surface pressure at $Re_c = 1.0 \times 10^6$ is presented in Fig. 3.16. The chordwise pressure distribution at select instances of the dynamic stall process at $Re_c = 1.0 \times 10^6$ is shown in Fig. 3.17. The pressure acquisition at $Re_c = 0.5 \times 10^6$ is also presented in Fig. 3.16, for reference. Similar to the pressure evolution at the lower Reynolds number, the initial phase of the dynamic stall process is associated with a rapid growth in suction at the airfoil leading edge. A sample pressure distribution during this initial phase, at $\alpha = 7.09°$, is associated with a complete pressure recovery at the airfoil trailing edge, as seen in Fig. 3.17 a). An increase in the angle of attack is accompanied by the appearance of an LSB-induced pressure plateau near the leading-edge region, as identified in Fig. 3.17 b). An LSB-induced pressure plateau had also been observed previously in the dynamic stall process at $Re_c = 0.5 \times 10^6$. The growth in the suction continues until an angle of attack of $\alpha = 23.67°$, during which the airfoil attains a peak minimum $C_p = -14.98 \pm 0.03$, as observed in Fig. 3.16 a) and Fig. 3.17 d). The suction peak at $Re_c = 1.0 \times 10^6$ is therefore, significantly greater than the peak $C_p = -7.63 \pm 0.07$, which was attained by the airfoil at the lower Reynolds number.

After attaining the pressure minimum, the leading-edge suction at $Re_c = 1.0 \times 10^6$ collapses quickly with increasing angles of attack. For the dynamic stall case at $Re_c = 0.5 \times 10^6$, the collapse of suction at the airfoil leading edge led eventually to the appearance of a distinct DSV-induced suction imprint, as shown in Fig. 3.3 h). At the higher Reynolds number, however, two distinct peaks develop in the C_p distribution, as identified in Fig. 3.17 f). It is conjectured that these peaks result from the formation of two distinct vortical structures, V_1 and V_2, as opposed to a single vortex that was observed at the lower Reynolds number. The appearance of an additional coherent structure was also inferred previously from the C_m polar in Fig. 3.15 b). With further increase in the angle of attack, the two suction peaks are observed to gradually merge into a single peak, as seen in Fig. 3.17 f), Fig. 3.17 g), and Fig. 3.17 h). Thus, the initially distinct vortical structures appear to combine into a single, coherent DSV. This unique behavior of the dynamic stall process at $Re_c = 1.0 \times 10^6$ is examined in greater detail from the off-body velocity acquisition presented in

Section 3.3.3. After formation, the DSV convects downstream with increasing angles of attack, producing a distinct suction signature that is outlined in Fig. 3.16 a). It is important to remind that the surface pressure at $Re_c = 0.5 \times 10^6$ was associated with a transient pressure recovery phase, prior to the appearance of the DSV-induced suction, as indicated in Fig. 3.2 a). This feature is however, absent from the pressure acquisition at the higher Reynolds number, which indicates that the DSV convection speed at $Re_c = 1.0 \times 10^6$ is significantly larger in comparison with $Re_c = 0.5 \times 10^6$. Thus, the effects of flow entrainment on the airfoil surface are largely diminished at $Re_c = 1.0 \times 10^6$ in comparison with the lower Reynolds number.

The energy spectra for the high time-resolution pressure measurements near the airfoil leading edge at $x_c/c = 0.033, 0.044, 0.056$ are presented in Fig. 3.18 a). The spectral contours at $x_c/c = 0.067, 0.094, 0.117$ from the dynamic stall process at the lower Reynolds number, presented originally in Fig. 3.6, are also reproduced in Fig. 3.18 b), for reference. As with the previous energy spectra from Fig. 3.6, a threshold filter has been employed in the energy iso-contours of Fig. 3.18 a) in order to mask the non-energetic contributions that stem primarily from the background noise, with $E < -30$ dB. From Fig. 3.18 a), the energy spectra for the clean airfoil at $Re_c = 1.0 \times 10^6$ are associated with a transient and later, a prolonged region of elevated spectral amplitude, following a general trend that is similar to the observed behavior at $Re_c = 0.5 \times 10^6$. As described in Section 3.1.3, the high-energy transient of region 1, in Fig. 3.18 a), corresponds to the reattachment of the LSB. The flow behavior near the reattachment point at $Re_c = 1.0 \times 10^6$ is also associated with a distinct disturbance in the C_p acquisition, as highlighted in Fig. 3.18 a)-i). In contrast with $Re_c = 0.5 \times 10^6$ however, the amplified energy of region 1, at the higher Reynolds number, is not associated with well-defined center frequencies. The absence of a dominant energy mode is likely a result of the hardware-limited acquisition rate, which was inadequate in capturing the temporal scales associated with the LSB-induced pressure fluctuations at the higher Reynolds number. The second region of amplified fluctuations in the pressure spectra was associated previously, in Section 3.1.3, with the collapse of leading edge suction and the emergence of the DSV. A transient, vortex-induced spike is observed in the surface pressure acquisition within region 2, as indicated in Fig. 3.18 a)-iii). This transient pressure feature has also been observed in the simulations of Benton and Visbal. [21, 22] Finally, the overall fluctuation energy at moderate and high frequencies is observed, from Fig. 3.18 a), to diminish rapidly for angles of attack beyond the suction peak. This behavior of the energy spectra at the higher angles of attack for $Re_c = 1.0 \times 10^6$ is consistent with the spectra at the lower Reynolds number, as observed in Fig. 3.18 b).

3.3.3 Flow Evolution

In Section 3.2.1, the dynamic stall process at $Re_c = 0.5 \times 10^6$ was described in detail, starting from an initial, largely irrotational state and leading up to the emergence of the DSV. For the purposes of comparison, the instantaneous Q-criteria at select angles of attack are presented in Fig. 3.19 a) and Fig. 3.19 c) for the dynamic stall processes at $Re_c = 0.2 \times 10^6$ and $Re_c = 1.0 \times 10^6$. The instantaneous Q contours for the dynamic stall process at $Re_c = 0.5 \times 10^6$, presented earlier in Fig. 3.11, have also been reproduced in Fig. 3.19 b), for the sake of completeness. It should be mentioned that the angles of attack in Fig. 3.19 have been judiciously selected such that each row provides a comparison of the flow across different Reynolds numbers for an approximately equivalent phase of the dynamic stall process. Thus, the differences in the flow development characteristics discussed hereafter are not an artifact of the selected angles of attack, but result solely from a variation in the Reynolds number.

As described in Section 3.2.1, the initial separation of the boundary layer at the airfoil trailing edge is inferred from the coherent vortical structures that appear near the vicinity of the airfoil surface, as observed in Fig. 3.19 i) and ii). The large chord-normal spread of the vortices at $Re_c = 1.0 \times 10^6$ indicates that the trailing-edge separation, prior to the ejection of LECS, is more prominent at the higher Reynolds number. A comparison of the phase-averaged velocity contours across the three Reynolds numbers is presented in Fig. 3.20 for identical angles of attack as those of the Q-contours in Fig. 3.19. Thus, the velocity fields of Fig. 3.20 ii) correspond to an equivalent phase of the dynamic stall process prior to the emergence of the LECS. For $Re_c = 1.0 \times 10^6$, a distinct region of reversed flow can be observed near the airfoil trailing edge, as indicated in Fig. 3.20 c)-ii). In contrast, the reversed flow region at $Re_c = 0.2 \times 10^6$ and $Re_c = 0.5 \times 10^6$ was presumably thinner than what could be resolved from the current TR-PIV measurements. These observations provide a more direct evidence for the prominent state of trailing-edge separation at $Re_c = 1.0 \times 10^6$ in comparison to the lower Reynolds numbers. With an increase in the angle of attack, the flow eventually separates at the airfoil leading edge which results in the ejection of LECS, as seen in Fig. 3.19 iii). These LECS appear at $\alpha = 17.19°$, $\alpha = 19.87°$, and $\alpha = 24.07°$, for $Re_c = 0.2 \times 10^6$, $Re_c = 0.5 \times 10^6$, and $Re_c = 1.0 \times 10^6$, which reflects the progressive delay in the leading-edge separation at the higher Reynolds numbers. This delay in BL separation enables the trailing-edge separation point to propagate to a significantly farther upstream location, which had been inferred from Fig. 3.19 c)-ii). The delay in the LECS emergence at $Re_c = 1.0 \times 10^6$ was also indicated previously from the performance and pressure results of Fig. 3.15 and Fig. 3.17. The progression of the dynamic stall process beyond the emergence of the LECS and leading up to the formation of the DSV is similar for $Re_c = 0.2 \times 10^6$ and $Re_c = 0.5 \times 10^6$, as shown in Fig. 3.19 a)-[iv)-viii)] and Fig. 3.19 b)-[iv)-viii)]. However, this progression from the LECS to the DSV occurs more rapidly for $Re_c = 0.5 \times 10^6$,

with $\Delta\alpha = 2.22°$ in comparison with $Re_c = 0.2 \times 10^6$, wherein the equivalent process was observed to span an angle of attack range of $\Delta\alpha = 3.09°$.

For $Re_c = 1.0 \times 10^6$, the dynamic stall process, after the leading-edge flow separation, diverges rapidly in its behavior in comparison with the lower Reynolds numbers. While the lower Reynolds number cases were associated with the coalescence of the LECS into a single vortex, the leading-edge structures at $Re_c = 1.0 \times 10^6$ are observed, from Fig. 3.19 c)–v), to coalesce into two distinct regions, V_1 and V_2, centered at $x/c \approx -0.01$ and $x/c \approx 0.21$, respectively. Although the formation of the primary vortex, V_1, is characteristically similar to that of a leading-edge vortex, the emergence of the secondary vortical structure, V_2, reflects a significant departure from the classical dynamic stall process, which is generally characterized by the emergence of a single, distinct, DSV. It should be noted that the emergence of the two distinct vortices at the higher Reynolds number was conjectured previously from the pressure acquisition, as described in Sections 3.3.1 and 3.3.2. Moreover, the location of the secondary vortex aft of the airfoil quarter-chord, is expected to produce a strong pitch down moment, as had been suggested from the characteristics of the C_m polar, presented in Fig. 3.15 b). With an increase in the angle of attack from $\alpha = 25.04°$ to $\alpha = 25.52°$, the secondary vortex is gradually swept upstream where it merges with the primary vortical structure, as seen in Fig. 3.19 c)-[v)-viii)]. The two initially-distinct vortices therefore, combine to produce a single DSV, which is identified in Fig. 3.19 c)–ix). The process of the emergence of the DSV, from the merging of a co-rotating vortex pair displays great similarities with the simulations of Benton and Visbal. [21,22] A similar process was also seen in the experiments of Mulleners and Raffel. [15] It should be highlighted here that the co-rotating vortex merging process is a repeating feature of the dynamic stall process at $Re_c = 1.0 \times 10^6$, as it can also be observed from the phase-averaged velocity contours that are presented in Fig. 3.20 c)-[v)-viii)]. Despite the complex nature of DSV emergence at the higher Reynolds number, the progression of the flow from the initial ejection of LECS to the emergence of the DSV occurs across an angle of attack range of $\Delta\alpha = 1.64°$, which is significantly smaller than the corresponding angular duration for $Re_c = 0.2 \times 10^6$ and $Re_c = 0.5 \times 10^6$.

3.3.4 Flow Spectra

The time-dependent spectra were analyzed in Section 3.2.2 by extracting the most amplified frequency at each chordwise location across several angles of attack. The space-time representation of the isolated velocity spectra was presented in Fig. 3.13. Following a similar process, the most dominant frequency modes were also extracted for further analysis from the phase-averaged velocity spectra at $Re_c = 0.2 \times 10^6$ and $Re_c = 1.0 \times 10^6$. These time-dependent, chordwise frequency distributions are presented in Fig. 3.21

a) and Fig. 3.21 c). A low-energy threshold filter, set at $E < 0$ dB, was also employed in Fig. 3.21. The initial ejection of the LECS and the emergence of the DSV have also been highlighted in these figures. The energy spectra for $Re_c = 0.5 \times 10^6$, from Fig. 3.13 a), has been reproduced in Fig. 3.21 b), to aid with the comparison.

Similar to the spectra at $Re_c = 0.5 \times 10^6$, the appearance of the coherent structures near the airfoil leading edge at $Re_c = 0.2 \times 10^6$ and $Re_c = 1.0 \times 10^6$ is also associated with a transient phase of high-amplitude velocity fluctuations, as outlined in Fig. 3.21 a) and Fig. 3.21 c). As with Fig. 3.21 b), the LECS-induced, high-amplitude outlines in Fig. 3.21 a) and Fig. 3.21 c) define regions where the perturbation energy is more than two standard deviations greater than the corresponding global mean energy levels. The high-amplitude transient appears at $\alpha = 16.73°$ for $Re_c = 0.2 \times 10^6$, and much later at $\alpha = 23.70°$ for $Re_c = 1.0 \times 10^6$, reflecting once again the significant delay in leading-edge separation at the higher Reynolds number. The high-energy outlines in Fig. 3.21 a) and Fig. 3.21 c) are associated with average frequencies of $St = 13.98 \pm 0.09$ and $St = 3.42 \pm 0.02$, for $Re_c = 0.2 \times 10^6$ and $Re_c = 1.0 \times 10^6$, respectively. As a reminder, the Strouhal number, during an equivalent phase of the dynamic stall process at $Re_c = 0.5 \times 10^6$ was estimated at $St = 6.23 \pm 0.09$. It is important to further note that these Strouhal numbers were calculated using the airfoil chord length and the freestream velocity, at a given Reynolds number, as the characteristic length and velocity scales. The large variation in the chord-based St with Reynolds number, therefore, indicates that the chord length and the freestream velocities are not reflective of the characteristic length and velocity scales associated with the LECS. A displacement-thickness based Strouhal scaling of the leading-edge frequencies is discussed later in Section 3.4.

As with $Re_c = 0.5 \times 10^6$, the frequencies of the velocity perturbations at $Re_c = 0.2 \times 10^6$ and $Re_c = 1.0 \times 10^6$ attain a local maximum during the high-energy transient at the airfoil leading edge. With an increase in the angle of attack, the leading edge frequencies decrease rapidly, as observed in Fig. 3.22 a) and Fig. 3.22 c). Thus, consistent with the spectral behavior at $Re_c = 0.5 \times 10^6$, which is reproduced in Fig. 3.22 b), the moderate-to-high frequency modes at the airfoil leading edge are attenuated after the high-energy phase of the dynamic stall process. Prior to the ejection of the LECS, however, the energy spectra at $Re_c = 1.0 \times 10^6$ is observed to be significantly different from the corresponding spectra at the lower Reynolds numbers. This distinction stems from the presence of moderate-amplitude fluctuations aft of the airfoil mid-chord at $Re_c = 1.0 \times 10^6$. During this pre-LECS phase, the velocity fluctuations span a wide range of Strouhal numbers, between $St = 0.35$ and $St = 3.5$, and propagate upstream with increasing angles of attack. This upstream movement of the moderate-amplitude velocity fluctuations is indicated by an arrow in Fig. 3.21 c). The energy spectra prior to the emergence of the LECS reflect the perturbations in the flow

that result primarily from the trailing-edge vortical structures, which had been identified previously from Fig. 3.19 i)-ii). The elevated amplitude of the velocity spectra at $Re_c = 1.0 \times 10^6$ therefore suggests that the velocity perturbations are amplified more strongly in the separated shear layer at the highest Reynolds number.

3.4 Linear Stability Analysis

The purpose of this section is to provide a comparison between the dominant modes of velocity fluctuations that were estimated using a combined EMD and Hilbert transform approach with those that were calculated using linear stability analysis. The linear stability predictions were obtained by extracting the convectively-unstable, two-dimensional perturbation modes from the Orr-Sommerfeld equations using a numerical procedure that was outlined in Chapter 2. As a reminder from Chapter 2, the phase-averaged x-velocity component, u, was used to obtain the base flow in the stability analysis routine. For a single instance of the the stability routine, the y-dependent, phase-averaged u-velocity was extracted at a fixed chordwise location for a given angle of attack. A hyperbolic tangent curve was then fitted over $u(y)$ to obtain the final base flow profile, which was then used as the primary input to initiate the stability calculation. The process was then repeated for several $u(y)$ profiles that were extracted at regular x/c locations across the entirety of the airfoil chord, producing an x-dependent eigenvalue spectra of the unstable velocity perturbations.

The instability spectra of the velocity field at $\alpha = 18.64°$, $\alpha = 20.63°$, and $\alpha = 24.72°$, corresponding to $Re_c = 0.2 \times 10^6$, $Re_c = 0.5 \times 10^6$, and $Re_c = 1.0 \times 10^6$ are presented in Fig. 3.23. These angles of attack were selected since they belong to the phase of the dynamic stall process that is characterized by rapid LECS ejection, as shown previously in Fig. 3.19. The colorbar in Fig. 3.23 represents the amplitude growth rate of the perturbations as a function of the chordwise position, along the x-axis, and the modal frequencies, along the y-axis. These frequencies are presented in terms of the chord-based Strouhal number. A thresholding filter is used in Fig. 3.23 to blank all of the plot regions that are associated with inconsequentially small growth rates, as defined by $-k_i < 0.1$. A series of velocity vectors are also included at regular intervals of $\Delta(x/c) = 0.026$ and $\Delta(y/c) = 0.017$, for reference. It should be mentioned that the y-axis in all of the stability results has been re-defined such that the origin lies on the surface of the airfoil mask at each x/c location. From Fig. 3.23, the instability spectra near the airfoil leading edge for each Reynolds number is associated with a series of unstable modes, with $k_i < 0$, that span a wide range of frequencies. It is also important, however, to note that the predictions of the linear stability analysis are only applicable

to the very initial phase of the shear layer transition process, which is characterized by an exponential growth in the perturbation amplitude. For a canonical shear layer, this exponential growth phase saturates quickly as the amplified non-linear effects begin to dominate the overall transition process. [52, 53] Thus, the discussion henceforth is focused solely on the eigenvalue estimates for the velocity profile at $x/c = -0.15$, which corresponds to the furthest upstream acquisition of the current TR-PIV experiments.

The variation in $-k_i$ as a function of the displacement-thickness based Strouhal number, St_{δ^*}, for the base velocity profile at $x/c = -0.15$ is presented in Fig. 3.24. As described in Chapter 2, this Strouhal definition, based on the displacement thickness and the maximum shear-layer velocity, provides a more accurate representation of the natural scales associated with the separated shear layer. It is important to note that the solid curves in Fig. 3.24 represent the average of the eigenvalue estimates across a $\Delta\alpha = \pm 0.05^\circ$ change in the angle of attack. The partially transparent color bands in Fig. 3.24 define a 68% confidence interval about the corresponding mean. This representation of the instability was selected, since it provides a measure of the degree of scatter associated with the eigenvalue estimates due to a time-dependent variation in the base flow. The narrow width of these bands is indicative of the low degree of scatter associated with the eigenvalue spectra of the present investigation, which further demonstrates that the predictions from linear stability analysis are largely insensitive to minor variations in the base flow. This behavior was predicted using a time-scale based argument presented in Section 2.4.2. The eigenvalue spectra from Fig. 3.24 also display strong resemblance with the classical shear layer instability profiles from the literature. [44, 46, 52, 53] Moreover, each of the eigenvalue profiles from Fig. 3.24 are associated with a well-defined peak. The peak growth rate of the fluctuation amplitude is observed to increase with increasing Reynolds number as the viscous-damping becomes increasingly insignificant compared to the inertial-driven effects. The higher growth rate is expected to induce an early roll up of the shear layer after the separation of the BL at the airfoil leading edge. This observation provides a possible hypothesis for the progressively smaller angle-of-attack difference between the LECS ejection and the DSV formation phases of the dynamic stall process at the higher Reynolds numbers, as described previously in Section 3.3.3.

The modal frequencies corresponding to the peak growth rates are observed from Fig. 3.24, to be largely independent of the Reynolds number. These frequencies are presented in Table 3.1 for each of the three Reynolds number cases. The average frequencies associated with the high-energy transients from Fig. 3.21 are also presented in Table 3.1 in terms of St_{δ^*}, in order to enable a direct comparison with the frequency estimates from linear stability analysis. From Table 3.1, the Strouhal estimates for the most unstable modes from linear stability analysis are found to be largely consistent with the high-energy modes that were determined using a combined EMD and Hilbert transform approach. Unlike the chord-based

Strouhal number, which was shown in Section 3.3.4 to have a strong dependence on the Reynolds number, the displacement-thickness based Strouhal scaling of the high-energy modes is observed to vary weakly with the Reynolds number. This observation indicates that the LECS-shedding process is similar across the three Reynolds numbers. Additionally, the range of displacement-thickness-based Strouhal numbers, between $St_{\delta^*} = 0.09$ and $St_{\delta^*} = 0.14$, has been associated in the literature [46–48] with the Kelvin-Helmholtz instability of canonical shear layer profiles. It should, however, be noted that the Kelvin-Helmholtz modes are generally associated with an inviscid instability of free shear layers, as governed by the Rayleigh equation. [52, 53, 66] But an increase in the Reynolds number, in the present investigation, was not found to have any significant effect on the frequencies associated with the most amplified modes of the velocity perturbations. The Reynolds number independence of the modal frequencies results from a rapid convergence of the viscous Orr-Sommerfeld modes to the inviscid Rayleigh modes, as documented in the literature. [67, 68] The Kelvin-Helmholtz instability mechanism is therefore ascertained as the fundamental physical process that initiates the growth of perturbations in the separated shear layer, leading eventually to the formation of discrete vortical structures near the airfoil leading edge.

3.5 Tables and Figures

Table 3.1: Comparison between the linear stability analysis and TR-PIV estimates of the most dominant perturbation modes during the ejection of LECS.

$Re_c(\times 10^6)$	α°	$(St_{\delta^*})_{LST}$	$(St_{\delta^*})_{EXP}$
0.20	18.64	0.13	0.14
0.50	20.63	0.10	0.09
1.00	24.72	0.14	0.11

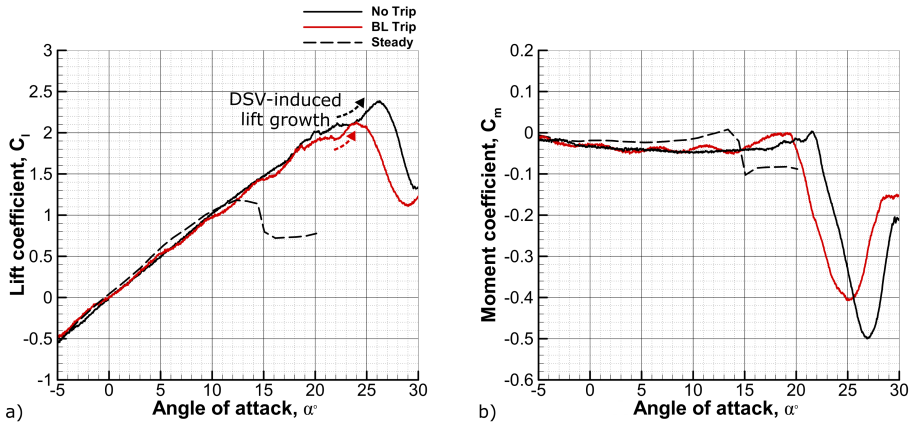

Figure 3.1: Airfoil a) lift and b) quarter-chord pitching moment coefficients at $Re_c = 0.5 \times 10^6$.

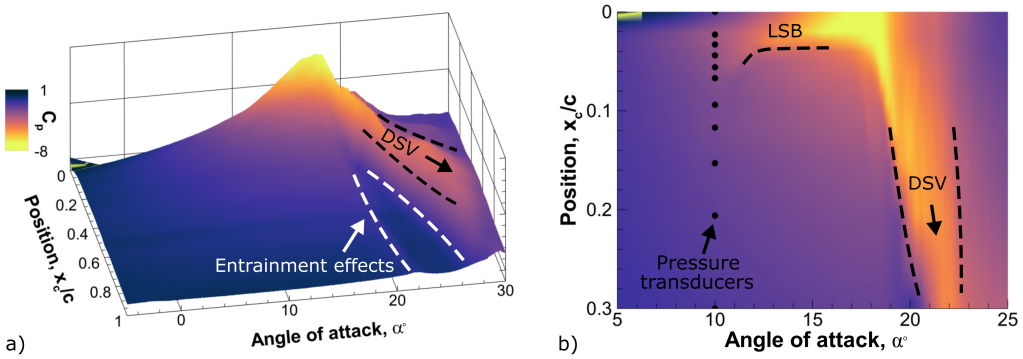

Figure 3.2: Pressure evolution during dynamic stall across a) entire upper surface, and b) near the airfoil leading edge, for $Re_c = 0.5 \times 10^6$.

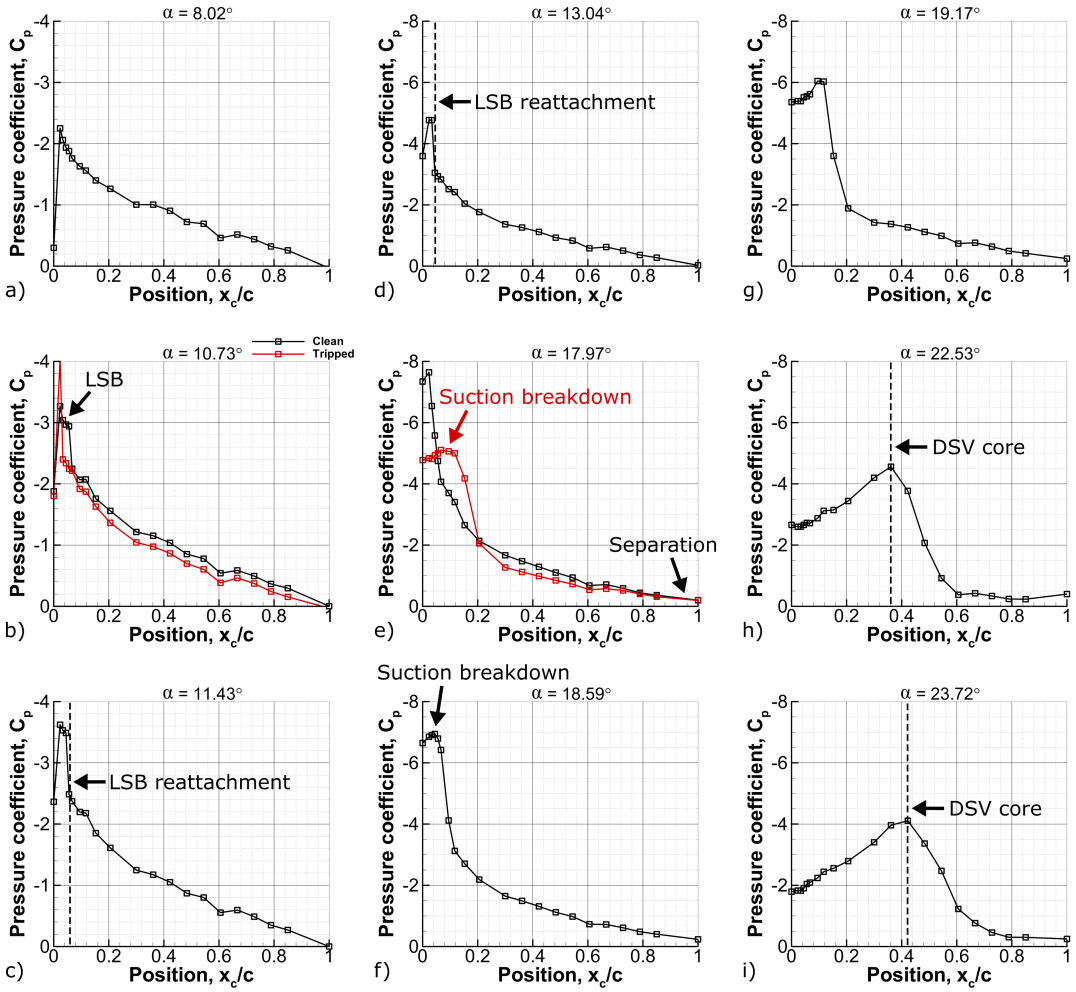

Figure 3.3: Chordwise pressure distributions at select angles of attack corresponding to the dynamic stall process at $Re_c = 0.5 \times 10^6$.

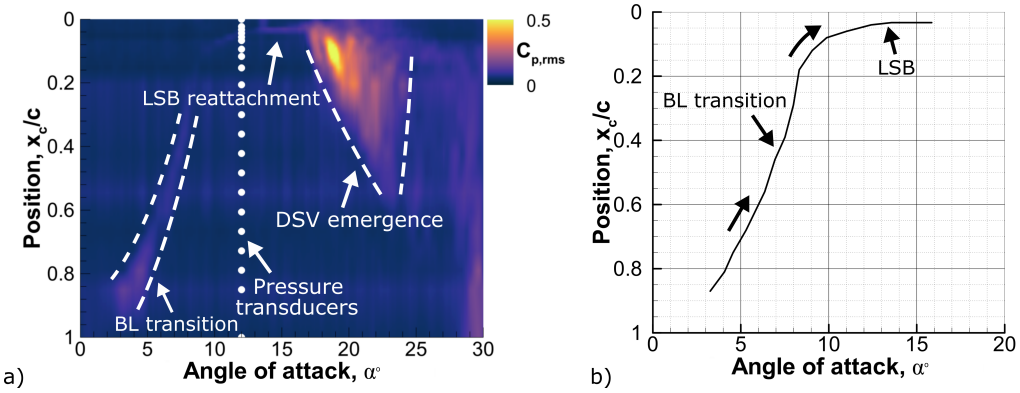

Figure 3.4: a) Root mean square of the pressure acquisition across the airfoil upper surface, and b) approximate motion of the boundary layer transition zone, at $Re_c = 0.5 \times 10^6$.

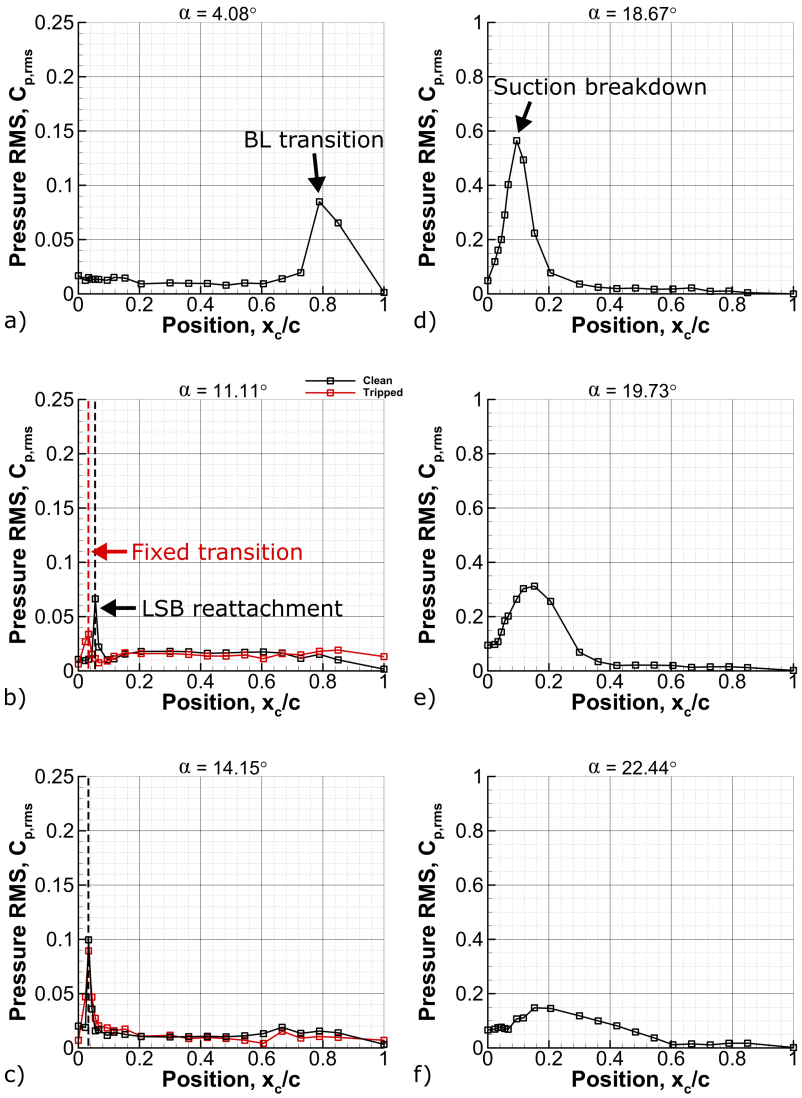

Figure 3.5: Chordwise distributions of the root-mean-square pressure at select instances of the dynamic stall process corresponding to $Re_c = 0.5 \times 10^6$.

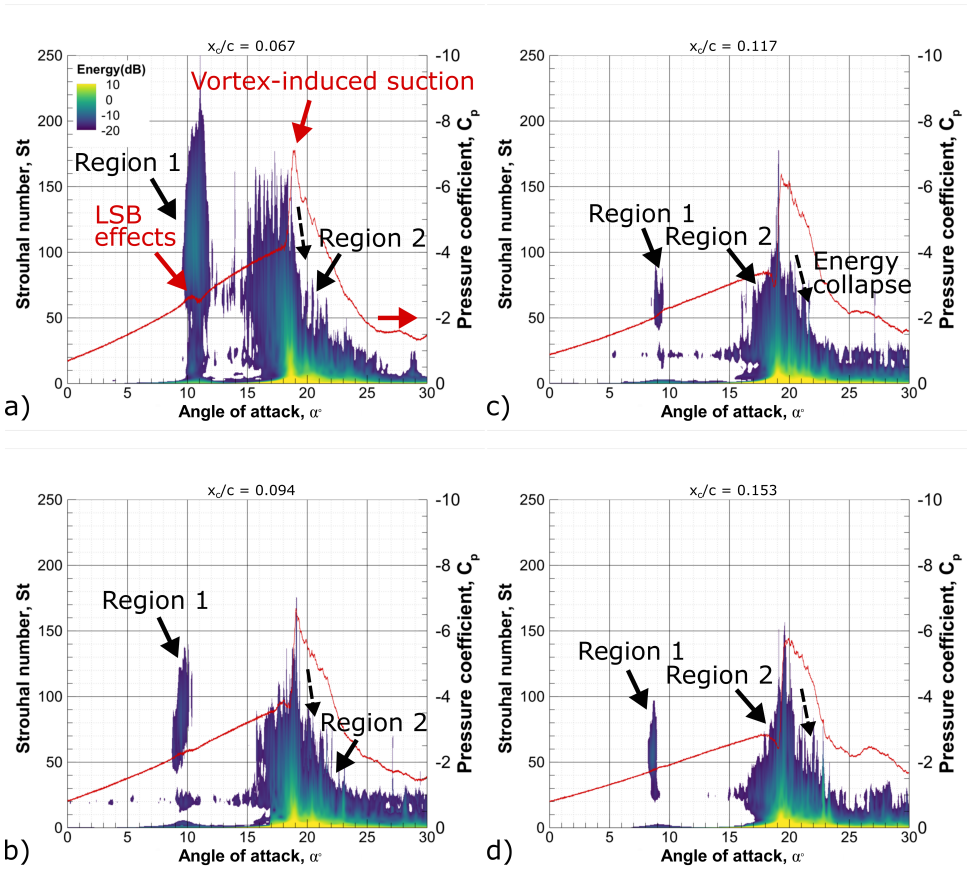

Figure 3.6: Energy spectra of the pressure fluctuations for the clean airfoil at select chordwise locations ($Re_c = 0.5 \times 10^6$).

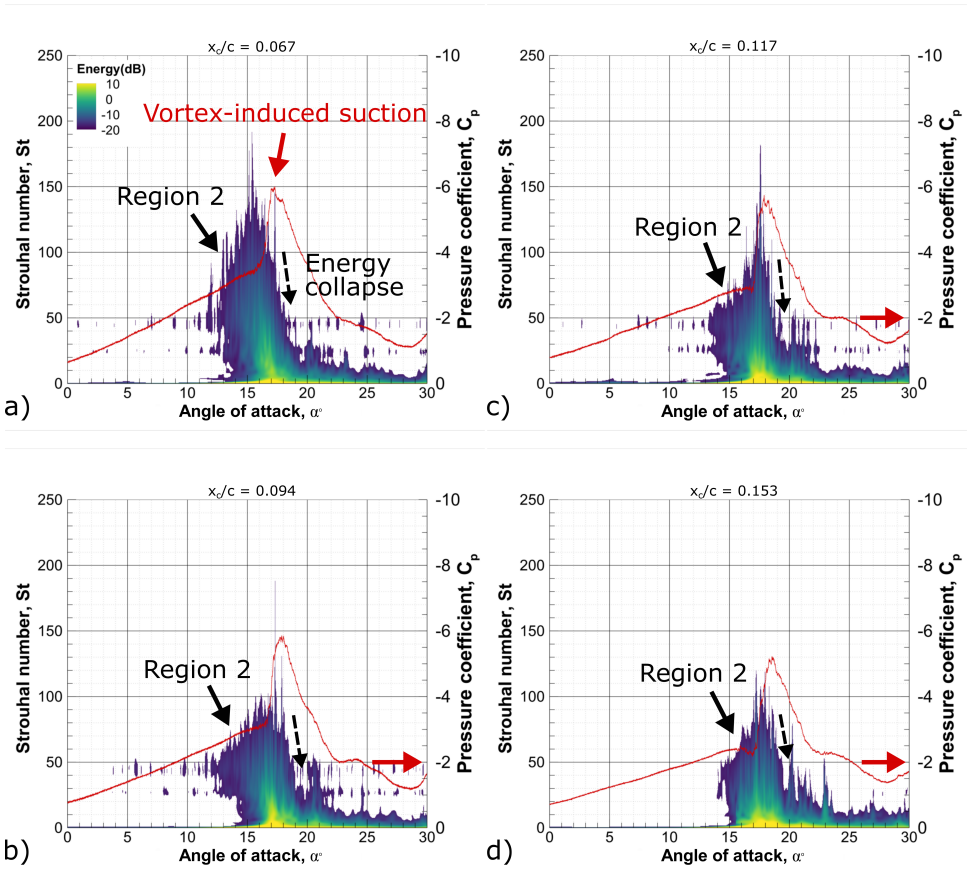

Figure 3.7: Energy spectra of the pressure fluctuations for the tripped airfoil configuration at select chordwise locations ($Re_c = 0.5 \times 10^6$).

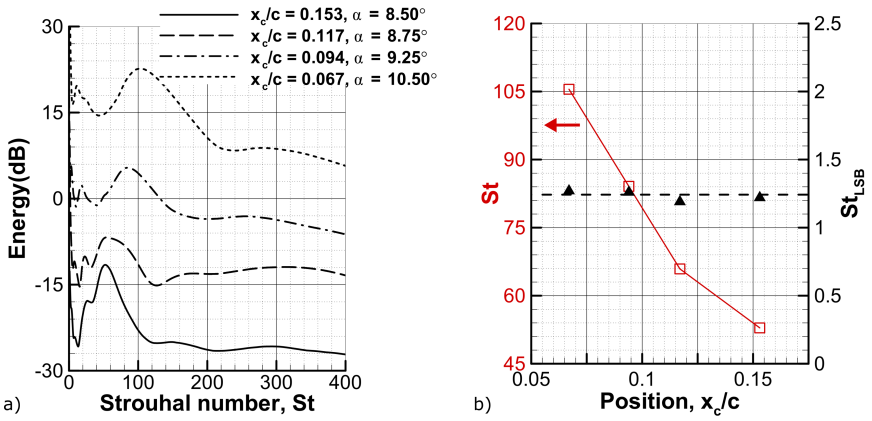

Figure 3.8: a) Pressure spectra corresponding to different chordwise positions of the LSB reattachment zone, and b) Center-frequency scaling associated with the spatial contraction of the LSB, at $Re_c = 0.5 \times 10^6$.

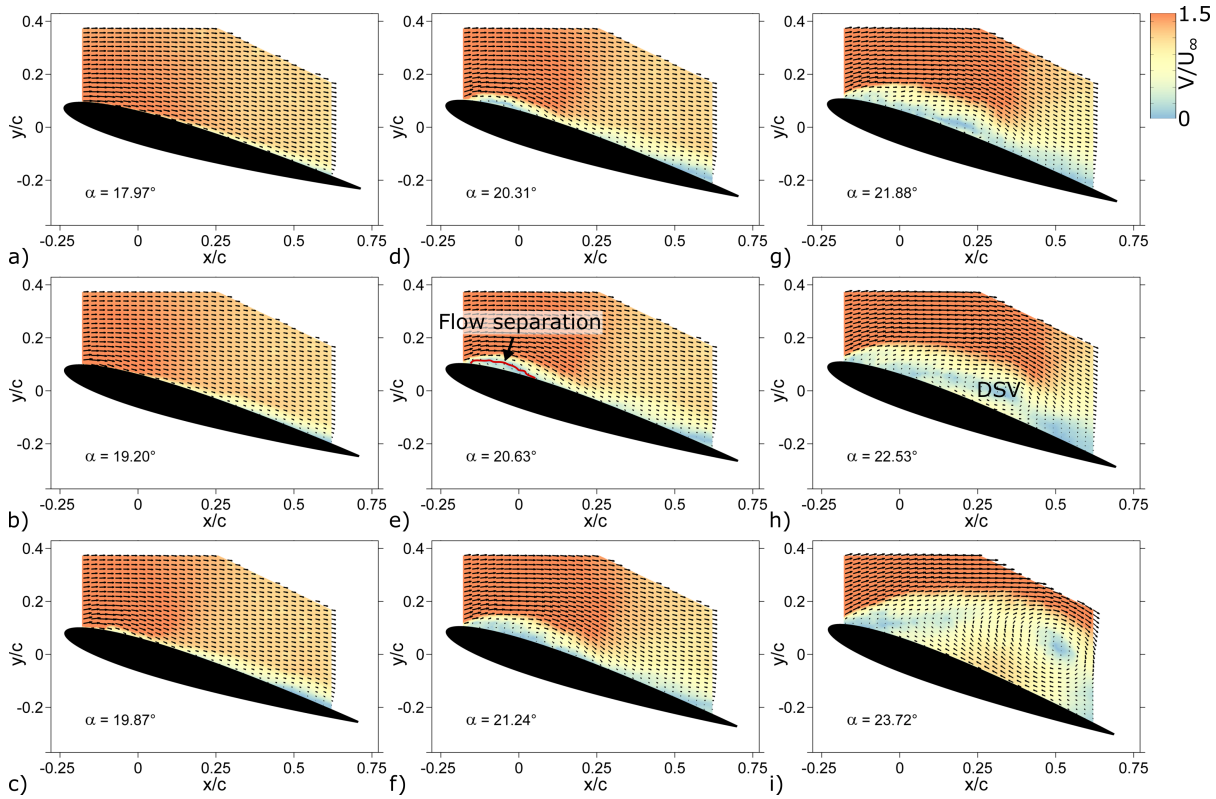

Figure 3.9: Velocity field contours for select instances of the dynamic stall process at $Re_c = 0.5 \times 10^6$.

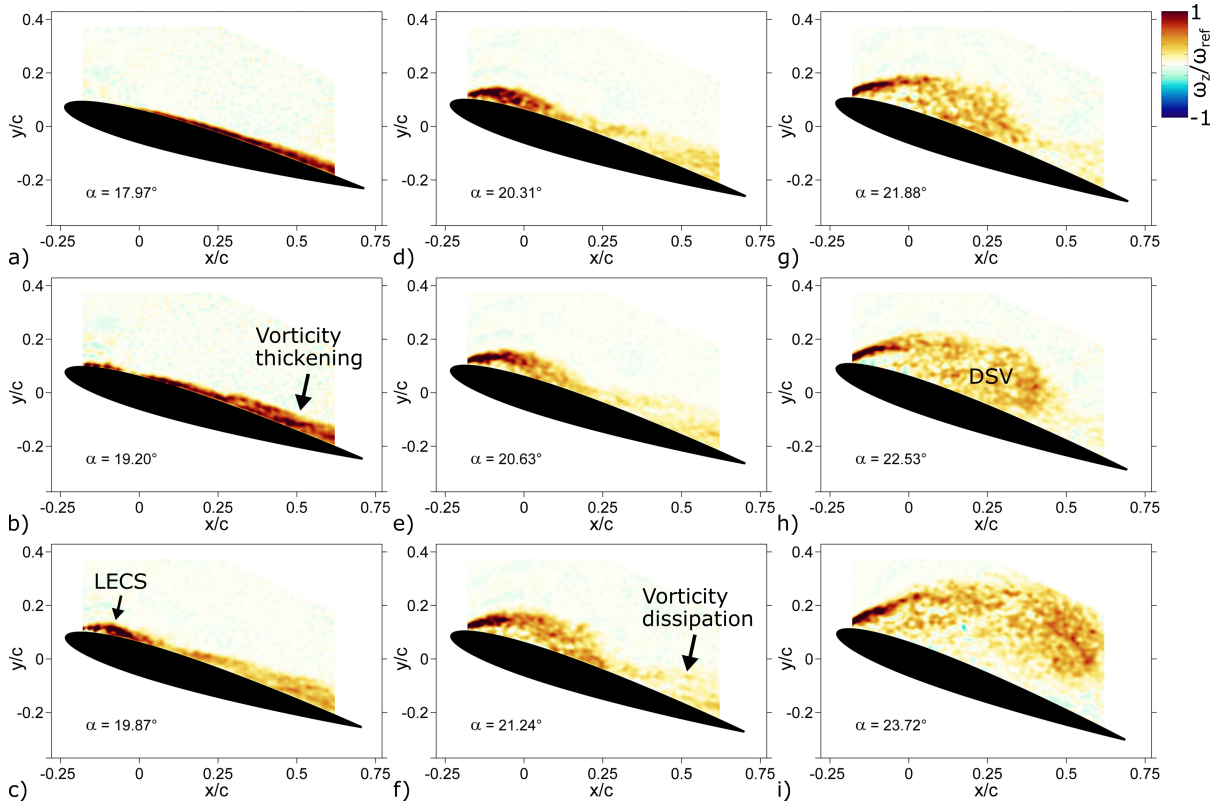

Figure 3.10: Vorticity field contours along the z axis for select instances of the dynamic stall process at $Re_c = 0.5 \times 10^6$.

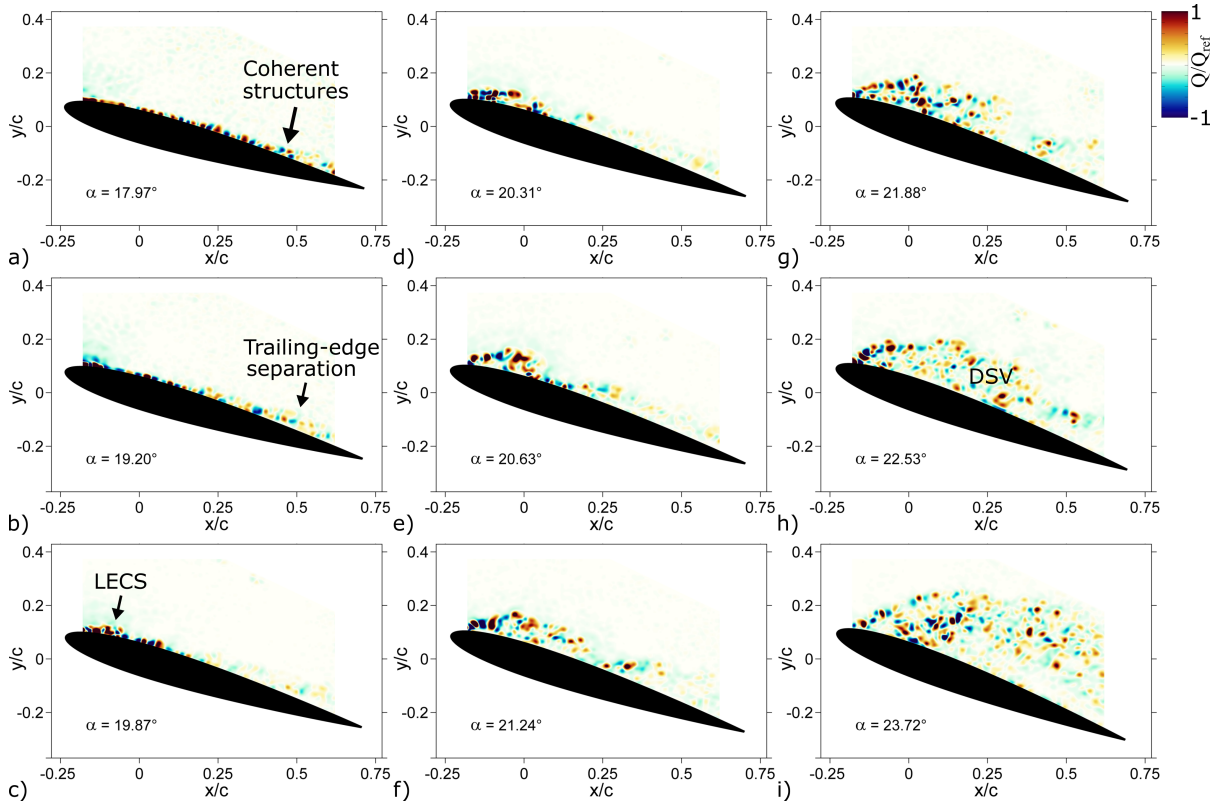

Figure 3.11: Contours of the instantaneous Q criterion for select instances of the dynamic stall process at $Re_c = 0.5 \times 10^6$.

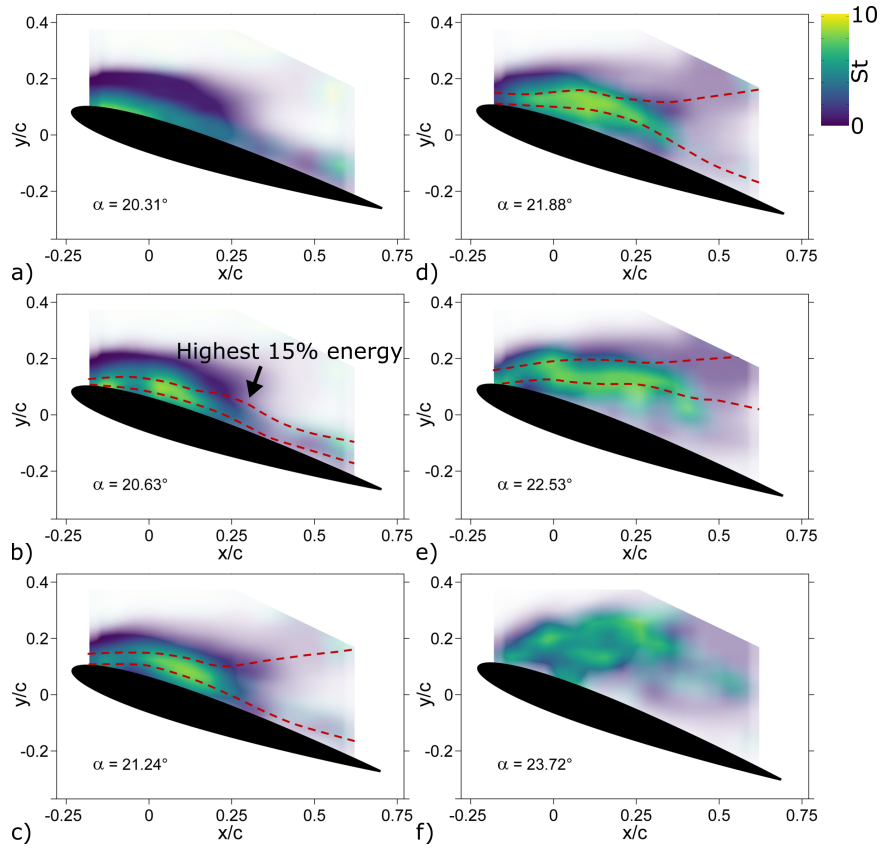

Figure 3.12: Frequency field contours corresponding to the most dominant mode of velocity fluctuations across all IMFs at select angles of attack ($Re_c = 0.5 \times 10^6$).

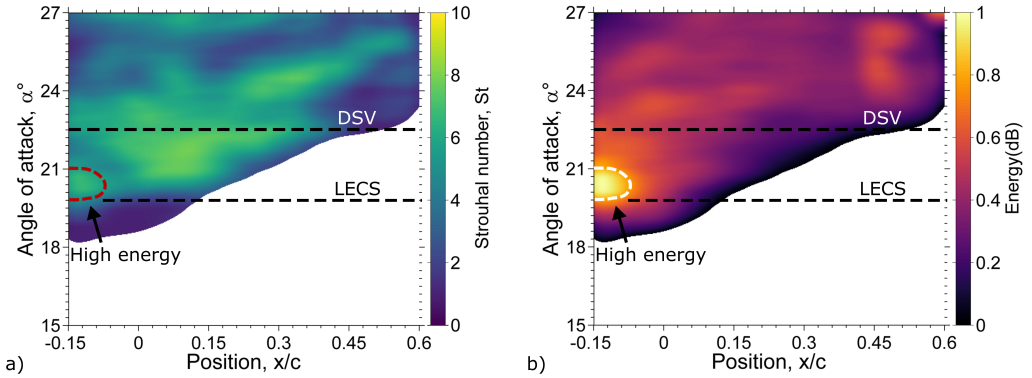

Figure 3.13: The time-dependent variation of a) frequency and b) energy associated with the most-amplified velocity fluctuations at each chordwise location along the airfoil upper surface, for $Re_c = 0.5 \times 10^6$.

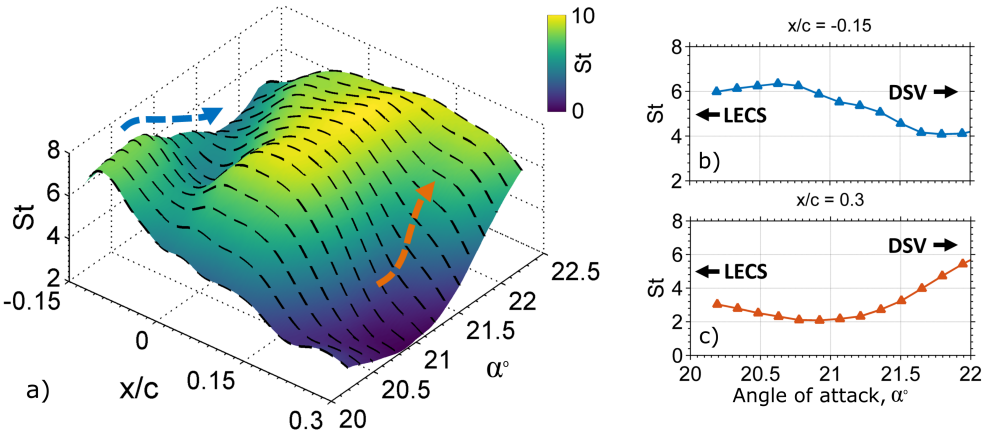

Figure 3.14: a) Surface contour of the dominant frequencies between LECS ejection and DSV emergence; Dominant frequency variation with angle of attack at b) $x/c = -0.15$, and c) $x/c = 0.3$ ($Re_c = 0.5 \times 10^6$).

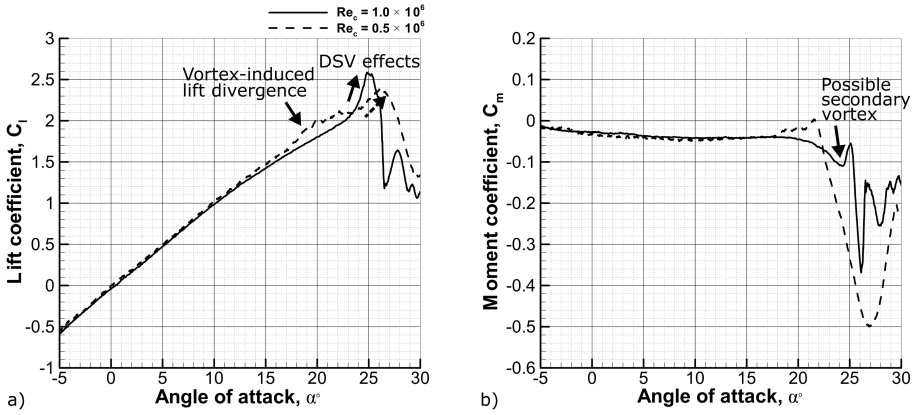

Figure 3.15: Airfoil a) lift and b) quarter-chord pitching moment coefficients at $Re_c = 0.5 \times 10^6$ and $Re_c = 1.0 \times 10^6$.

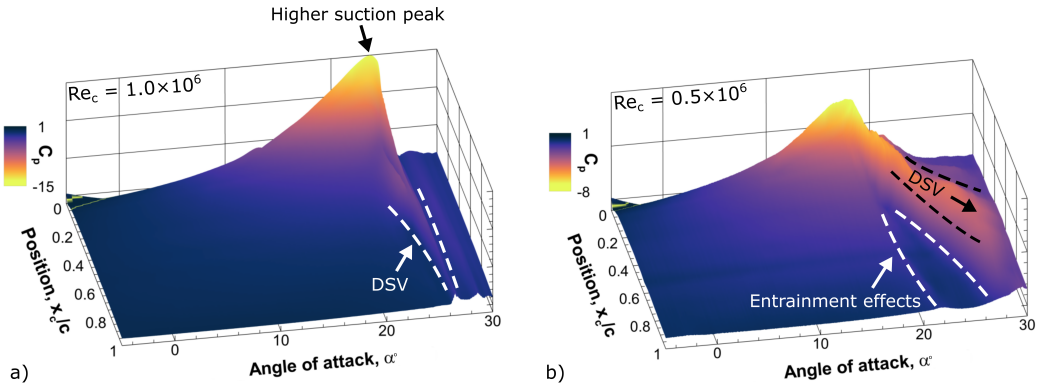

Figure 3.16: Surface pressure evolution for the dynamic stall process at a) $Re_c = 1.0 \times 10^6$, and b) $Re_c = 0.5 \times 10^6$.

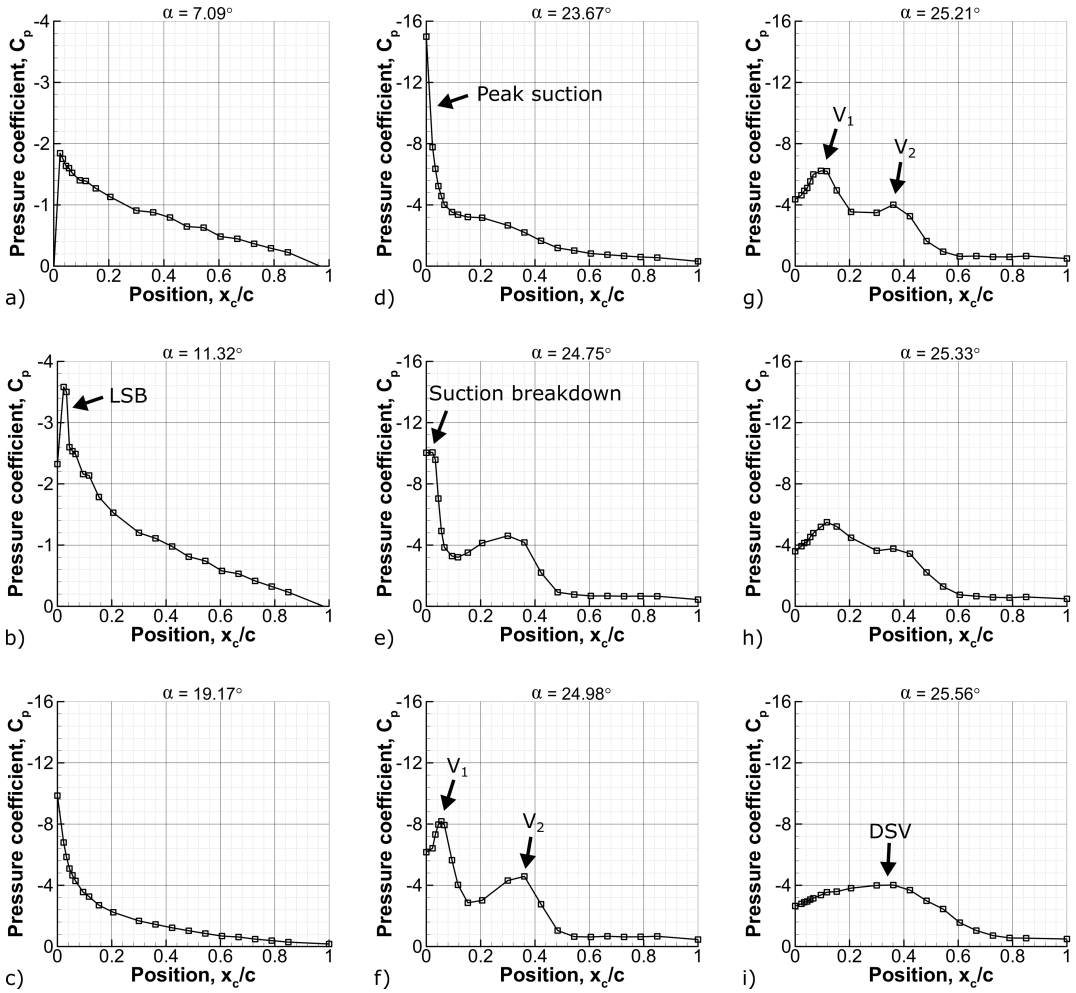

Figure 3.17: Chordwise pressure distributions at select angles of attack corresponding to the dynamic stall process at $Re_c = 1.0 \times 10^6$.

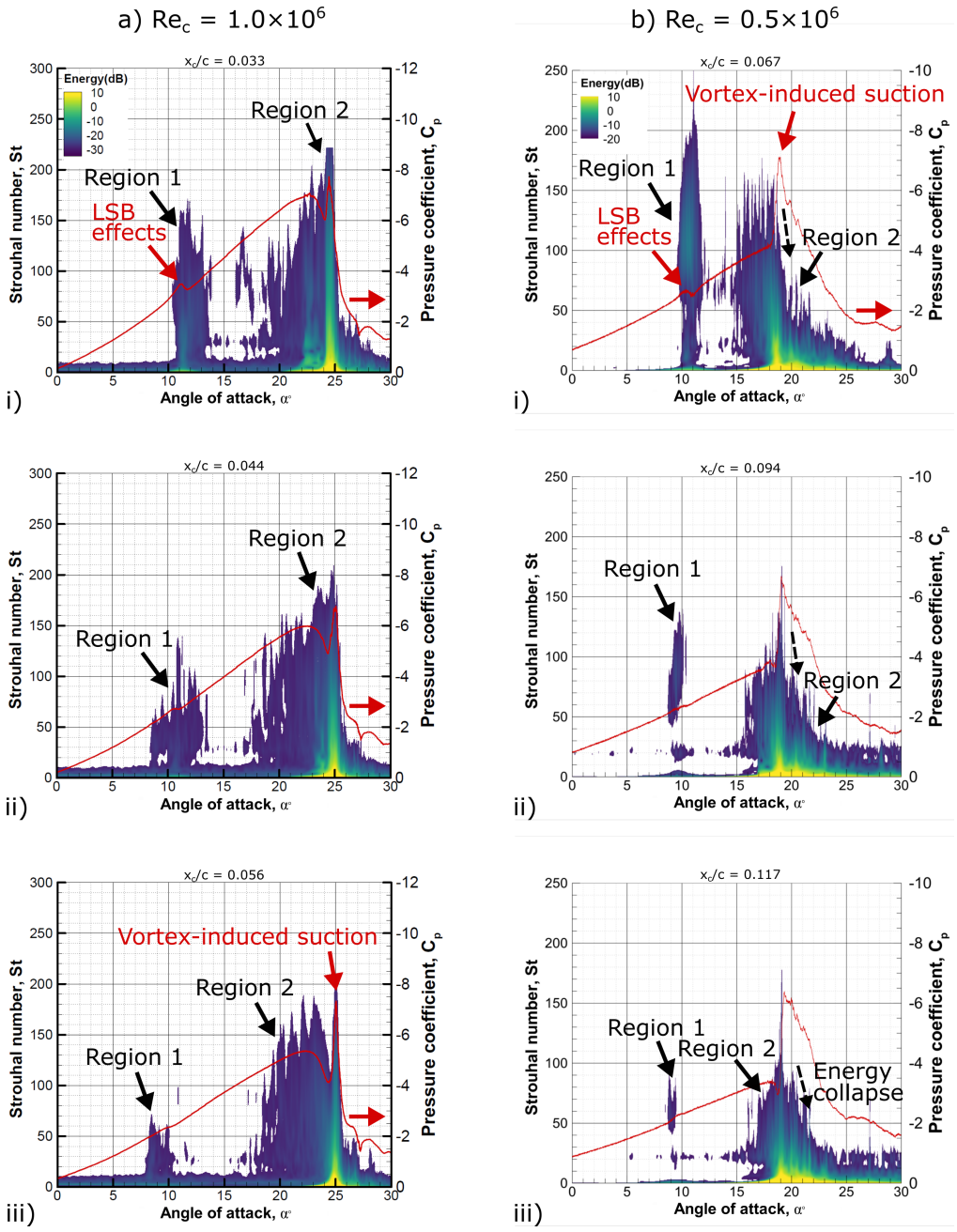

Figure 3.18: Energy spectra of the pressure fluctuations at select chordwise locations for a) $Re_c = 1.0 \times 10^6$, and b) $Re_c = 0.5 \times 10^6$.

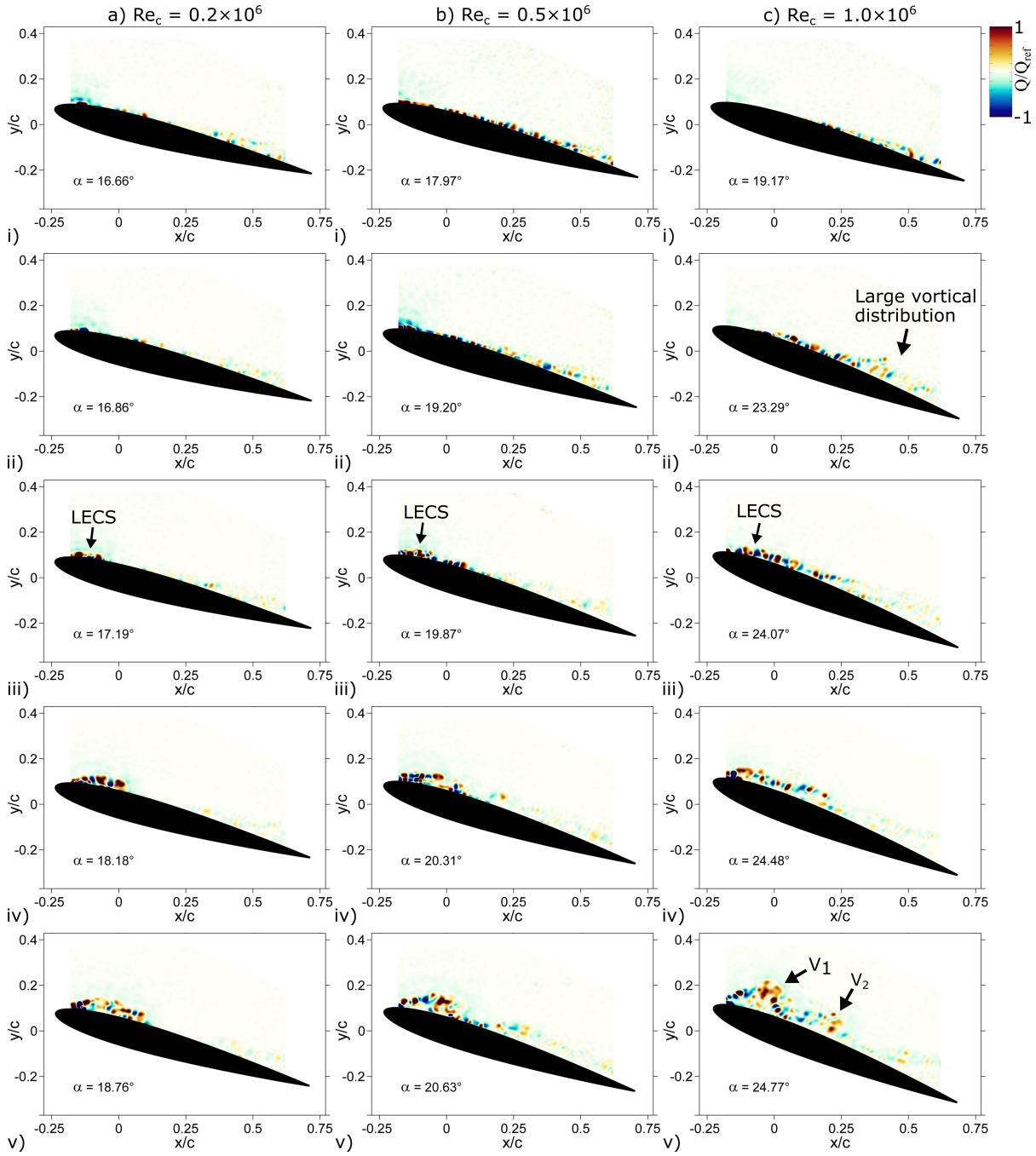

Figure 3.19: Contours of the instantaneous Q criterion for select instances of the dynamic stall process at a) $Re_c = 0.2 \times 10^6$ b) $Re_c = 0.5 \times 10^6$, and c) $Re_c = 1.0 \times 10^6$.

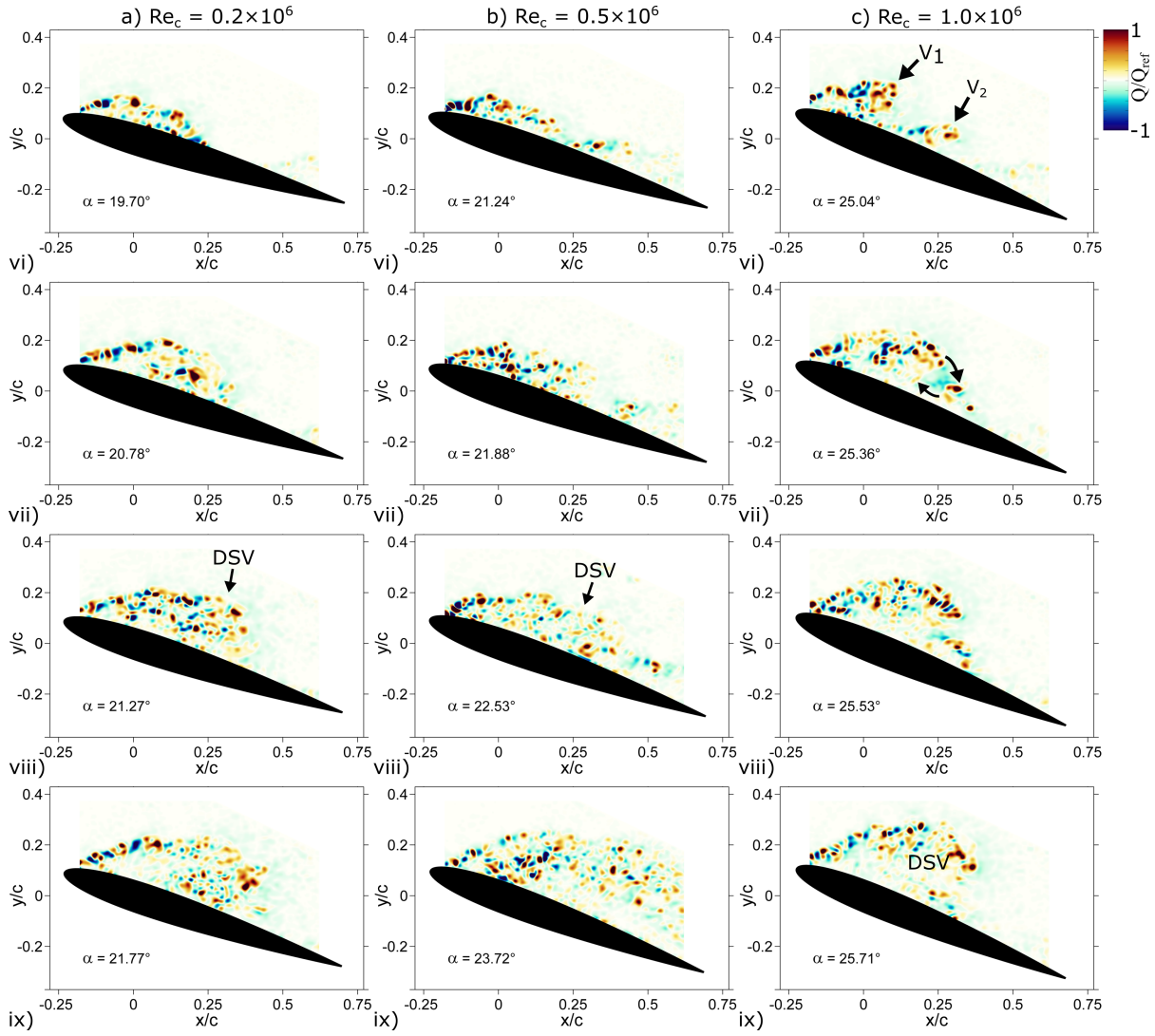

Figure 3.19: (cont.) Contours of the instantaneous Q criterion for select instances of the dynamic stall process at a) $Re_c = 0.2 \times 10^6$ b) $Re_c = 0.5 \times 10^6$, and c) $Re_c = 1.0 \times 10^6$.

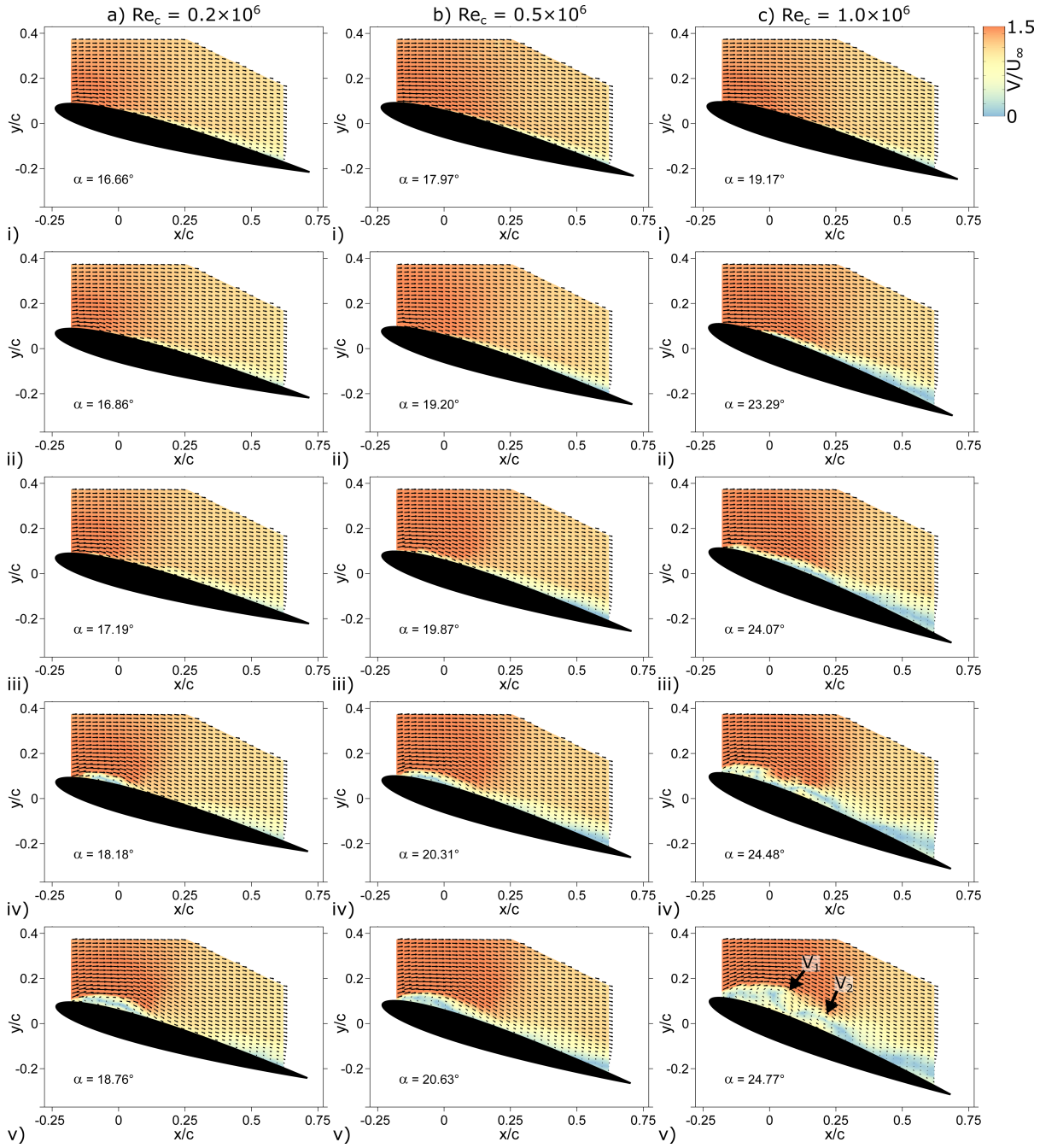

Figure 3.20: Velocity field contours for select instances of the dynamic stall process at a) $Re_c = 0.2 \times 10^6$ b) $Re_c = 0.5 \times 10^6$, and c) $Re_c = 1.0 \times 10^6$.

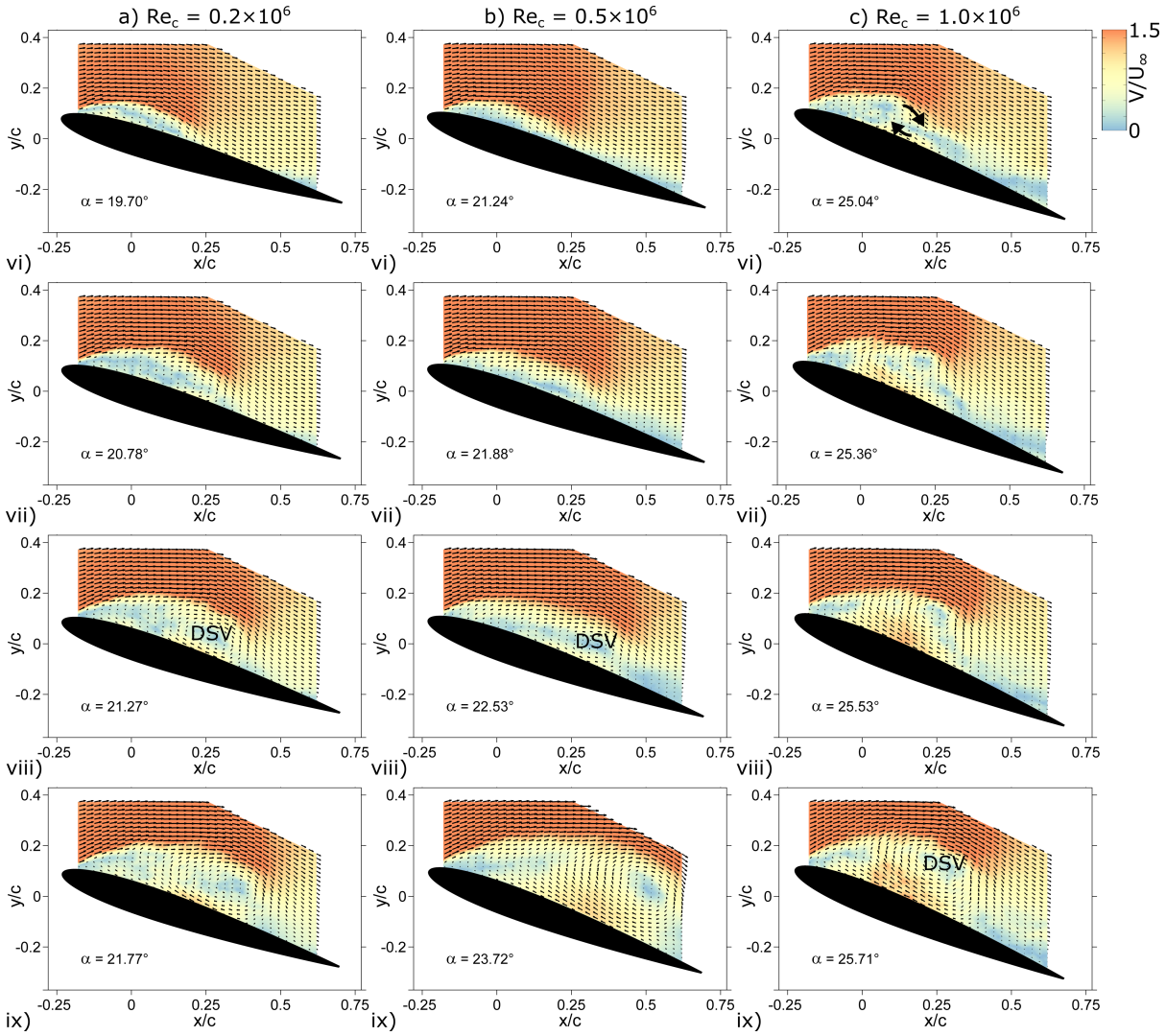

Figure 3.20: (cont.) Velocity field contours for select instances of the dynamic stall process at a) $Re_c = 0.2 \times 10^6$ b) $Re_c = 0.5 \times 10^6$, and c) $Re_c = 1.0 \times 10^6$.

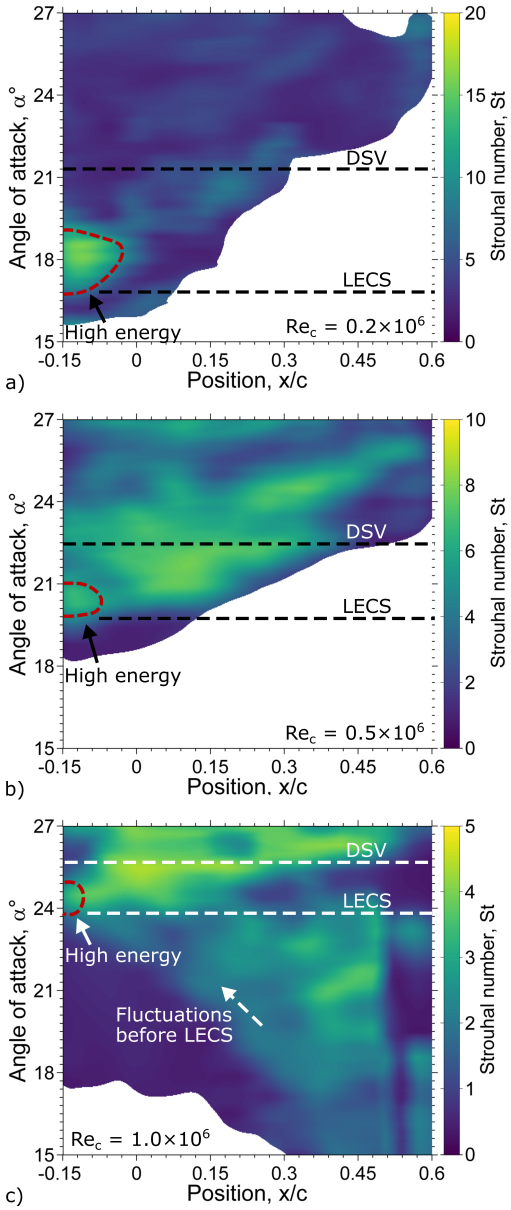

Figure 3.21: The time-dependent variation of frequency associated with the most-amplified velocity fluctuations at each chordwise location along the airfoil upper surface, for a) $Re_c = 0.2 \times 10^6$, b) $Re_c = 0.5 \times 10^6$, and c) $Re_c = 1.0 \times 10^6$.

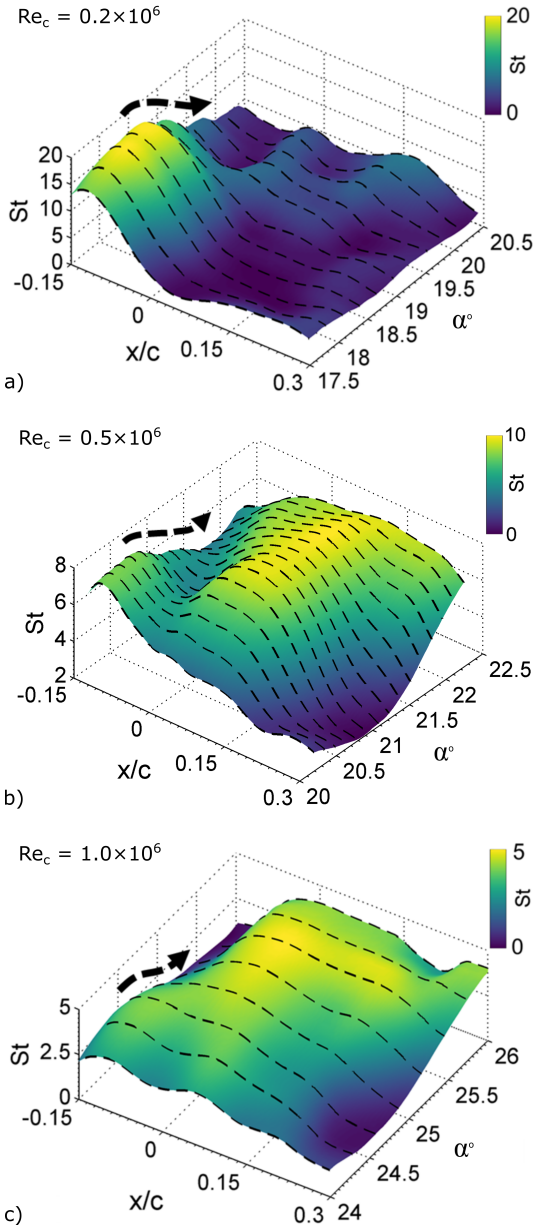

Figure 3.22: Surface contours of the dominant frequencies between LECS ejection and DSV emergence for the dynamic stall processes at a) $Re_c = 0.2 \times 10^6$, b) $Re_c = 0.5 \times 10^6$, and c) $Re_c = 1.0 \times 10^6$.

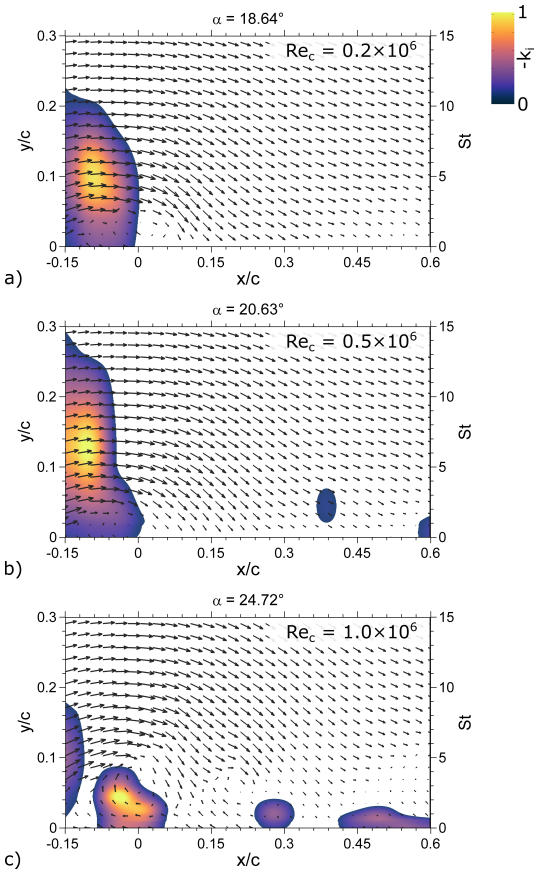

Figure 3.23: Eigenvalue spectra of the unstable perturbation modes associated with the phase-averaged velocity fields during an equivalent phase of the dynamic stall process at a) $Re_c = 0.2{\times}10^6$, b) $Re_c = 0.5{\times}10^6$, and c) $Re_c = 1.0 \times 10^6$.

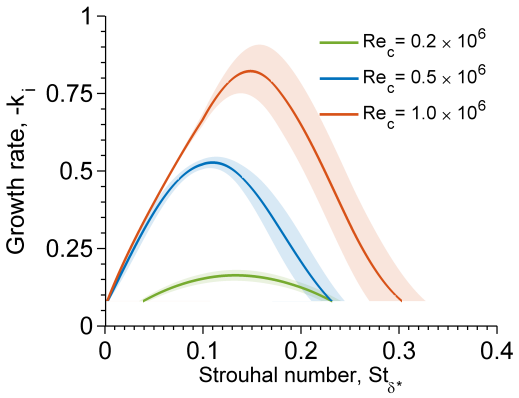

Figure 3.24: Eigenvalue spectra of unstable perturbation modes for the velocity profiles at $x/c = -0.15$ corresponding to a) $Re_c = 0.2 \times 10^6$, b) $Re_c = 0.5 \times 10^6$, and c) $Re_c = 1.0 \times 10^6$.

Chapter 4

Conclusions and Future Work

A series of wind tunnel experiments was conducted on an NACA 0012 airfoil undergoing a linear pitch ramp maneuver at a fixed dimensionless pitch rate of $\Omega^+ = 0.05$ and across three transitional Reynolds numbers, $Re_c = 0.2 \times 10^6$, $Re_c = 0.5 \times 10^6$, and $Re_c = 1.0 \times 10^6$. The primary objectives of these experiments were to perform a detailed, physics-based analysis of a canonical dynamic stall process, including a description of the salient features in the near-wall flow prior to the appearance of large-scale flow separation, the instability mechanism at the airfoil leading edge, and a quantitative characterization of the spatio-temporal spectra of the dynamic stall flowfield. Additionally, the off-body flow dependence on the freestream Reynolds number was also examined to highlight the physical differences in the vortex evolution during the emergence of the DSV. These objectives were addressed through high-fidelity measurements of the surface pressure and the velocities in the off-body flowfield.

4.1 Surface Pressure Results

A series of pressure transducers distributed across the airfoil surface was used to acquire the time-dependent surface pressure evolution during the dynamic stall process. The initial phase of the dynamic stall process was characterized by a rapid growth of suction near the airfoil leading edge. During this initial phase, an estimate of the root-mean-square of the surface pressure at $Re_c = 0.5 \times 10^6$ was used to identify the region of BL transition, which was observed to initiate at the airfoil trailing edge and move upstream with increasing angles of attack. With further increase in the airfoil angle of attack, a characteristic plateau was identified in the surface pressure distribution for both $Re_c = 0.5 \times 10^6$, and $Re_c = 1.0 \times 10^6$. This feature was associated with the formation of an LSB at the airfoil leading edge. The LSB was further observed to contract with increasing angles of attack, as inferred from the upstream movement of the characteristic pressure signature associated with LSB reattachment. The LSB formation process was also found to be inhibited during forced transition, which was achieved using a BL trip, installed immediately downstream of the airfoil leading edge. The peak suction magnitude of $C_p = -14.98$ at $Re_c = 1.0 \times 10^6$ was found to be significantly larger than

the corresponding peak at $Re_c = 0.5 \times 10^6$, which was measured at $C_p = -7.63$. Further increase in the angle of attack beyond the peak C_p at $Re_c = 0.5 \times 10^6$ was associated with a rapid collapse in suction at the airfoil leading edge. The emergence of the DSV was accompanied by the growth of a large-scale region of low pressure across the upper surface of the airfoil. For $Re_c = 1.0 \times 10^6$, the emergence of DSV-induced suction was preceeded by the appearance of two vortex-induced suction peaks, indicating that the formation of two distinct vortices. These distinct suction peaks were observed to gradually coalesce into a single, significantly larger region of reduced pressure, with increasing angles of attack. The character of the C_p evolution at $Re_c = 1.0 \times 10^6$, after the breakdown of suction and leading up to the emergence of a single DSV-induced suction peak, was therefore, markedly different from pressure acquisition at the lower Reynolds number. The emergence and the subsequent convection of the DSV were also associated with a characteristic suction imprint on the time-dependent surface pressure field. For $Re_c = 0.5 \times 10^6$, a transient pressure recovery phase due to vortex-induced fluid motion towards the airfoil surface was also identified in the aft region of the airfoil prior to the appearance of the DSV. While the maximum lift attained by the airfoil was significantly larger at the higher Reynolds number, the associated phenomenon of lift stall was found to occur earlier at $Re_c = 1.0 \times 10^6$ in comparison with $Re_c = 0.5 \times 10^6$. This observation indicated that the DSV, after formation, convects away from the airfoil surface at a much faster rate during the dynamic stall process at $Re_c = 1.0 \times 10^6$, in comparison with the lower Reynolds number.

The energy spectra of the high time-resolution surface pressure measurements, acquired across the leading-edge region of the airfoil, were calculated using continuous wavelet transformations. These spectra were associated with a transient region of increased unsteadiness due to the reattachment of the LSB. The spatial contraction of the LSB at $Re_c = 0.5 \times 10^6$ was accompanied by an increase in the center frequency of the LSB-induced pressure fluctuations. These center frequencies were observed to span a range of chord-based Strouhal numbers between $St = 50$ and $St = 105$. Using the projection of the chordwise extent of LSB in the vertical plane as the characteristic length scale, the set of frequencies, between $St = 50$ and $St = 105$, was observed to collapse to an approximately constant value of $St_{LSB} = 1.2$. It is conjectured that an unsteady actuation at the LSB natural frequencies can help prolong the lifespan of the LSB, by forcing the transition of the separated shear layer, and delaying the large-scale separation of flow and in turn the emergence of the DSV. Beyond the LSB-induced transients, a second, more prolonged, region of amplified fluctuations was also observed in the lead up to the collapse of leading-edge suction and the inception of the DSV. The appearance of the vortex-induced suction peak was accompanied by a rapid collapse in the spectral energy at the higher frequency modes in the surface pressure fluctuations. The qualitative features of the pressure spectra were found to be consistent for both $Re_c = 0.5 \times 10^6$ and $Re_c = 1.0 \times 10^6$.

4.2 TR-PIV Results

The evolution of the flow in the region above the airfoil upper surface was studied using a combination of velocity, vorticity and Q-criterion contours at several angles of attack. The initial state of the flow, described in this study, was characterized by a stochastic distribution of vortical structures in the immediate vicinity of the airfoil surface. Increasing the angle of attack, beyond the collapse of the suction peak, was accompanied by a rapid ejection of coherent structures, resulting from an instability of the leading-edge separated shear layer. For $Re_c = 0.2 \times 10^6$ and $Re_c = 0.5 \times 10^6$, the continued production of vortices and the associated mutual interactions were observed to cause a gradual coalescence of the LECS into a single, coherent DSV. At $Re_c = 1.0 \times 10^6$, however, the fine-scale coherent structures near the airfoil surface were found to amalgamate into two distinct regions, which were identified as the primary and secondary vortices. With an increase in the angle of attack, the distinct secondary vortex was observed to gradually combine with the primary vortex, leading to the emergence of a single, coherent DSV. The co-rotating vortex merging process had been conjectured previously from the surface pressure distribution, as described earlier. It should be noted that the flow topology associated with the dual-vortex system at $Re_c = 1.0 \times 10^6$ is significantly different from the classical understanding of the DSV formation process and requires further investigation to ascertain the underlying physical mechanism, in the future.

The spatio-temporal distribution of the energy spectra for the most dominant modes of fluctuations in the velocity field was extracted through a combination of EMD and the Hilbert transform. The perturbations in the separated shear layer, from the airfoil leading edge, were associated with a state of elevated amplitude, in comparison with the outer freestream. Moreover, within the shear layer, the highest overall amplitude was observed during the initial ejection of LECS in the region near the airfoil leading edge. These features of the velocity spectra were found to be consistent across the three Reynolds numbers. The LECS-induced high energy transients were associated with average frequencies of $St = 13.98$, $St = 6.23$, and $St = 3.42$, for $Re_c = 0.2 \times 10^6$, $Re_c = 0.5 \times 10^6$, and $Re_c = 1.0 \times 10^6$, respectively. Beyond the amplified transients, the perturbations in the shear layer near the airfoil leading edge were increasingly dominated by the lower frequency modes, following a trend that was observed to be consistent with the pressure spectra during a similar phase of the dynamic stall process. The perturbations in velocity, prior to the ejection of LECS, were found to be insignificant for $Re_c = 0.2 \times 10^6$ and $Re_c = 0.5 \times 10^6$. In contrast, a series of modal perturbations with comparatively larger amplitude, spanning a wide range of frequencies between $St = 0.35$ and $St = 3.5$, were observed during an equivalent phase of the dynamic stall process at $Re_c = 1.0 \times 10^6$. Thus, the flow structures in the near-wall region, prior to the ejection of LECS, were ascertained to be more prominent at the higher Reynolds number, in comparison with $Re_c = 0.2 \times 10^6$ and $Re_c = 0.5 \times 10^6$.

4.3 Stability Analyses

A numerical implementation of the Orr-Sommerfeld equations was used to extract the convectively-unstable, two-dimensional perturbation modes associated with the phase-averaged u-velocity during the initial ejection of vortices at the airfoil leading edge. The frequencies of the most amplified modes for the base velocity, $u(x/c = -0.15, y)$, from linear stability analysis, were found to be in close agreement with the experimentally-determined average frequencies during the LECS-induced, high-amplitude transients at the airfoil leading edge. Moreover, these leading edge perturbation modes, spanning a range of displacement-thickness based Strouhal numbers between $St_{\delta^*} = 0.09$ and $St_{\delta^*} = 0.14$, were found to be consistent with the Kelvin-Helmholtz instability for canonical shear layer profiles, from the literature. The Kelvin-Helmholtz instability mechanism was therefore, confirmed as the underlying physical process that is responsible for the breakup of the separated shear layer into discrete LECS, prior to the emergence of the DSV. It is hoped that the quantitative characterization of the flow spectra, combined with the physical understanding of the instability mechanism, from the present experiments, helps provide a baseline framework for future efforts in the design of unsteady actuation systems for active control of dynamic stall.

4.4 Future Work

The following set of objectives is suggested as future work to further the understanding of the complex phenomenon of dynamic stall that was gained from the current set of investigations:

- From the current study, the flow evolution prior to the DSV emergence at $Re_c = 1.0 \times 10^6$, characterized by a dual-vortex merging process, was found to be distinct from the DSV formation process observed at the lower Reynolds numbers. However, the detailed physical mechanism responsible for the emergence of two distinct vortical structures, as opposed to a single leading-edge vortex, has not been investigated from an experimental standpoint. A combination of TR-PIV measurements with significantly higher spatio-temporal resolution than what was achieved in the current experiments and surface skin friction measurements using flush-mounted hot-film sensors is recommended to adequately capture the evolution of LSB near the airfoil leading edge and the progression of BL separation from the airfoil trailing edge. It is hypothesized that the characteristic dual-vortex behavior observed at $Re_c = 1.0 \times 10^6$ stems from a possible interaction between the LSB and the trailing-edge BL separation point.

- In the current study, the dominant frequencies of fluctuations in the flowfield, localized in the spatio-

temporal domain, were extracted through a combination of EMD and the Hilbert transform. However, the quantitative estimates for the spatio-temporally-dependent wavenumbers could not be obtained using the current set of techniques. The development of a combined EMD and Riesz transform, which is a generalized form of the Hilbert transform with extended capability for multi-dimensional signals, is recommended for a simultaneous wavenumber and frequency characterization of the nonstationary flowfield.

- An implementation of active flow control using unsteady forcing at the dominant frequencies in the flowfield, as reported in the current study, is recommended as an exploratory investigation of the active control of dynamic stall. It is hypothesized that an excitation of natural instabilities in the flow, and in particular of the LSB shear layer, will delay the large-scale separation of the flow from the airfoil leading edge that occurs after the breakdown of the LSB. This delay in BL separation will in turn, lead to a delay in LECS ejection and the emergence of the DSV. An efficient flow control methodology for the active control of dynamic stall is of great importance to the aerospace community as large overshoots in the aerodynamic forces and moments, introduced by the DSV, are detrimental to the stability and structural integrity of aircraft.

- While the current investigations focused on a primarily two-dimensional dynamic stall process, most practical realizations of this phenomenon are associated with finite-aspect-ratio-wing geometries. These finite-aspect-ratio wings are subjected to non-uniform downwash leading to a spanwise variation in the effective angle of attack. As such, it is recommended to conduct future experiments on suitable wing geomtries using time-resolved stereo or tomographic PIV to capture the full three-dimensional evolution of the flowfield, with particular emphasis on the emergence of such features as the lambda and the ring vortices.

- Finally, the current set of experiments were performed at low freestream Mach numbers such that the effects of compressibility were largely insignificant through the entirety of the dynamic stall process. It is important to extend the current investigations to higher Mach numbers, as informed from practical applications, in order to study the effects of compressibility on the dynamic stall process. These future experiments are envisaged with advanced optical flow diagnostic techniques for the simultaneous acquisition of time-dependent flow parameters ($\mathbf{u}$, p, ρ, and T) in order to effectively capture the underlying physical mechanisms in the flow, such as a possible interplay between shock waves and the LSB and its implications on the emergence of the DSV.

References

[1] Carr, L. W., McAlister, K. W., and McCroskey, W. J., "Analysis of the development of dynamic stall based on oscillating airfoil experiments," Tech. Rep. NASA-TN-D-8382, 1977.

[2] Ansell, P. J., *Unsteady modes in the flowfield about an airfoil with a leading-edge horn-ice shape*, Ph.D. thesis, University of Illinois at Urbana-Champaign, 2014.

[3] Ham, N. D., "Aerodynamic loading on a two-dimensional airfoil during dynamic stall." *AIAA Journal*, Vol. 6, No. 10, 1968, pp. 1927–1934.

[4] McCroskey, W. J., Carr, L. W., and McAlister, K. W., "Dynamic stall experiments on oscillating airfoils," *AIAA Journal*, Vol. 14, No. 1, 1976, pp. 57–63.

[5] McAlister, K. W., Carr, L. W., and McCroskey, W. J., "Dynamic stall experiments on the NACA 0012 airfoil," Tech. Rep. NASA-TP-1100, 1978.

[6] McCroskey, W. J., "The phenomenon of dynamic stall," Tech. Rep. NASA-TM-81264, 1981.

[7] McCroskey, W. J., McAlister, K. W., Carr, L. W., Pucci, S. L., Lambert, O., and Indergrand, R. F., "Dynamic stall on advanced airfoil sections," *Journal of the American Helicopter Society*, Vol. 26, No. 3, 1981, pp. 40–50.

[8] Carr, L. W., "Progress in analysis and prediction of dynamic stall," *Journal of Aircraft*, Vol. 25, No. 1, 1988, pp. 6–17.

[9] Lorber, P. F. and Carta, F. O., "Airfoil dynamic stall at constant pitch rate and high Reynolds number," *Journal of Aircraft*, Vol. 25, No. 6, 1988, pp. 548–556.

[10] Visbal, M. R., "Dynamic stall of a constant-rate pitching airfoil," *Journal of Aircraft*, Vol. 27, No. 5, 1990, pp. 400–407.

[11] Chandrasekhara, M. S., Ahmed, S., and Carr, L. W., "Schlieren studies of compressibility effects on dynamic stall of transiently pitching airfoils," *Journal of Aircraft*, Vol. 30, No. 2, 1993, pp. 213–220.

[12] Chandrasekhara, M. S., Carr, L. W., and Wilder, M. C., "Interferometric investigations of compressible dynamic stall over a transiently pitching airfoil," *AIAA Journal*, Vol. 32, No. 3, 1994, pp. 586–593.

[13] Pruski, B. J. and Bowersox, R. D. W., "Leading-edge flow structure of a dynamically pitching NACA 0012 airfoil," *AIAA Journal*, Vol. 51, No. 5, 2013, pp. 1042–1053.

[14] Mulleners, K. and Raffel, M., "The onset of dynamic stall revisited," *Experiments in Fluids*, Vol. 52, No. 3, 2012, pp. 779–793.

[15] Mulleners, K. and Raffel, M., "Dynamic stall development," *Experiments in Fluids*, Vol. 54, No. 2, 2013, pp. 1469.

[16] Deparday, J. and Mulleners, K., "Critical evolution of leading edge suction during dynamic stall," *Journal of Physics: Conference Series*, Vol. 1037, 2018, p. 022017.

[17] Deparday, J. and Mulleners, K., "Modeling the interplay between the shear layer and leading edge suction during dynamic stall," *Physics of Fluids*, Vol. 31, No. 10, 2019, pp. 107104.

[18] Visbal, M. R., "Analysis of the onset of dynamic stall using high-fidelity large-eddy simulations," *52nd AIAA Aerospace Sciences Meeting*, 2014, p. 0591.

[19] Visbal, M. R. and Garmann, D. J., "Analysis of dynamic stall on a pitching airfoil using high-fidelity large-eddy simulations," *AIAA Journal*, 2018, pp. 46–63.

[20] Wen, G. and Gross, A., "Numerical investigation of dynamic stall for a helicopter blade section," *2018 AIAA Aerospace Sciences Meeting*, 2018, p. 1557.

[21] Benton, S. I. and Visbal, M. R., "Understanding abrupt leading edge separation as a mechanism for the onset of dynamic stall," *2018 AIAA Aerospace Sciences Meeting*, 2018, p. 0356.

[22] Benton, S. I. and Visbal, M. R., "The onset of dynamic stall at a high, transitional Reynolds number," *Journal of Fluid Mechanics*, Vol. 861, 2019, pp. 860–885.

[23] Sharma, A. and Visbal, M. R., "Airfoil thickness effects on dynamic stall onset," *23rd AIAA Computational Fluid Dynamics Conference*, 2017, p. 3957.

[24] Sharma, A. and Visbal, M. R., "Numerical investigation of the effect of airfoil thickness on onset of dynamic stall," *Journal of Fluid Mechanics*, Vol. 870, 2019, pp. 870–900.

[25] Benton, S. I. and Visbal, M. R., "High-frequency forcing to delay dynamic stall at relevant Reynolds number," *47th AIAA Fluid Dynamics Conference*, 2017, p. 4119.

[26] Visbal, M. R. and Benton, S. I., "Exploration of high-frequency control of dynamic stall using large-eddy simulations," *AIAA Journal*, Vol. 56, No. 8, 2018, pp. 2974–2991.

[27] Mohan, A. T., Visbal, M. R., and Gaitonde, D. V., "Model reduction and analysis of deep dynamic stall on a plunging airfoil using dynamic mode decomposition," *53rd AIAA Aerospace Sciences Meeting*, 2015, p. 1058.

[28] Mohan, A. T., Gaitonde, D. V., and Visbal, M. R., "Model reduction and analysis of deep dynamic stall on a plunging airfoil," *Computers & Fluids*, Vol. 129, 2016, pp. 1–19.

[29] Dunne, R., Schmid, P. J., and McKeon, B. J., "Analysis of flow timescales on a periodically pitching/surging airfoil," *AIAA Journal*, 2016, pp. 3421–3433.

[30] Mohan, A. T., Agostini, L. M., Visbal, M. R., and Gaitonde, D. V., "A preliminary spectral decomposition and scale separation analysis of a high-fidelity dynamic stall dataset," *54th AIAA Aerospace Sciences Meeting*, 2016, p. 1352.

[31] Wen, G. and Gross, A., "Modal decomposition of dynamic stall for helicopter blade section," *AIAA Scitech 2019 Forum*, 2019, p. 1657.

[32] Ansell, P. J. and Mulleners, K., "Multiscale vortex characteristics of dynamic stall from empirical mode decomposition," *AIAA Journal*, 2019, pp. 1–18.

[33] Braslow, A. L., Hicks, R. M., and Harris, R. V., "Use of grit-type boundary-layer-transition trips on wind-tunnel models," Tech. Rep. NASA-TN-D-3579, 1966.

[34] Diebold, J. M., Woodard, B., Monastero, M., and Bragg, M., "Experimental study of splitter plates for use with semispan wing models," *53rd AIAA Aerospace Sciences Meeting*, 2015, p. 1227.

[35] Torrence, C. and Compo, G. P., "A practical guide to wavelet analysis," *Bulletin of the American Meteorological society*, Vol. 79, No. 1, 1998, pp. 61–78.

[36] Barlow, J. B., Rae, W. H., and Pope, A., *Low-speed wind tunnel testing*, Wiley New York, 1999.

[37] Martinuzzi, R. J., Bailey, S. C. C., and Kopp, G. A., "Influence of wall proximity on vortex shedding from a square cylinder," *Experiments in Fluids*, Vol. 34, No. 5, 2003, pp. 585–596.

[38] He, G.-S., Wang, J.-J., Pan, C., Feng, L.-H., Gao, Q., and Rinoshika, A., "Vortex dynamics for flow over a circular cylinder in proximity to a wall," *Journal of Fluid Mechanics*, Vol. 812, 2017, pp. 698–720.

[39] Hunt, J. C. R., Wray, A. A., and Moin, P., "Eddies, streams, and convergence zones in turbulent flows," Tech. Rep. CTR-S88, 1988.

[40] Gupta, R. and Ansell, P. J., "Closed-loop trailing-edge separation control system using empirical mode decomposition," *AIAA Journal*, 2018, pp. 121–131.

[41] Koll, M., Favale, J., Kirchner, B. M., Elliott, G. S., and Dutton, J. C., "Flow structure identification in the near wake of an axisymmetric supersonic base flow using MEEMD," *47th AIAA Fluid Dynamics Conference*, 2017, p. 3972.

[42] Thirumalaisamy, M. R. and Ansell, P. J., "Fast and adaptive empirical mode decomposition for multidimensional, multivariate signals," *IEEE Signal Processing Letters*, Vol. 25, No. 10, 2018, pp. 1550–1554.

[43] LeBlanc, P., Blackwelder, R., and Liebeck, R., "A comparison between boundary layer measurements in a laminar separation bubble flow and linear stability theory calculations," *Low Reynolds Number Aerodynamics*, Springer, 1989, pp. 189–205.

[44] Nishioka, M., Asai, M., and Yoshida, S., "Control of flow separation by acoustic excitation," *AIAA Journal*, Vol. 28, No. 11, 1990, pp. 1909–1915.

[45] Lang, M., Rist, U., and Wagner, S., "Investigations on controlled transition development in a laminar separation bubble by means of LDA and PIV," *Experiments in Fluids*, Vol. 36, No. 1, 2004, pp. 43–52.

[46] Yarusevych, S., Kawall, J. G., and Sullivan, P. E., "Separated-shear-layer development on an airfoil at low Reynolds numbers," *AIAA Journal*, Vol. 46, No. 12, 2008, pp. 3060–3069.

[47] Boutilier, M. S. H. and Yarusevych, S., "Separated shear layer transition over an airfoil at a low Reynolds number," *Physics of Fluids*, Vol. 24, No. 8, 2012, pp. 084105.

[48] Boutilier, M. S. H. and Yarusevych, S., "Sensitivity of linear stability analysis of measured separated shear layers," *European Journal of Mechanics-B/Fluids*, Vol. 37, 2013, pp. 129–142.

[49] Theofilis, V., Hein, S., and Dallmann, U., "On the origins of unsteadiness and three-dimensionality in a laminar separation bubble," *Philosophical Transactions of the Royal Society of London. Series A: Mathematical, Physical and Engineering Sciences*, Vol. 358, No. 1777, 2000, pp. 3229–3246.

[50] Jones, L. E., Sandberg, R. D., and Sandham, N. D., "Direct numerical simulations of forced and unforced separation bubbles on an airfoil at incidence," *Journal of Fluid Mechanics*, Vol. 602, 2008, pp. 175–207.

[51] Dovgal, A. V., Kozlov, V. V., and Michalke, A., "Laminar boundary layer separation: instability and associated phenomena," *Progress in Aerospace Sciences*, Vol. 30, No. 1, 1994, pp. 61–94.

[52] Drazin, P. G. and Reid, W. H., *Hydrodynamic stability*, Cambridge University Press, 2004.

[53] Drazin, P. G., *Introduction to hydrodynamic stability*, Cambridge University Press, 2002.

[54] Dini, P., Selig, M. S., and Maughmer, M. D., "Simplified linear stability transition prediction method for separated boundary layers," *AIAA Journal*, Vol. 30, No. 8, 1992, pp. 1953–1961.

[55] Orszag, S. A., "Accurate solution of the Orr-Sommerfeld stability equation," *Journal of Fluid Mechanics*, Vol. 50, No. 4, 1971, pp. 689–703.

[56] Bridges, T. J. and Morris, P. J., "Differential eigenvalue problems in which the parameter appears nonlinearly," *Journal of Computational Physics*, Vol. 55, No. 3, 1984, pp. 437–460.

[57] Danabasoglu, G. and Biringen, S., "A Chebyshev matrix method for spatial modes of the Orr-Sommerfeld equation," Tech. Rep. NASA-CR-4247, 1989.

[58] Liou, W. W. W. and Morris, P. J., "The eigenvalue spectrum of the Rayleigh equation for a plane shear layer," *International Journal for Numerical Methods in Fluids*, Vol. 15, No. 12, 1992, pp. 1407–1415.

[59] Dongarra, J. J., Straughan, B., and Walker, D. W., "Chebyshev tau-QZ algorithm methods for calculating spectra of hydrodynamic stability problems," *Applied Numerical Mathematics*, Vol. 22, No. 4, 1996, pp. 399–434.

[60] McFadden, G. B., Murray, B. T., and Boisvert, R., "Elimination of spurious eigenvalues in the Chebyshev tau spectral method," *Journal of Computational Physics*, Vol. 91, 1990, pp. 228–239.

[61] Dawkins, P. T., Dunbar, S. R., and Douglass, R. W., "The origin and nature of spurious eigenvalues in the spectral tau method," *Journal of Computational Physics*, Vol. 147, No. 2, 1998, pp. 441–462.

[62] Bourne, D., "Hydrodynamic stability, the Chebyshev tau method and spurious eigenvalues," *Continuum Mechanics and Thermodynamics*, Vol. 15, No. 6, 2003, pp. 571–579.

[63] Zwillinger, D., *CRC standard mathematical tables and formulae*, Chapman and Hall/CRC, 2002.

[64] Wieneke, B., "PIV uncertainty quantification from correlation statistics," *Measurement Science and Technology*, Vol. 26, No. 7, 2015, pp. 074002.

[65] O'Meara, M. M. and Mueller, T. J., "Laminar separation bubble characteristics on an airfoil at low Reynolds numbers," *AIAA Journal*, Vol. 25, No. 8, 1987, pp. 1033–1041.

[66] Michalke, A., "On the inviscid instability of the hyperbolictangent velocity profile," *Journal of Fluid Mechanics*, Vol. 19, No. 4, 1964, pp. 543–556.

[67] Morris, P. J., "The spatial viscous instability of axisymmetric jets," *Journal of Fluid Mechanics*, Vol. 77, No. 3, 1976, pp. 511–529.

[68] Tam, C. K. W. and Morris, P. J., "The radiation of sound by the instability waves of a compressible plane turbulent shear layer," *Journal of Fluid Mechanics*, Vol. 98, No. 2, 1980, pp. 349–381.